Norwegian University of Science and Technology (NTNU)

Kavli Institute for Systems Neuroscience

Master's Thesis

Immunohistochemical and electrophysiological characterization of principal cells in layer II of the lateral entorhinal cortex

Author:

Gunhild Fjeld

Supervisor:

Eirik Stamland Nilssen

Faculty of Medicine, Department of Neuroscience

Trondheim, June 2015

NTNU – Trondheim
Norwegian University of
Science and Technology

Acknowledgements

The work presented in this thesis was performed at the Kavli Institute for Systems Neuroscience and Centre for Neuronal Computation (CNC) at the Norwegian University of Science and Technology (NTNU), under the supervision of Eirik Stamland Nilssen.

I would especially like to thank Eirik for his helpfulness, expertise, and patience. He has helped me throughout the practical work, and given me thoughtful constructive feedback on my written work as well. Also, thank you to Pål Kvello and Menno Witter for guidance along the way.

Another special thanks goes out to my family and friends, for always supporting me, and showing me a good time. Thank you to Anne for all the laughs in the office, and also for useful feedback on all matters.

Finally, I would like to thank Håkon and our dog Loke for all of their love and support. Coming home to the two of you is the best, and I am one lucky girl for having you both in my life.

Abstract

The entorhinal cortex (EC) is a part of the medial temporal lobe of the brain, and is considered to be important for learning and memory. The EC can be divided into two subdivisions; the lateral EC (LEC) and the medial EC (MEC). LEC and MEC have shown to be similar in many aspects, with the exception of properties of layer (L)II cells. These cells differ between the two subregions in terms of morphology and electrophysiology. Some ambiguity still exists whether the cells of LEC LII and MEC LII show similarities to the expression of the immunomarkers Reelin and Calbindin (CB). It has also been suggested that the reactivity to these immunomarkers in MEC LII might separate the cells into two populations with differences in projection patterns, cellular morphology and electrophysiology. The aim of this study is to investigate whether LEC LII cells can be separated by these two immunomarkers, and whether this coincides with differences in morphology and electrophysiology.

In this study, electrophysiological responses of principal cells of LEC LII were recorded in rat brain slice preparations with the use of whole-cell multipatch recordings together with intracellular filling with Biocytin. Subsequent immunohistochemistry staining against CB and Reelin was performed, followed by post-hoc morphological analyses.

A total of 102 out of the 104 morphologically identified cells, were found to be immunoreactive for Reelin but not for CB. The neuronal population included fan cells, multiform cells, oblique pyramidal cells and pyramidal cells. No correlation between morphologically identified cell type, and electrophysiological parameters was detected.

The main findings of this study suggest that LEC LII cells can only be subdivided based on their morphology, and not by their immunoreactivity to Reelin and CB, nor can they be separated based on their electrophysiological responses. This implies that the cells of LEC LII are more homogenous than the cells of MEC LII. It remains to be seen whether the LEC LII cells differ in terms of connectivity and projection patterns.

Abbreviations

General

AP thresh	Action Potential threshold
CA	Cornu Ammonis
CB	Calbindin
CR	Calretinin
DG	Dentate Gyrus
EC	Entorhinal Cortex
EPSP	Excitatory Postsynaptic Potential
GABA	Gamma-Aminobutyric Acid
HCN	Hyperpolarized-Activated Cation (channel)
HF	Hippocampal Formation
I_h	Cation Current
IR	Immunoreactive
ISI	Interspike Interval
IV	Current (I), Voltage (V)
LEC	Lateral Entorhinal Cortex
LPP	Lateral Perforant Path
MEC	Medial Entorhinal Cortex
NMDA	N-methyl-D-Aspartate
P	Postnatal
PaS	Parasubiculum
PER	Perirhinal Cortex
PHR	Parahippocampal Region
POR	Postrhinal Cortex
PrS	Presubiculum
R_I	Input Resistance
RMP	Resting Membrane Potential
SFA	Spike Frequency Adaptation
Sub	Subiculum
T (tau)	Time Constant

Chemicals, Solutions, Tools

ACSF	Artificial Cerebrospinal Fluid
ANOVA	Analysis of Variance
DMSO	Dimethyl Sulfoxide
MANOVA	Multivariate Analysis of Variance
NA	Numerical Aperture
PB	Phosphate Buffer
PFA	Paraformalaldehyde
TBS-Tx	Tris-buffered Saline-Triton X

Contents

1. Introduction

1.1. The hippocampal formation and parahippocampal region – an overview

The hippocampal formation (HF) and parahippocampal region (PHR) are structures belonging to the medial temporal lobe of the brain. The medial temporal lobe is involved in memory functions, a role that has been accepted for more than a century, since the description of von Bechterew in 1900 (Squire et al., 2004). Since the start of the past century, these regions have remained popular in studying episodic and episodic-like memory, and it has become clear that the structures involved are essential for both nonspatial and spatial memory (Scoville and Milner, 1957, O'Keefe and Dostrovsky, 1971, Eichenbaum and Fortin, 2005, Hafting et al., 2005, Solstad et al., 2008). The medial temporal lobe is also a region that exhibits the earliest changes in neurodegenerative diseases (Spargo et al., 1993, Shelbourne et al., 2007, Didic et al., 2011).

The HF comprises the dentate gyrus (DG), the subfields of Cornu Ammonis (CA1, CA2, CA3), and the subiculum (Sub). These structures are classified as allocortex, based on having only three layers. The PHR comprises the presubiculum (PrS), the parasubiculum (PaS), the entorhinal cortex (EC), and the perirhinal (PER) and postrhinal (POR) cortices (Insausti et al., 1997). Unlike the HF, the PHR consists of structures that are 3-6 layered, and referred to as periallocortex, often taken as a transition between the allocortex and the isocortex (Cappaert et al., 2014). Generally, layering is based on having a distinctive population of cells that vary in connectivity, morphology and cellular density (Purves et al., 2001).

1.2. Connectivity and anatomy (axes) of the HF and PHR

The HF and PHR are highly interconnected, and process information both serially and in parallel (Cappaert et al., 2014). The HF is said to be on top of the cortical hierarchy, where projections from unimodal and polymodal sensory areas converge, first onto the perirhinal and postrhinal cortices, before getting processed in the entorhinal cortices, and finally reaching the hippocampus itself. A feature of this processing system is the fact that all projections (with the exception of the local network within the HF) are heavily reciprocal (Suzuki and Eichenbaum, 2000).

The HF and PHR make up a complex three-dimensional unit, which requires several axes to explain more exact locations in all three dimensions. Figure 1.2.1 depicts this, and also shows how the different structures appear after coronal and horizontal sections through the area have been made. For the HF, three axes are used: the septotemporal axis (also called the long axis or the dorsoventral axis), the proximodistal axis (also referred to as the transverse axis), and the superficial-to-deep axis (or radial axis). For the PHR, a similar radial axis is used, as well as septotemporal and proximodistal axes for the pre- and parasubiculum. For the EC, a dorsolateral-to-ventromedial gradient is used, as well as the rostrocaudal (anterior-posterior) axis.

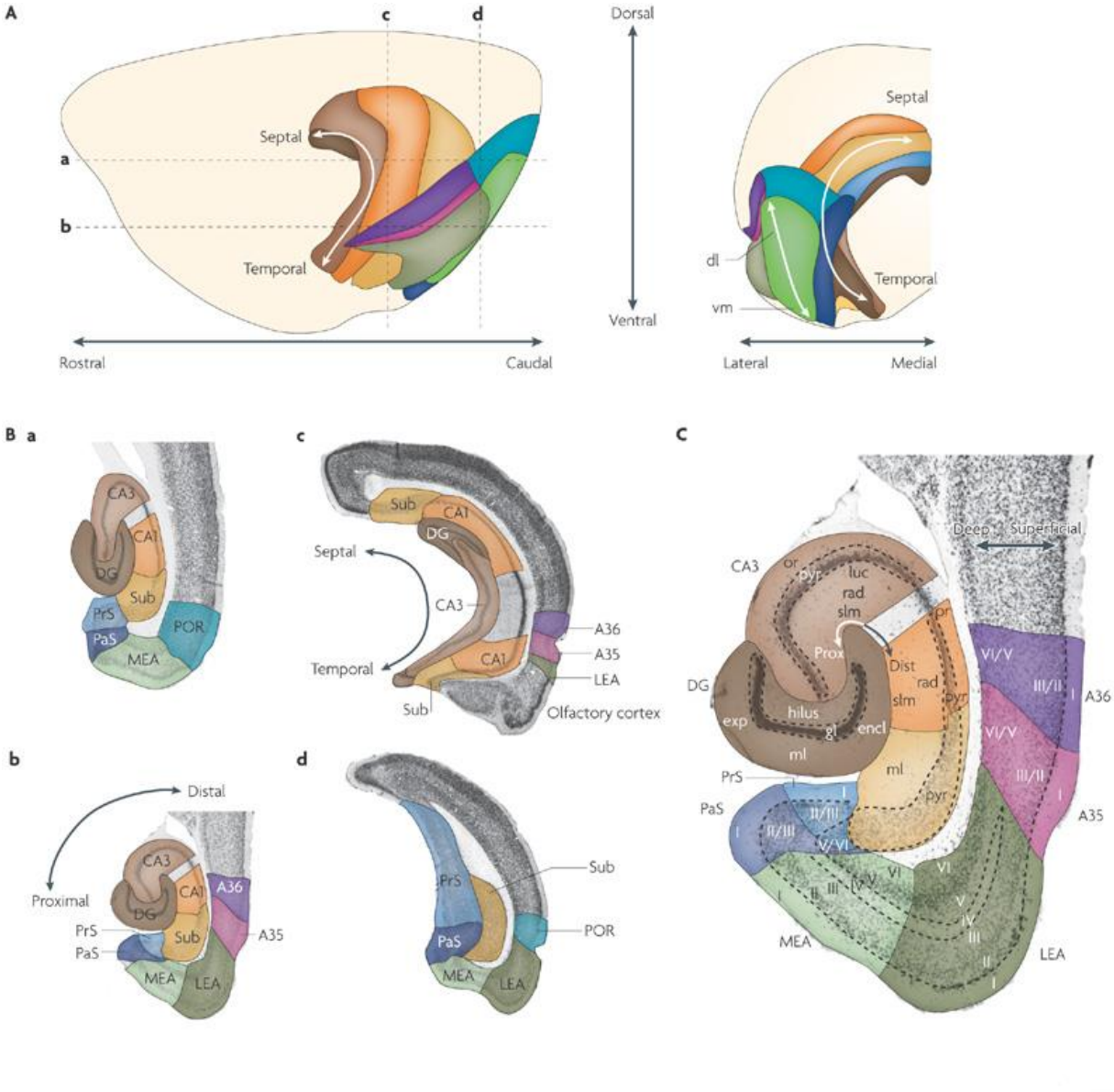

Figure 1.2.1. The relative position of the different structures that make up the hippocampal formation and the parahippocampal region. The axes include the (**A**) rostrocaudal, septotemporal, dorsoventral, lateral-medial, (**B**) distal-proximal and (**C**) deep-superficial. The hippocampal formation structures are given in brown and orange tones, and includes the dentate gyrus (DG), subfields of Cornu Ammonis (CA1 and CA3), and the subiculum (Sub). The parahippocampal region is given in blue, green and purple tones and includes the Postrhinal cortex (POR), Perirhinal cortex (PER), Lateral Entorhinal Cortex/Area (LEC/LEA), Medial Entorhinal Cortex/Area (MEC/MEA), Parasubiculum (PaS) and Presubiculum (PrS). Figure adapted from (van Strien et al., 2009).

1.3. The entorhinal cortex

1.3.1. The divisions of the entorhinal cortex

The EC makes up the hub for which the majority of information entering and leaving the HF must pass through. The EC is typically subdivided into two cytoarchitectonically and functionally different areas; a lateral part (lateral entorhinal cortex, LEC) and a medial part (medial entorhinal cortex, MEC) (Insausti et al., 1997, Cappaert et al., 2014). The border between LEC and MEC is not distinct, as cells situated at the border have shown to share compatible traits in terms of electrophysiology and morphology (Giocomo and Hasselmo, 2008, Canto and Witter, 2012b).

1.3.2. The perforant pathway and the functional differences between MEC and LEC

The HF receives its input via the perforant pathway arising from principal cells in LII and LIII of the EC, whereas the output of HF mainly goes through principal cells of LV of the EC (figure 1.3.1). The LII cells project to the DG and CA3 whereas the LIII cells project to the CA1 and subiculum(Witter, 2010). The perforant path(way) is divided into a medial perforant path originating from MEC LII/LIII and a lateral perforant path originating from LEC LII/LIII. It has been argued that these two parallel pathways process different information, based on differences in their input structures.

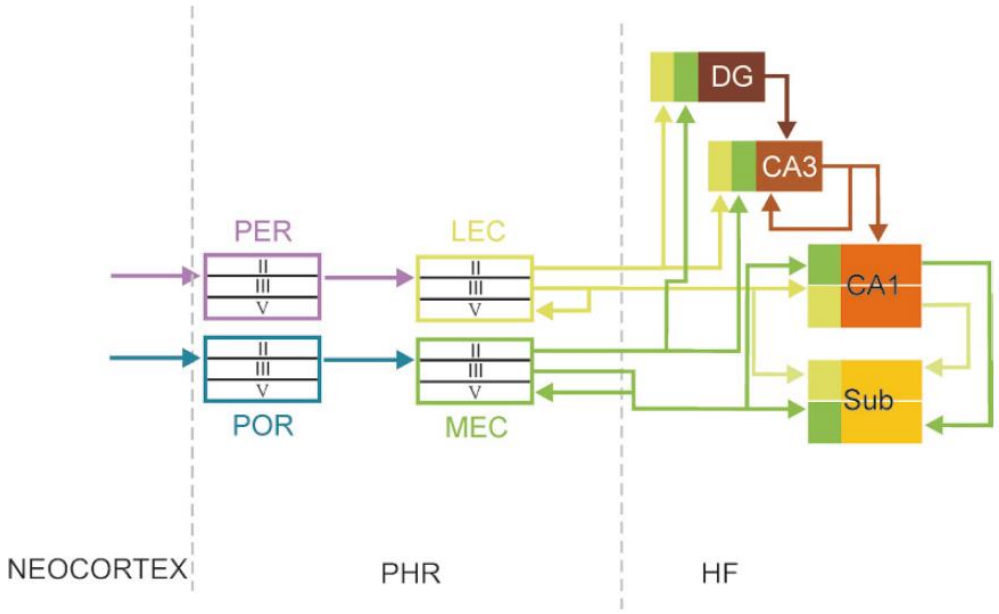

Figure 1.3.1. The connectivity of the neocortex – parahippocampal region – hippocampal formation. The perforant pathway arises from LII/LIII LEC and MEC, where it projects to DG, CA3, CA1 and Sub. The main neocortical input to LEC and MEC stems from the PER and POR respectively. Figure taken from (Witter, 2010).

MEC receives its main input from the postrhinal cortex (POR) (figure 1.3.1), and from the presubiculum, postsubiculum, and retrosplenial cortex (Burwell, 2000, Cappaert et al., 2014), Additionally, MEC receives a relatively stronger input from the visual association areas compared to LEC (Burwell and Amaral, 1998a). The POR is believed to be involved in context-related processing, and the presubiculum, postsubiculum and retrosplenial cortex are all shown to contain spatially tuned cells (Deshmukh, 2014). This spatial information that is fed into MEC could be important in the formation of grid cells, head-direction cells and border cells found there (Hafting et al., 2005, Hargreaves et al., 2005). MEC projects this spatial information via the perforant path to the hippocampus, and this input is involved in the formation of place cells located in the hippocampus (O'Keefe and Dostrovsky, 1971, Solstad et al., 2006, Zhang et al., 2013). The input to LEC, on the other hand, is not as spatially informative. LEC mainly receives its input from the perirhinal cortex (PER) (figure 1.3.1), in addition to a prominent input from the amygdala (Canto et al., 2008). The PER encodes nonspatial, object-related information. However, LEC has been shown to code spatial

information in the presence of objects, but not in an empty environment (Hargreaves et al., 2005, Deshmukh and Knierim, 2011). It has been noted that the way in which cells of MEC LII keeps track of their current location in space is bound to accumulate errors, and that a possible function of LEC is to correct and reset these errors by using landmarks in the environment as positional relativities. It is also possible that MEC yields useful distance estimations for LEC when determining the Euclidean distance between objects observed (Deshmukh, 2014). Either way, it is likely that MEC and LEC contribute to complementary inputs to the hippocampus.

1.3.3. The principal cells of the perforant path

Neurons can be either principal cells or non-principal cells. The principal cells make up the biggest group (around 90%), and are usually glutamatergic, excitatory neurons. They are also referred to as projection neurons, as they are responsible for projecting their axon collaterals across vast distances in the brain. The non-principal cells contribute more local functions, such as controlling and coordinating the activity of nearby cells, and are usually GABAergic, inhibitory neurons (Witter, 2010). Among the principal cells of the perforant path and in the EC as a whole, MEC and LEC LII cells have shown to be the most different in terms of morphology, electrophysiology and immunohistochemistry, whereas the pyramidal cells in EC LIII are more uniform (Varga et al., 2010, Canto and Witter, 2012b, a). While MEC LII mainly consists of stellate cells and pyramidal cells, cells of LEC LII are either fan cells, multiform cells, or pyramidal cells (Tahvildari and Alonso, 2005, Canto and Witter, 2012a, b). Generally, more is known about the MEC LII than LEC LII, and the following paragraphs will mainly deal with LEC LII principal cells.

1.4. Morphology

1.4.1. Morphological classes of LEC LII principal neurons

The LEC LII principal cells have not been extensively studied, and only recently a fourth morphological class was added (Tahvildari and Alonso, 2005, Cappaert et al., 2014). This new addition to the predescribed cell types was the oblique pyramidal cells (Canto and Witter, 2012a). The different morphological classes are shown in figure 1.4.1.

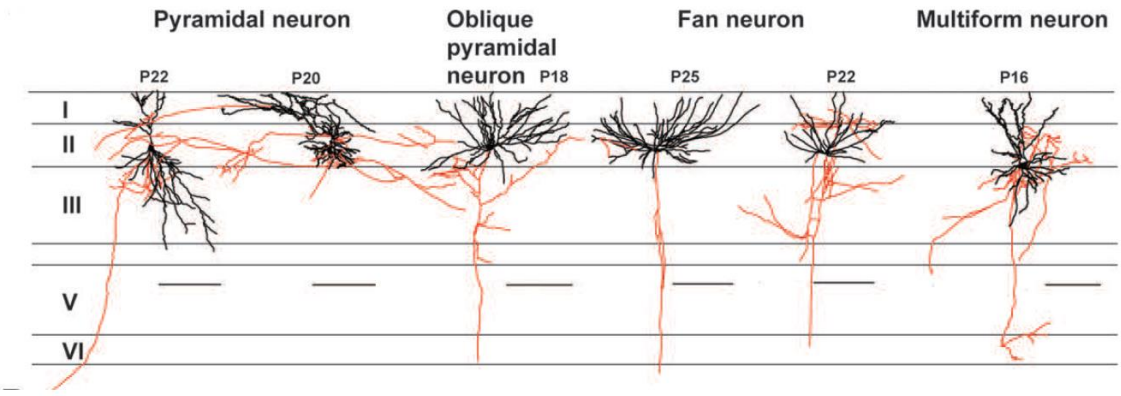

Figure 1.4.1. Morphology of the four different LEC LII principal cells, including the pyramidal neuron, oblique pyramidal neuron, fan neuron and multiform neuron. Adapted from (Canto and Witter, 2012a).

The pyramidal cells of LEC LII are similar to other pyramidal cells seen elsewhere in the brain. It is well characterized by its triangular shaped soma, and its large apical dendrite. In LEC LII the pyramidal neuron is vertically oriented with its apical dendrites reaching into LI, and basal dendrites spreading within LII and sometimes LIII. The pyramidal cells of LEC LII are for the most part situated deep within the layer (Tahvildari and Alonso, 2005, Canto and Witter, 2012a). The next cell type is the oblique pyramidal neuron which is a horizontally tilted (with respect to the pia) pyramidal cell, with more primary dendrites than the typical pyramidal cell. It is considered as a morphologically intermediate cell class between the pyramidal LEC LII cells and the multiform- and fan- cell of LEC LII (Canto and Witter, 2012b). The third cell type is the fan neuron, which is also the most abundant cell type of LEC LII (Canto and

Witter, 2012a). The fan neuron is named after its fanning appearance of apical dendrites reaching into LI and LII with hardly any reaching into LIII. Its basal dendritic tree is either missing, or rather underdeveloped (Tahvildari and Alonso, 2005, Canto and Witter, 2012a). The last cell type is the multiform neuron. This is the largest cell type of LEC LII. They are similar to the fan cells, but they have basal dendrites that reach into LIII as well. The multiform cell has a soma that can be either polygonal, fusiform or round. The fact that the primary dendrites are oriented in all directions make them resemble the stellate cell in MEC LII (Tahvildari and Alonso, 2005, Canto and Witter, 2012a). As of now, no other subclass of LEC LII principal cells have been described.

1.5. Electrophysiology

1.5.1. Background

To study a neuron's membrane properties, one assess the neuron's responses to either current or voltage responses. This procedure can yield several electrophysiological parameters of a cell, such as passive properties or spiking patterns. The different parameters can describe how the neuron at rest separates electrical charge, how this electrical charge separation changes when a current is applied, and how efficient the cell is to propagate this change. The most basic electrophysiological characteristic of a neuron is its resting membrane potential (RMP). Other properties like the neuron's time constant or input resistance, say something about how efficient the cell is to alter its output to alterations in its input. The time constant describes the temporal decay of the charge across the membrane, whereas the input resistance reflects the accumulated electrical resistance of the cell to current injected by the electrode (Ascoli et al., 2008). Lastly, the channel-composition of the cell gives it additional complex non-linear responses for the input/output relations. One type of channels is the hyperpolarized-activated cation (HCN) channels, which carry a current abbreviated I_h. These channels are activated upon hyperpolarization, and resist the voltage change in the cell with a contra-acting depolarization. This causes a sag, whereby the onset of the channel's function is slightly delayed. This same delay also causes a

rebound once the hyperpolarizing input to the cell has stopped, which is an overshoot due to the sudden stop of HCN channels holding the voltage change back (Pape, 1996).

1.5.2. Cell type classification based on electrophysiology

There has been some ambiguity as to whether LEC LII principal cells can be separated into different classes based on their electrophysiology. In a study done by Tahvildari and Alonso (2005) it was reported that it was possible to distinguish three classes of principal cells based on their electrophysiology, which corresponded to the morphologically identified pyramidal cells, multiform cells and fan cells. These authors showed that the pyramidal cells showed regular firing, a more negative resting membrane potential and a longer spike duration than fan cells, whereas multipolar cells represented a class that was electrophysiologically in between the pyramidal cells and the fan cells (Tahvildari and Alonso, 2005). However, this is in contrast with recent findings showing that "no clear correlation between the morphology of LII principal neurons and their electrophysiological properties could be established" (Canto and Witter, 2012a). In another study, Wang and Lambert studied the electrophysiological parameters of lateral perforant path (LPP) neurons, without separating them based on morphological cell type, representing the LPP neurons as a homogenous group (Wang and Lambert, 2003).

Some of the previously found electrophysiological parameters of LEC LII principal cells are listed in table 1.5.1. It should be noted that the Canto & Witter 2012a study included 31 LEC LII principal neurons, Talhvildari & Alonso 2005 included 31 LEC LII principal neurons and Wang & Lambert 2003 included 42 LPP projection neurons.

Table 1.5.1. Selected electrophysiological parameters of LEC LII principal neurons, from Canto & Witter 2012, Tahvildari & Alonso 2005, Wang & Lambert 2003. Canto & WItter did not subdivide the LEC LII principal cells, and their values were given in figures, not tables. Wang & Lambert recorded from lateral perforant path (LPP) projection neurons.

Parameters/ Study	Canto & Witter 2012	Tahvildari & Alonso 2005			Wang & Lambert 2003
	LEC II principal cells	Fan	Pyramidal	Multiform	LPP projection neurons
RMP (mV)		-65.9 ± 1.30	-75.1 ± 1.26	-70.0 ± 6.36	-66.6 ± 2.59
R_i (MΩ)	410	57.3 ± 18.98	41.6 ± 4.8	55.7 ± 18.12	204 ± 142.6
τ (ms)	25	23.2 ± 3.64	18.6 ± 2.61	20.7 ± 3.49	43.3 ± 32.4
Sag ratio	0.78	0.885 ± 0.07	0	0.75	0.95 ± 0.06
Rebound (mV)	3				
AP threshold (mV)		-45.4 ± 1.86	-44.6 ± 2.1	-45.8 ± 1.32	-51.7 ± 1.9

RMP: resting membrane potential; R_I: input resistance; τ: time constant; AP: action potential.

1.6. Immunohistochemistry of the entorhinal cortex

1.6.1. Background

Immunohistochemistry is a useful tool allowing the use of chromophore-labeled antibodies to stain for specific antigens in a tissue. The most prominent immunohistochemical markers for projection neurons in the entorhinal cortex include Calbindin[1] (CB) and Reelin. Both CB and Reelin show a strikingly clear laminar distribution in the superficial EC. CB-immunoreactivity (IR) can be seen in deep LII and superficial LIII, whereas the Reelin-IR remains mainly in superficial LII (Fujimaru and Kosaka, 1996, Ramos-Moreno et al., 2006, Berndtsson, 2013). Generally, the immunoreactivity for CB and Reelin has shown to be essentially non-overlapping in MEC (Varga et al., 2010, Berndtsson, 2013, Tang et al., 2014). This could potentially mean that the immunoreactivity of LEC LII cells to these markers could represent two separate cell groups, or populations of cells.

[1] Calbindin includes several calcium-binding proteins. The main form has a molecular weight of 28 kDa and is referred to as calbindin-D28k. The use of calbindin will hereafter refer to this isoform of the protein.

1.6.2. Calbindin

Calbindin is one of several calcium-binding proteins found in the central nervous system. CB-IR cells in MEC LII are believed to be pyramidal cells (Blair, 2014, Ray et al., 2014). However, species differences exist and it has been indicated that in the mouse stellate cells in MEC LII are CB-IR, whereas CB-IR cells of MEC LIII are pyramidal cells (Fujimaru and Kosaka, 1996). Also, the arrangement of the CB-IR and the negative CB-IR cells in LII differ within MEC between the mouse and the rat, whereas a more similar pattern is observed for LEC LII CB-IR cells in both species (Gianatti, 2015).

1.6.3. Reelin

Reelin is a large extracellular matrix protein that is especially prominent in EC LII neurons. It is involved in synaptic plasticity and it signals cell proliferation, migration or differentiation cues during brain development (Ramos-Moreno et al., 2006). Whereas CB-IR cells in MEC LII are believed to be pyramidal cells, Reelin-positive cells are believed to be stellate cells in MEC (Varga et al., 2010, Ray et al., 2014). A large population of LEC LII cells have been demonstrated to be Reelin-IR. These cells were pyramidal in shape, but also other labeled neurons that were fusiform or multipolar in shape were found, suggesting that several of the LEC LII cell types are indeed Reelin-IR (Ramos-Moreno et al., 2006).

1.6.4. Implications

Disease

The expression of both CB and Reelin are reduced in EC LII principal neurons in neurodegenerative diseases such as Alzheimer's, Parkinson's and Huntington's disease (Iacopino and Christakos, 1990, Iritani et al., 2001, Chin et al., 2007). Reelin expression is also reduced in normal aging, and linked to cognitive impairments (Stranahan et al., 2011a). CB and Reelin have been postulated to act as neuroprotectors, and therapeutic agents limiting the loss of CB and Reelin can potentially help reduce the effects of the degenerative disorders (Peterson et al., 1996, Thorns et al., 2001, Stranahan et al., 2011b).

Connectivity

A study done by Varga et al (2010) showed that the MEC LII neurons that were CB-IR did not project to the DG, whereas Reelin-IR cells did. This notion has recently received further support (Berndtsson, 2013, Kitamura et al., 2014). It has further been suggested that the CB-IR cells projected extra-hippocampally (Varga et al., 2010). What holds true for LEC in terms of connectivity remains to be seen.

Generalization

A hopeful view presented by studies done in MEC, is to be able to characterize a cell type by its immunoreactivity to either CB or Reelin. Obviously, with there being only two immunomarkers and four morphological cell types of LEC LII, dividing LEC LII into two cellular population is the upper most characterization ability of this method. However, this would enable a fast way of characterizing cells within one of the two populations.

1.7. Aim

A lot of focus has gone into studying MEC, and especially the cells in LII responsible for the generation of spatial input further fed into the hippocampal formation. Since the main studies previously done in LEC only concerned a limited number of cells, a further description of the principal cell types in LEC, and especially those confined to LII is of preference. Adding a high number of morphologically characterized LEC LII principal cells to the already existing database, is of interest, such that any subpopulations or trends can be identified and further described. Also, although it has been made clear that principal cells are distinguishable based on electrophysiology in MEC LII, it remains unclear if this is the case in LEC LII. Lastly, the concern of which cell types of LEC LII exhibits immunoreactivity to CB or Reelin is presently unclear.

Thus, the aim of this study is to investigate whether or not there are subpopulations of the predescribed principal cell types of LEC LII in terms of morphology, electrophysiology and immunohistochemistry. The following questions will be addressed:

- ***Are there any morphological subclasses of the predescribed principal cells of LEC LII?***

- ***Is it possible to separate the principal cell types of LEC LII into separate classes based on their electrophysiology?***

- ***Which principal cell types of LEC LII are immunoreactive for Calbindin or Reelin?***

2. Materials and methods

2.1. Whole-cell current clamp

2.1.1. Preparations

12 Long Evans rats between the postnatal ages 22-52 (P22-P52) were anesthetized with isoflurorane, and subsequently decapitated. The brain was then removed from the skull and immediately placed in ice-cold (4 C^o) artificial cerebrospinal fluid (ACSF) saturated with 95% O_2/5% CO_2. This choline chloride-based cutting ASCF (appendix 7.1) held an osmolality of about 400-430 mOsm. The cerebral hemispheres were separated, and the frontal parts and cerebellum were removed. One of the hemispheres was then preserved in the 95% O_2/5% CO_2 saturated ice-cold cutting ACSF, whereas the other hemisphere was selected for cutting.

The selected hemisphere was glued onto a holding plate, supported by a 2 % agar gel block. The hemisphere was then sectioned into 400 µm thick semicoronal slices in a bath of ice-cold (4 C^o) cutting ACSF using Leica VT 1000s vibratome. The semicoronal sections were at an approximate 20^o angle with respect to the coronal plane (see figure 2.1.1). This was the angle shown to give the most intact axons and dendrites after cutting through LEC (De Villers-Sidani et al., 2004). The slices were then left to incubate for approximately one hour in magnesium chloride-rich holding ASCF at 35 C^o to allow recovery from the intrusive slicing. All solutions are in the appendix section 7.1.

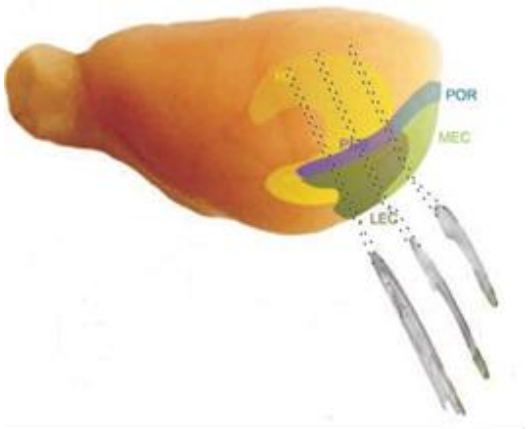

Figure 2.1.1. Illustration of the semicoronal sections of LEC taken at three different rostrocaudal levels. MEC depicted in light green, LEC in dark green, perirhinal cortex (PER) in light purple, postrhinal cortex (POR) in light blue and the hippocampal formation (HF) in yellow. Figure adapted from (Canto and Witter, 2012a)

2.1.2. Whole-cell current clamp

Patch micropipettes were pulled using a standard-walled borosilicate tubing (BS4 30-0057, Harvard Apparatus, MA, USA), with a flaming brown micropipette puller (P97, Sutter Instrument Co., CA, USA). The patch pipettes had a final measured resistance of 4-9 MΩ. The patch pipettes were filled with a K-gluconate-based intracellular solution (appendix 7.1). Biocytin (Sigma-Aldrich, MO, USA) (2-4 mg per ml) was added to the intracellular solution. The first semicoronal slice was taken from the holding chamber and put into the recording chamber of the rig, where a ACSF solution (see appendix 7.1) saturated with 95% O_2/5% CO_2 continuously perfused the tissue to preserve it best possible.

A camera connected to the infrared differential interference contrast (IR_DIC) microscope (Olympus BX51W1, Shinjuku, Tokyo) made it possible to visualize the cells in the slice. The rhinal fissure and dense patches of large cells found in LEC LII were used to ensure that it was indeed LEC LII cells that were being patched. The patch pipettes were made to come into focus, so that a clear interaction between the tip of the pipette and the cell of interest could be visualized. Before approaching the cell's membrane, positive pressure was applied. Upon contact with the cell membrane, the positive pressure was relieved forming a gigaohm

seal between the pipette tip and the cell membrane. Suction was subsequently applied to rupture the membrane and obtain the whole-cell configuration mode. Once membrane rupture occurred, the Biocytin filled the cells (Aston-Jones and Siggins, 2000). The recordings were made with a Multiclamp 700A and a Multiclamp 700B Amplifier (Axon Instruments, CA, USA). Data was collected with a sampling rate of 10 kHz with an Instrutech ITC-1600 board (Instrutech, NY, USA). Data acquisition and off-line analysis were done using a custom-made script in IGOR Pro (Wavemetrics, OR, USA). Each cell was recorded for more than 15 minutes. At the end of the recording day, the slices were put into 4% paraformalaldehyde (PFA, see appendix 7.2) overnight in 4^{o}C.

The numbering of the slices that were patched is that of (yymmdd_# of slice) where the "# of slice" ranges from 1-4, where 1 is the first patched slice, and 4 the last patched slice. I patched slices 150211_1, 150212_1, 150212_2 and 150212_3, which amounted to five cells, and my supervisor patched the rest of the slices.

2.1.3. Recording protocol

Recordings were carried out in current clamp mode, where voltage responses to the current injections were measured. Up to four cells were patched at the same time, and checked for connections as part of a separate project. For investigating membrane properties of the cells, a current-step protocol was used. In this protocol, current injections lasted for 500 ms per sweep, with an increment of 100 pA ranging from -400 pA to +500 pA. This resulted in a run consisting of 9 sweeps. Figure 2.1.2 shows the injection protocol.

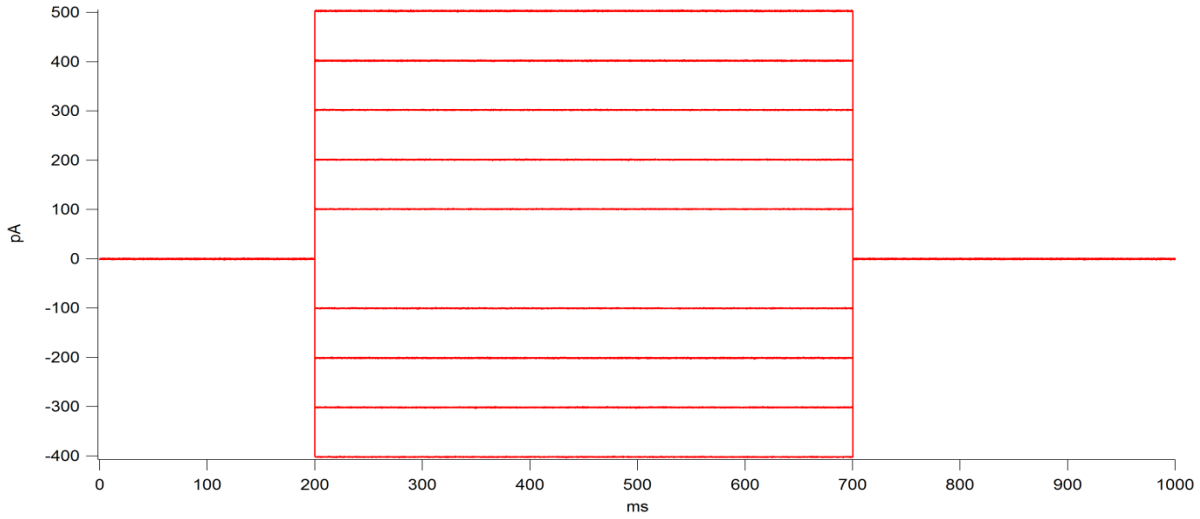

Figure 2.1.2. Current injection protocol, showing the arrangement of the 9 current injections (in pA) with time (in ms).

2.2. Electrophysiological analysis

Electrophysiological recordings with an action potential height of more than 70 mV from threshold to peak were kept. Other criterias include an input resistance of more than 40 MΩ, a resting membrane potential more negative than -50 mV and an action potential overshoot of more than 20 mV (Giocomo and Hasselmo, 2008). No electrophysiological recordings with holding currents were included. Electrophysiological analysis was performed using the recorded data in IGOR pro and Microsoft Excel. The parameters were calculated by averaging over the first four sweeps of the same current injection wherever possible. Illustrations of the calculations made are shown in figure 2.2.1.

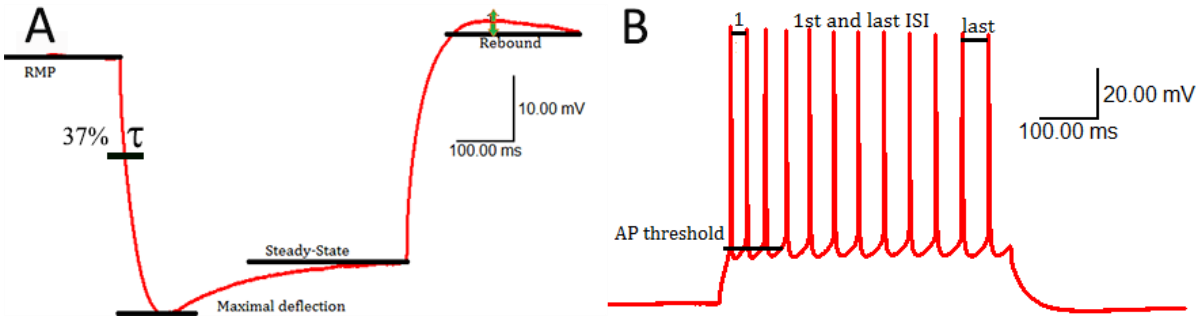

Figure 2.2.1. Illustrations of the different areas of interest for electrophysiological parameters calculations. **A**: Depicts the measure for the resting membrane potential (RMP), rebound and the maximal deflection and steady-state used for calculating the sag ratio and the time constant. Time constant (τ) is also shown at its approximate temporal position. **B**: Depicts the measure of the AP threshold, as well as the first interspike-interval (ISI) and last ISI used to calculate the ISI ratio.

2.2.1. Resting membrane potential

The resting membrane potential was calculated using the first current injection step, at the time period 0-200 ms when no current was injected, depicted in figure 2.2.1.A.

2.2.2. Action potential threshold

The action potential threshold was determined by using IGOR's action potential table, using the first derivative coupled with a threshold function in IGOR, of the first action potential seen (usually at the +100 pA current injection). The approximate position of the threshold is illustrated in figure 2.2.1.B.

2.2.3. Input resistance

Input resistance was calculated by averaging the steady-state voltage response and subtracting the resting membrane potential from this value. It was calculated at the -100 pA current step. By applying Ohm's law, the calculation was $R_{input} = \Delta V/I$, resulting in values in the MΩ scale. Steady-state voltage and RMP depicted in figure 2.2.1.A.

2.2.4. Sag ratio

For calculating the sag ratio, the most negative voltage value within the range of 240 ms to 400 ms of the recording was used, and the ratio was that of this maximum deflection divided by the steady state value. The sag ratio was calculated at the -300 pA current step injection. Maximum deflection and steady-state voltage given in figure 2.2.1.A.

2.2.5. Rebound

Rebound measures were made using the voltage values within the range of 780-1000 ms, where the difference between the maximum value and minimum value in this range yielded the rebound (figure 2.2.1.B). This was done using the -300 pA current step injection. For sweeps with an action potential firing because of the rebound, the rebound was not calculated.

2.2.6. Time constant

Manual calculations were performed, exploiting how RC-circuits work during the discharge of a capacitor on the -100 pA current injection step. By modeling the cell as a capacitor, the following calculation was applied:

$V(t) = V_{max}(e^{-t/\tau})$, where V_{max} is the steady-state. At $t=\tau$, $V(t) = V_{max}(e^{-1}) \approx 0.37\ V_{max}$, meaning that the time constant corresponds to the time taken to reach 37% of the maximum voltage low (depicted in figure 2.2.1.A) (Molleman, 2003).

2.2.7. Interspike-interval ratio

The interspike-interval ratio, also called adaptation ratio, is the ratio of the first interspike-interval divided by the last interspike-interval. These calculations were performed on the +300 pA current injections. First and last interspike-intervals are displayed on the graph in figure 2.2.1.B.

2.2.8. Statistical analysis

In order to establish whether the electrophysiological parameters were significantly different between the four different cell types, a statistical analysis was performed. The electrophysiological parameters were first tested to see whether they were normally distributed, using each cell type's mean values for each electrophysiological parameter. This was done employing a Shapiro-Wilk test for normality. Normally distributed parameters were analyzed using a multivariate analysis of variance (MANOVA) test. For the parameters that were not normally distributed a Kruskal-Wallis nonparametric test was performed, which is also an analysis of variance that uses ranks to decide whether samples originate from the same distribution, and is the non-parametric equivalent to ANOVA/MANOVA (Kruskal and Wallis, 1952). P-values < 0.05 were considered significant for all tests. Data was analyzed with the statistical software package SPSS statistics version 21.0 (IBM, NY, USA).

2.3. Morphological reconstructions and characterizations

2.3.1. Secondary antibody staining of the Bicotyin-filled cells

The tissue was first rinsed 5x15 min in Tris-buffered saline Triton-x (TBS-tx), before being incubated overnight in room temperature with the secondary antibody Streptavidin Alexa 488 (Invitrogen, Oslo, Norway) in a concentration of 1:600 (in TBS-Tx). The following day the sections were rinsed 3x15 minutes in TBS-Tx. The sections were subsequently dehydrated in 30%, 50%, 70%, 90%, 2x100% ethanol, sequentially, each step lasting for 10 minutes. Then a 1:1 mixture of ethanol and methyl salicylate for 10 minutes. Finally, the sections were stored in methyl salicylate in 4^{o}C.

2.3.2. Confocal microscopy

The methyl salicylate immersed slices were put on a metal slide for scanning using a confocal microscope (Zeiss LSM 510 meta) where they were scanned using the 10x air objective (0.45 NA) and the 40x oil objective (1.3 NA). For the immunohistochemical co-localization scans, the 63x oil objective (1.4 NA) was used. The confocal microscope allows to optically section the slice in the z-direction, and integrating this axis over the x,y-plane (specimen plane), thus

obtaining a high resolution 3D-image (Inoue, 2006). A selection of slices were elected for high-resolution scanning using a 0.6µm interval for the z-direction image-stacking using the 40x oil objective, in order for them to be sufficiently detailed for 3D reconstructions. The remaining slices were scanned using a 2µm interval z-stack with the 40x oil objective. All sections were scanned using a 1024x1024 resolution. The lasers that were used were the Argon laser (458, 477, 488, 514 nm – 30 mW), DPSS laser (561nm – 10 mW) and the HeNe (633nm – 5 mW). A 405nm diode (30 mW) was used for scanning a fluorescent Nissl section (fluorescing at 455 nm). All filters and objectives were from Carl Zeiss (Zeiss, Oberkochen, DE).

2.3.3. Three-dimensional reconstruction of the stained neurons

The neurons in the high-resolution image-stacks were manually reconstructed in 3D using the AMIRA (FEI, Oregon, USA) software. AMIRA employs a skeleton tool (Schmitt et al., 2004, Evers et al., 2005) which traces the filled neuron slice by slice in the image stack. Once fully reconstructed, a surface file is made from the skeleton, which can then be treated separately from the original image-stacks and used in other applications (Halavi et al., 2012).

2.4. Immunohistochemistry

2.4.1. Finalizing the protocol

The testing was carried out after I had done the initial immunoprotocol on slice numbers 141001_2, 141001_3, 141002_1, 141002_2, 141002_3 and 141002_4. The Reelin labeling appeared to label the same cells as previously reported (Ramos-Moreno et al., 2006), whereas there was too little CB labeling. The other slices were scanned for morphology while the immunoprotocol was optimized. This means that the rest of the slices were stained using Streptavidin → dehydrated → scanned for morphology → rehydrated → stained for Reelin and CB → dehydrated → scanned for colocalization purposes. The initial protocol is in the appendix (7.1).

No finalized protocol for immunostaining against CB or Reelin in 400 µm slices was available. I performed a total of 9 immunohistochemistry tests, testing variables such as primary antibody concentration, primary antibody incubation period, and whether or not the immunoreactions needed to be heat induced. These variables were tested, in a variety of combinations. The finalized protocols are attached in the appendix (7.1). A control using just the secondary antibody for both CB and Reelin was also performed (figure 7.3), as well as a control to see whether there was a difference in staining using a mouse or a rabbit anti-CB primary antibody (figure 7.4).

2.4.2. Immunostaining for Calbindin and Reelin

The tissue was first rinsed 2x15 minutes in 0.125M phosphate buffer. Next, it was rinsed 5x15 min in Tris-buffered saline Triton-x (TBS-tx). Subsequently, the slices were incubated in a mixture consisting of 1:10 goat serum (Abcam, Cambridge, UK):TBS-tx for three hours for blocking. Then the primary antibodies were added using mouse anti-Reelin (1:1000) (Millipore, Merck Life Science AS, Oslo, Norway) and rabbit anti-Calbindin (1:3000) (SWANT, Inc, Marley, Switzerland). The slices were then left to incubate for three days on a shaker in 4^{o}C. These antibodies have both previously been extensively tested, and published elsewhere (de Rouvroit et al., 1999, SWANT, 2011). Next, the tissue was washed 5x15 min in TBS-tx followed by the incubation of the secondary antibodies, using goat anti-mouse Alexa 546 (1:400) (Thermo Fisher, MA, USA) and goat anti-rabbit Alexa 635 (1:400) (Thermo Fisher, MA, USA) overnight in room temperature. The following day, the tissue was rinsed 3x15 min in TBS-tx, then either stored in the cryoprotective dimethyl sulfoxide (DMSO), or dehydrated directly for scanning using the confocal microscope. The dehydration process and the full immunoprotocols are in the appendix (7.1).

2.4.3. Colocalization of immunomarkers

To assess the colocalization between Biocytin with either CB or Reelin, the confocal (Zeiss LSM 510 meta) microscope was utilized. A 63xoil immersion image yields a good close up of the cells of interest, and having scanned the same section in the same xy plane using all three channels, one is able to infer whether the Biocytin cell is indeed positive for Calbindin and/or Reelin. The Laser Scanning Microscopy (LSM) files from the confocal scans were

further processed using imageJ (Rasband W, National Institutes of Health, MD, USA), Adobe Photoshop (Adobe Systems Inc., CA, USA), Adobe Illustrator (Adobe Systems Inc., CA, USA) and AMIRA.

2.4.4. Fluorescing Nissl stain

A fluorescing Nissl stain was performed on some control slices, to check whether the immunoreactivity for CB and Reelin covered the whole cellular population of LEC LII or not. The fluorescing Nissl solution was added one day after the primary antibody for CB and Reelin, resulting in a total incubation period of two days. The Nissl-stain fluoresced at a wavelength of 640 nm.

2.5. Positioning the recorded cells

A Nissl-stained section was used to delineate LEC, and the slices were reconstructed using the AMIRA software. The recorded cells were then plotted using the distance from the rhinal fissure and the distance from the pial surface, showing the medial-lateral and deep-superficial distribution of the recorded cells.

A series of Nissl-stained semicoronal sections, with a thickness of 50µm and interval of 4 (resulting in images that were 200 µm apart) were used to best fit the slices in the anterior-posterior axis. The 20x images were obtained in a MIRAX Brightfield scanner equipped with a Merlin Camera F-146C IRF MEDICAL (ALLIED Vision Technologies Medical). The sections and images were obtained by my supervisor. The images were subsequently matched with the confocal microscope images of the recorded sections. Three bins à 800µm were used, each bin contained four images separated 200µm apart. This was to give the relative position of the recorded cells in the anterior-posterior axis.

3. Results

From the 12 rats used in this study, a total of 42 slices were recorded from. I analyzed data from 104 cells with a satisfactory Biocytin-filling for determining their cell type, 90 of which had a satisfactory electrophysiological recording, based on the criteria given in section 2.2. All 104 morphologically identified cells were checked for their immunoreactivity to CB and Reelin.

3.1 Principal cell type distribution in LEC LII

Out of the 104 morphologically identified neurons, 56 (54%) were classified as fan cells, 19 (18%) were classified as multiform cells, 18 (17%) were classified as oblique pyramidal cells, and 11 (11%) were classified as pyramidal cells (figure 3.1.1.A). 27 of these cells were reconstructed in 3D. Out of the 90 cells that were included based on the electrophysiological criteria, 48 (53%) were fan cells, 18 (20%) were multiform cells, 14 (16%) were oblique pyramidal cells and 10 (11%) were pyramidal cells (figure 3.1.1.B).

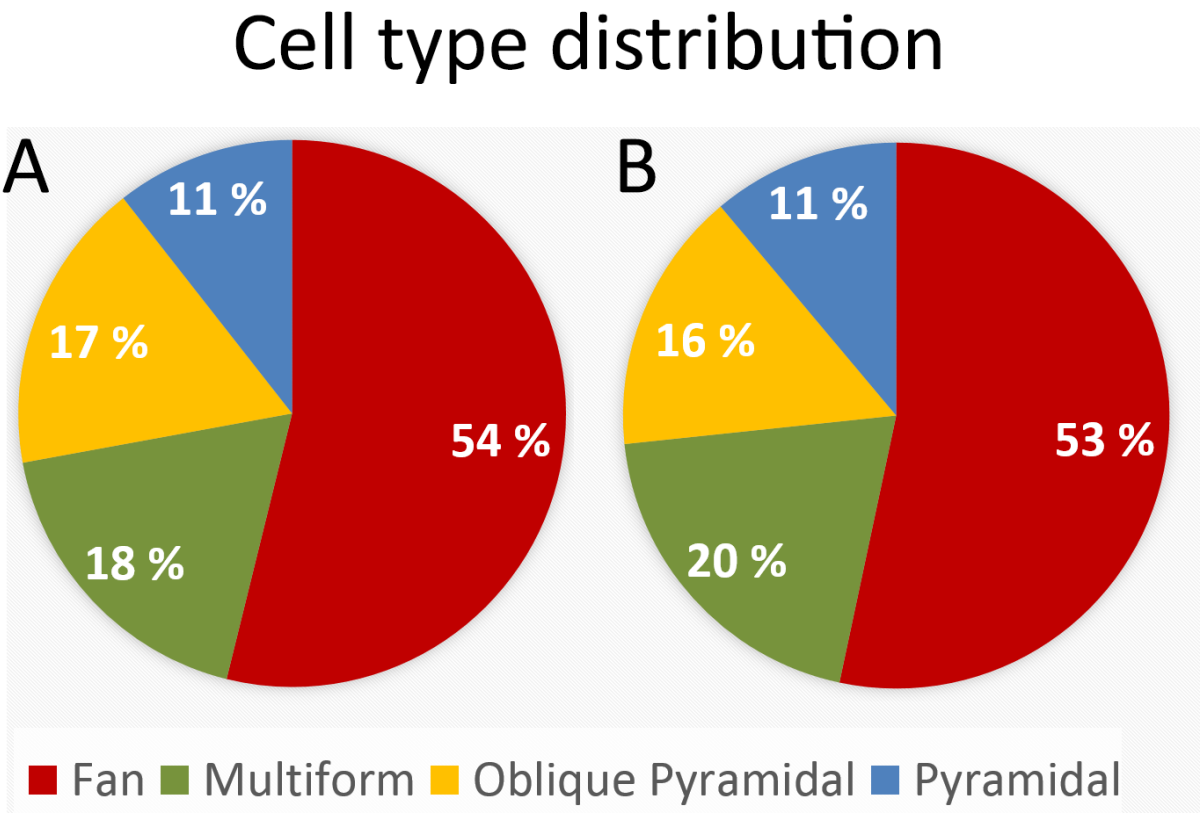

Figure 3.1.1. Pie charts showing the proportions of the different cell types in LEC LII. Fan cells in red, multiform cells in green, oblique pyramidal cells in yellow, pyramidal cells in blue. **A**: Proportions of the morphologically identified cell types, based on morphological identification alone (N = 104). **B**: Proportions of the morphologically identified cell types with a satisfactory electrophysiological recording (N=90).

All cells were distributed in the more superficial part of LII of LEC, and mainly situated close to the rhinal fissure. Figure 3.1.2 gives an overview of the recording site and the positions of the different cell types. The locations of the cells were frequently similar, and there is therefore an extensive overlap between cells in superficial LII in this figure. The indentation in the rhinal fissure depicts the measurement point used to make the figure (see section 2.5).

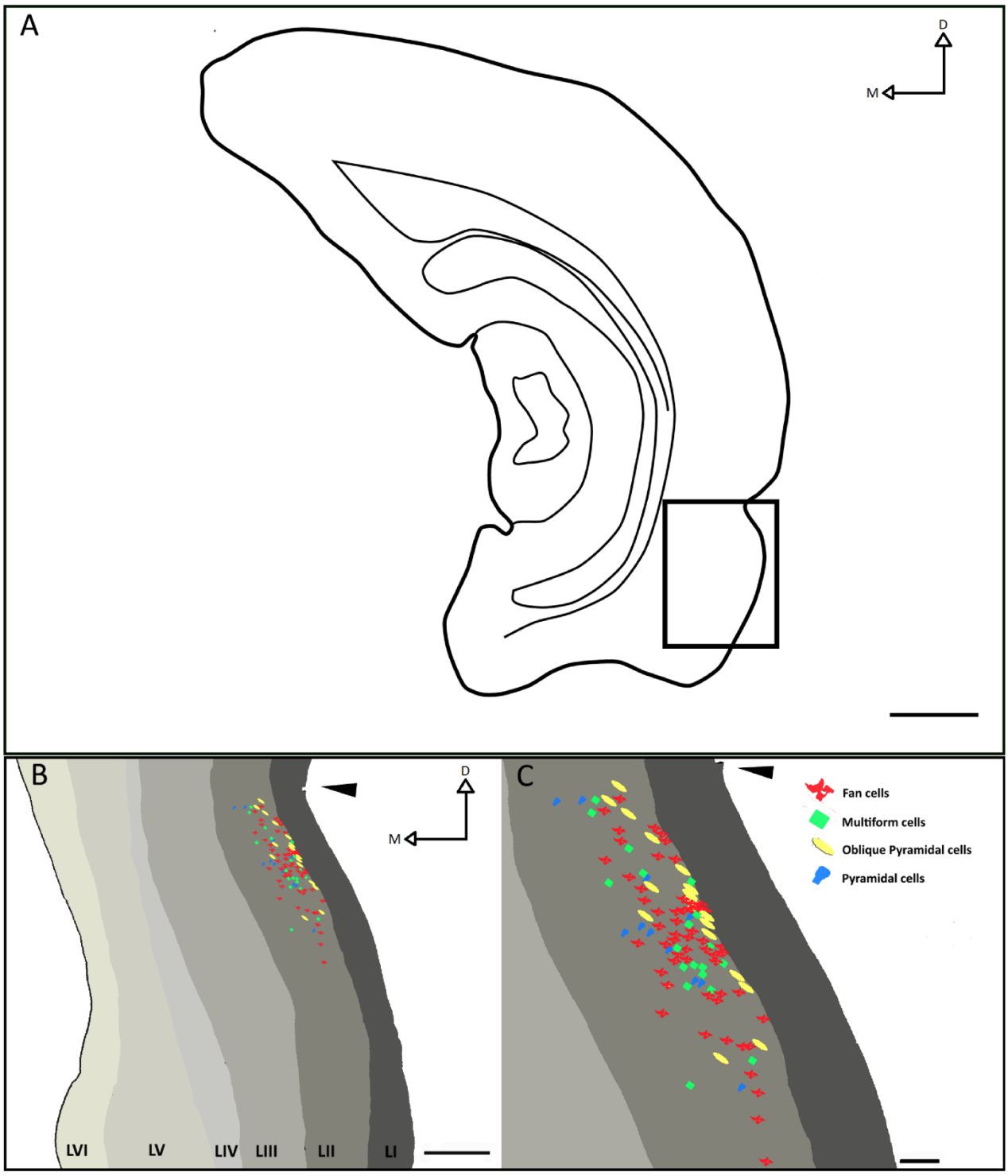

Figure 3.1.2. The morphologically identified cell types plotted and combined on their recordings sites in LEC LII. Arrowhead shows the position of the rhinal fissure in both B and C. **A**: Coronal cartoon section showing the approximate position of LEC in the cut out in B. D = dorsal, M = medial. Scale bar = 1000 µm. **B**: an overview of the medial-lateral and deep-superficial extent of the recorded cells. D = dorsal, M = medial. Scale bar = 200 µm. **C**: a close-up of the 104 recorded cells separated by their respected symbol and color. Scale bar = 50 µm.

3.2 Morphology

Fan cells

The fan cells made up the largest group (figure 3.1.1). The fan cells are so-called due to the orientation of their dendritic tree, fanning out towards the pial surface. The basal dendritic tree of the fan cell was rather rudimentary, and sometimes not present at all. This restriction made the dendritic domain of the fan cells isolated to layers I and II. The extensive branching of the dendrites towards the pial surface covered a half-disk with the lengths of the dendrites being approximately the same in all direction. They varied morphologically in terms of dendritic tilting, and somatic tilting and shape. The tilted fan cells (like the one in figure 3.2.1) had one side of dendrites pointing towards the pia and the other pointing towards LIII. The fan cells that were proximal to the rhinal fissure had their dendrites oriented away from the fissure, making them radially restricted (figure 3.2.2). All of the fan cells were spiny, and often the axons could be traced to the angular bundle (the axon was cut in roughly 50% of the cases as a result of brain sectioning), with axon-collaterals branching off mainly in LIII.

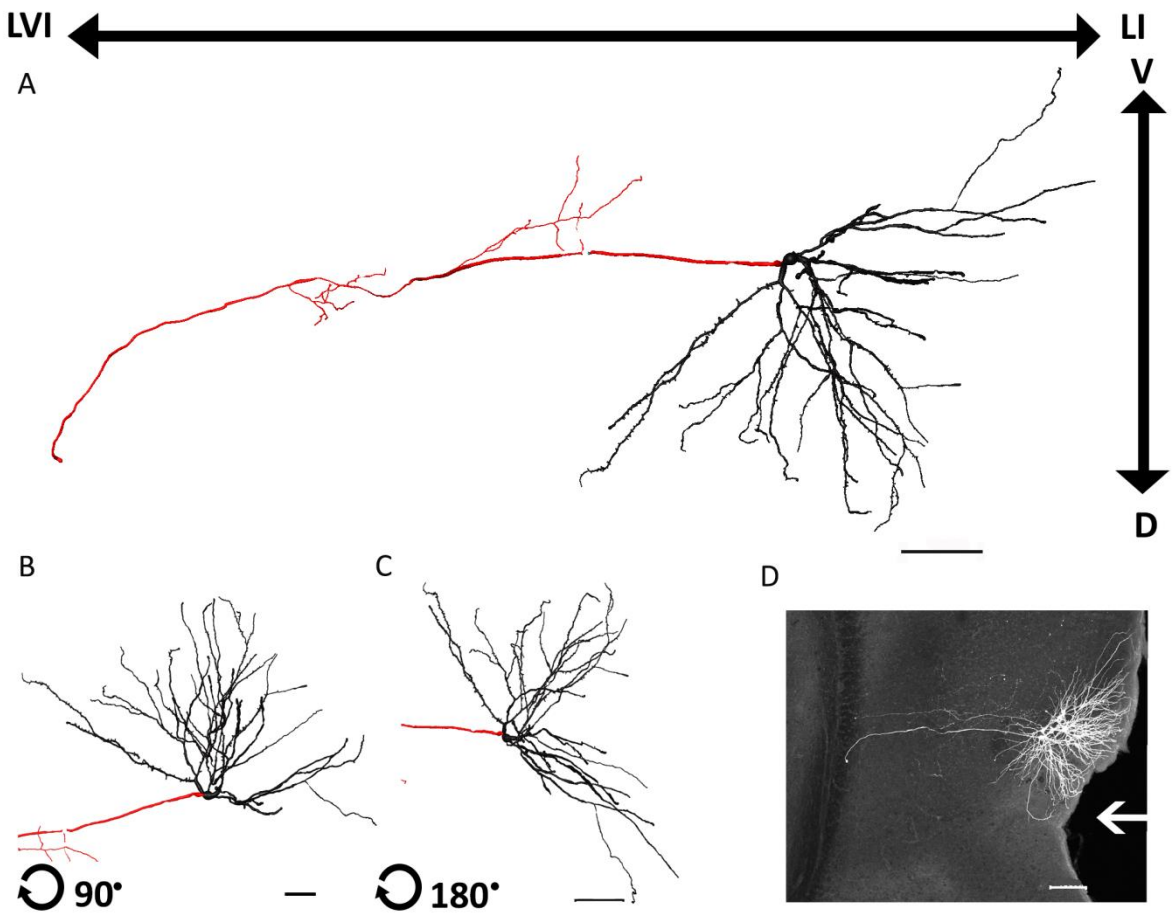

Figure 3.2.1. 3D reconstruction of a fan cell, axon depicted in red. **A**: the full extent of the cell, in the xy plane, **B**: the cell tilted approximately 90°, showing its dendrites deeper in the slice, **C**: the cell flipped horizontally (180°) from A, **D**: 10x maximum z-stack projection confocal image showing a four-cell cluster where the reconstructed fan cell is the cell on the lower left with the fully intact axon. Arrow indicates the position of the rhinal fissure. Scale bars: 50 µm for images A, B, C, 100 µm for image D.

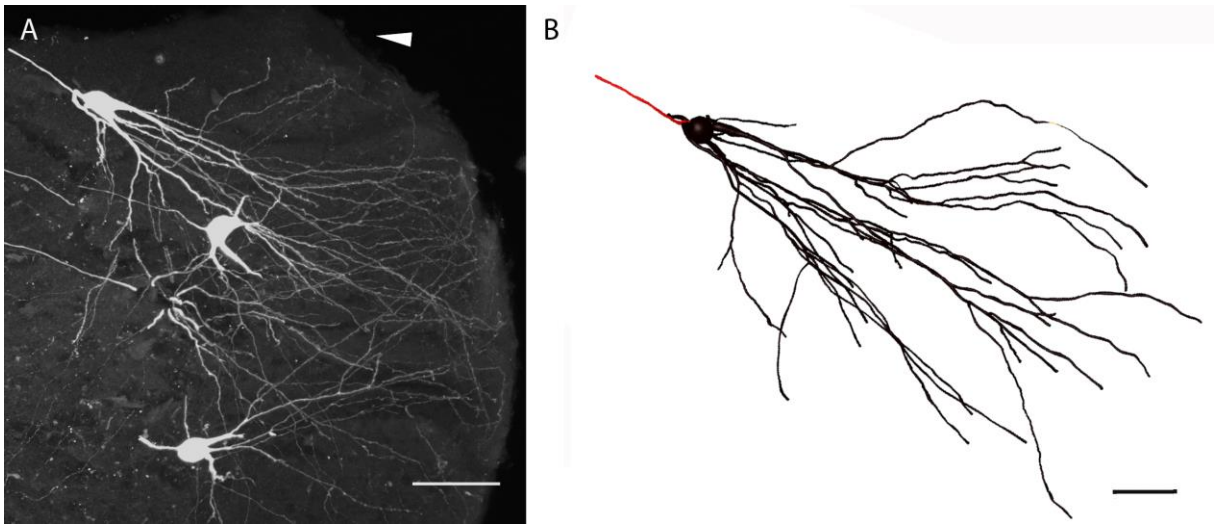

Figure 3.2.2. Fan cell proximal to the rhinal fissure. **A**: A 40xoil maximum z-stack projection confocal image of three fan cells that are proximal to the fissure, the upper fan cell is distorted by the proximity to the rhinal fissure position shown by the white arrow head. Scale bar = 50 µm. **B:** Showing the 3D-reconstruction of the fan cell in the upper left corner in the confocal image in A, with dendrites oriented away from the fissure. Cut axon depicted in red. Scale bar = 30 µm.

Two subclasses of the fan cells were observed, namely the parachute fan cells and the spherical fan cells. The soma of these two subclasses varied from a parachute-shaped soma bending towards LI, to a more spherical-looking shape (depicted in figure 3.2.3). These two different somatic shapes also usually meant a different spreading of the apical dendritic tree as well. For the parachute-shaped soma, the apical dendritic tree fanned out into an almost 180^{o} radial extent. For the spherical soma, however, the apical dendritic tree was sometimes restricted as much as 80^{o} into a barrel-like confinement, in the same direction of the axon (deep-superficial).

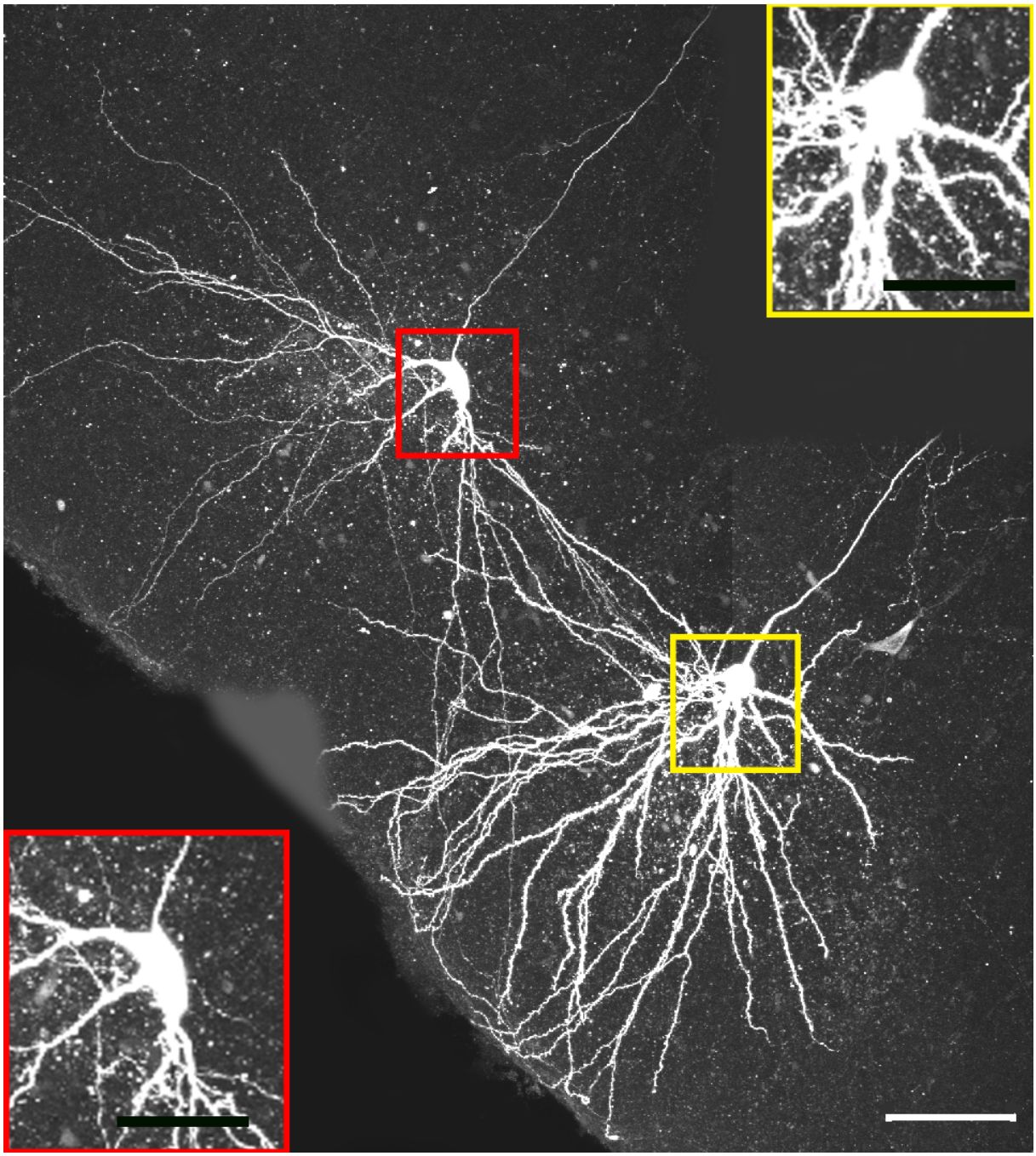

Figure 3.2.3. A 40xoil maximum z-stack projection confocal image, showing two fan cells of LEC LII. The fan cell in the upper left is a parachute fan cell, and the one in the lower right is a spherical fan cell. Image in the red box is a magnified (2x) image of the soma of the parachute fan cell, and image in the yellow box a magnified (2x) image of the soma of the spherical fan cell. Scale bar = 50 µm for the large image and 25 µm for the boxes.

Multiform cells

The multiform cell group comprised the second largest group of cells (figure 3.1.1). These cells generally appeared larger than the fan cells, both in radial distribution of dendrites and somatic size, and often displayed a fusiform-shaped somata (see figure 3.2.5). The dendritic domain of the multiform cell is fully distributed in all directions. The dendrites that reached the pial surface would curve accordingly, and follow the surface in parallel for up to tens of micrometers. This feature is both evident in figure 3.2.4 and in figure 3.2.5. The multiform cells generally had more primary dendrites than what was observed for the other cell types. The basal dendrites of the multiform cell remained mainly in LII but also reached into LIII, and sometimes quite deep into this layer. The dendrites of the multiform cell were also spiny. The axon could be followed to the angular bundle whenever it was not cut, and it gave off axon collaterals in LII and LIII. The multiform cells found near the rhinal fissure (like the one in figure 3.2.4) also had the dendrites pointing in the direction away from the fissure.

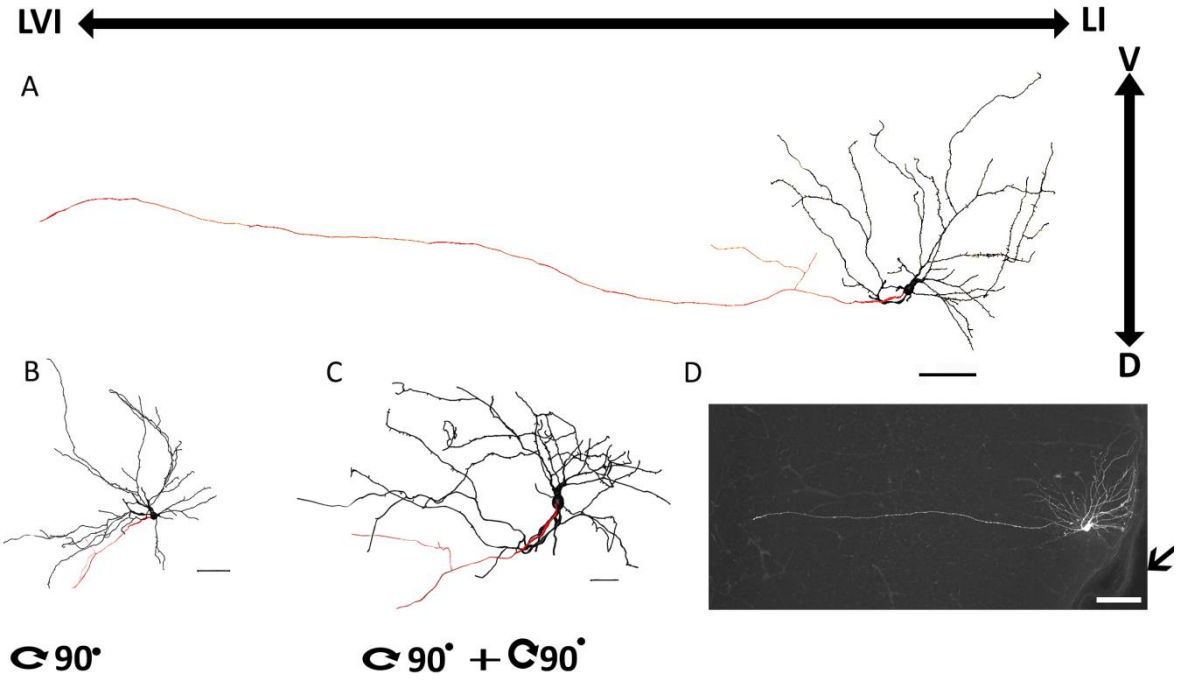

Figure 3.2.4. 3D reconstruction of a multiform cell, axon depicted in red. **A**: the full extent of the cell, in the xy plane. **B**: same cell rotated 90° outwards **C**: same cell from a more lateral view (90° tilted from B). **D**: The 10x maximum z-stack projection confocal image of the reconstructed cell. Arrow indicates the position of the rhinal fissure. Scale bars: A = 50 µm, B = 40 µm, C = 20 µm, D = 100 µm.

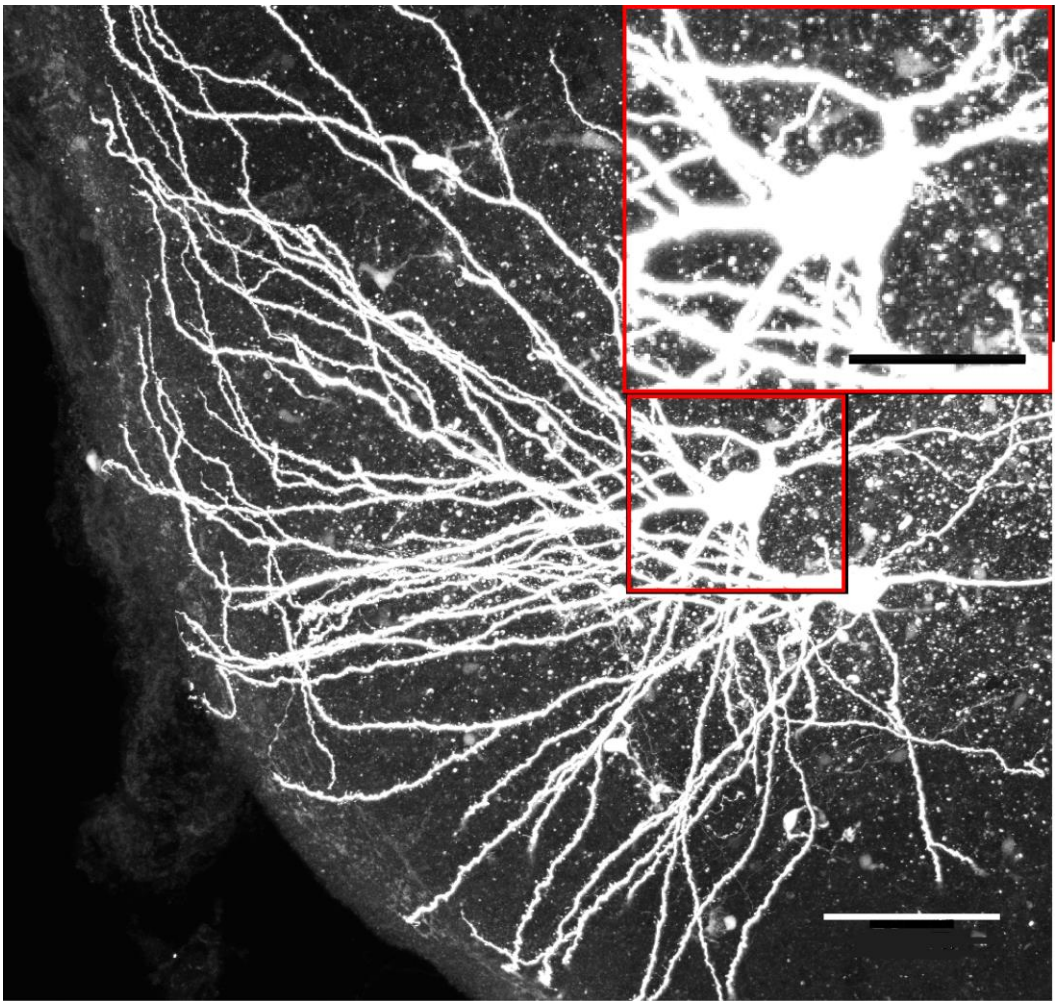

Figure 3.2.5. A 40xoil maximum z-stack projection confocal image, which shows the large fusiform somata of multiform cells. It also shows how the dendrites follow the edge of the pial surface. The image in the red box is a magnified (2x) image of the soma of the multiform cell. Scale bar = 50 µm for the large image and 25 µm for the box.

Oblique Pyramidal cells

The oblique pyramidal cell group was the third most populated cell group (figure 3.1.1). These cells had a triangular (or pyramid) shaped soma (figure 3.2.7), and were tilted up to 90^{o} compared to a regular pyramidal cell, making its elongated side parallel to the pial surface. Some variance in this angle was also found, but they did not tilt their apical dendrites more than 90^{o} to the pial surface, but rather less (some were found at approximately 45^{o} tilted, see figure 3.2.7). The apical and basal dendritic tree domains were

polarized as in the regular pyramidal cell (see figure 3.2.6), but there were more primary dendrites emerging from the cell body in the case of the oblique pyramidal cell.

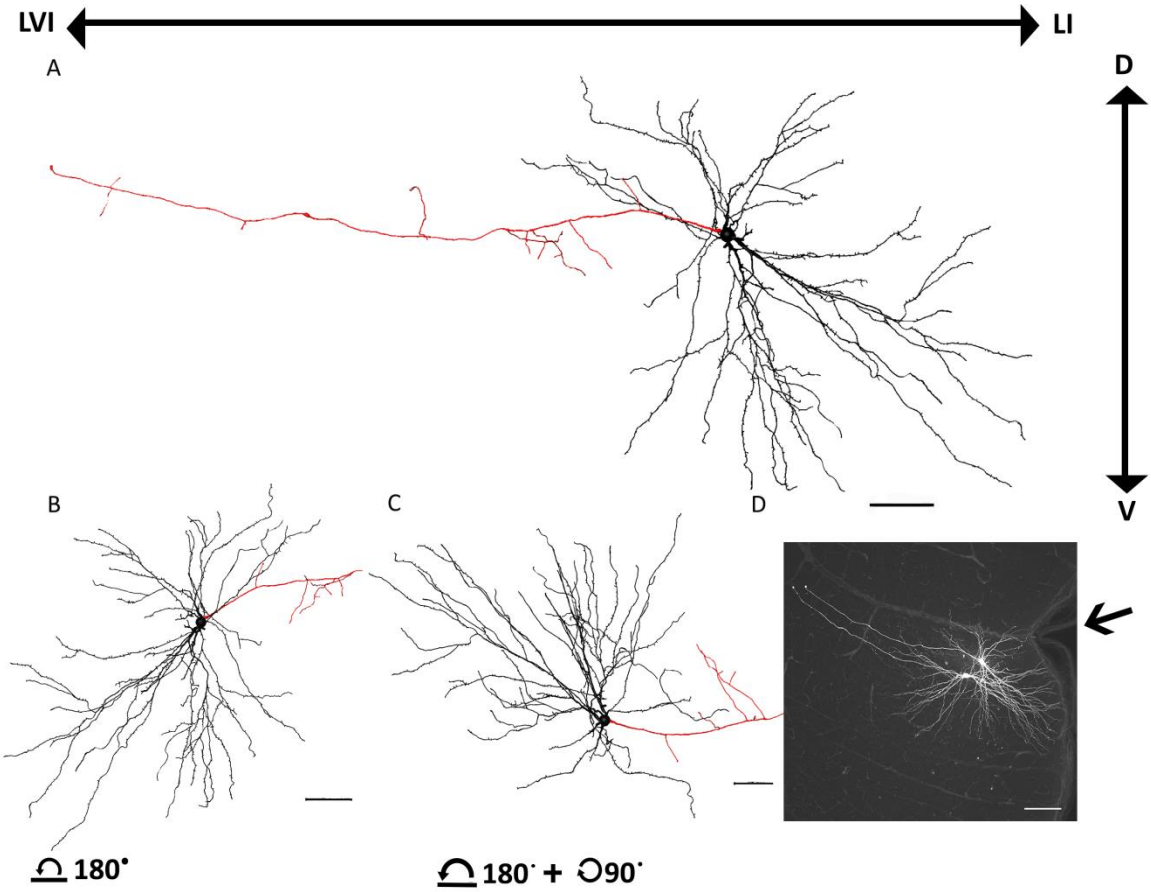

Figure 3.2.6. 3D reconstruction of an oblique pyramidal cell, axon depicted in red. **A**: the full extent of the cell, in the xy plane, axon depicted in red. **B**: same cell flipped vertically (180°), **C**: same cell from a more lateral view (90° turn inwards in the plane from B). **D**: confocal image (10x) showing maximum z-stack projection view. Arrow indicates the position of the rhinal fissure. Scale bars: A = 50 µm, B = 50 µm, C = 40 µm, D = 100 µm.

The oblique pyramidal cells often had a primary dendrite extending out of their side, but this dendrite did not branch noteworthy. Also, the basal dendritic tree going towards LIII were found to be less extensive than the one going towards LI, and both remained mainly in LII. They all had spiny dendrites. The axon could be followed to the angular bundle whenever it was not cut, and had axon collaterals ramifying in layers I, II and III.

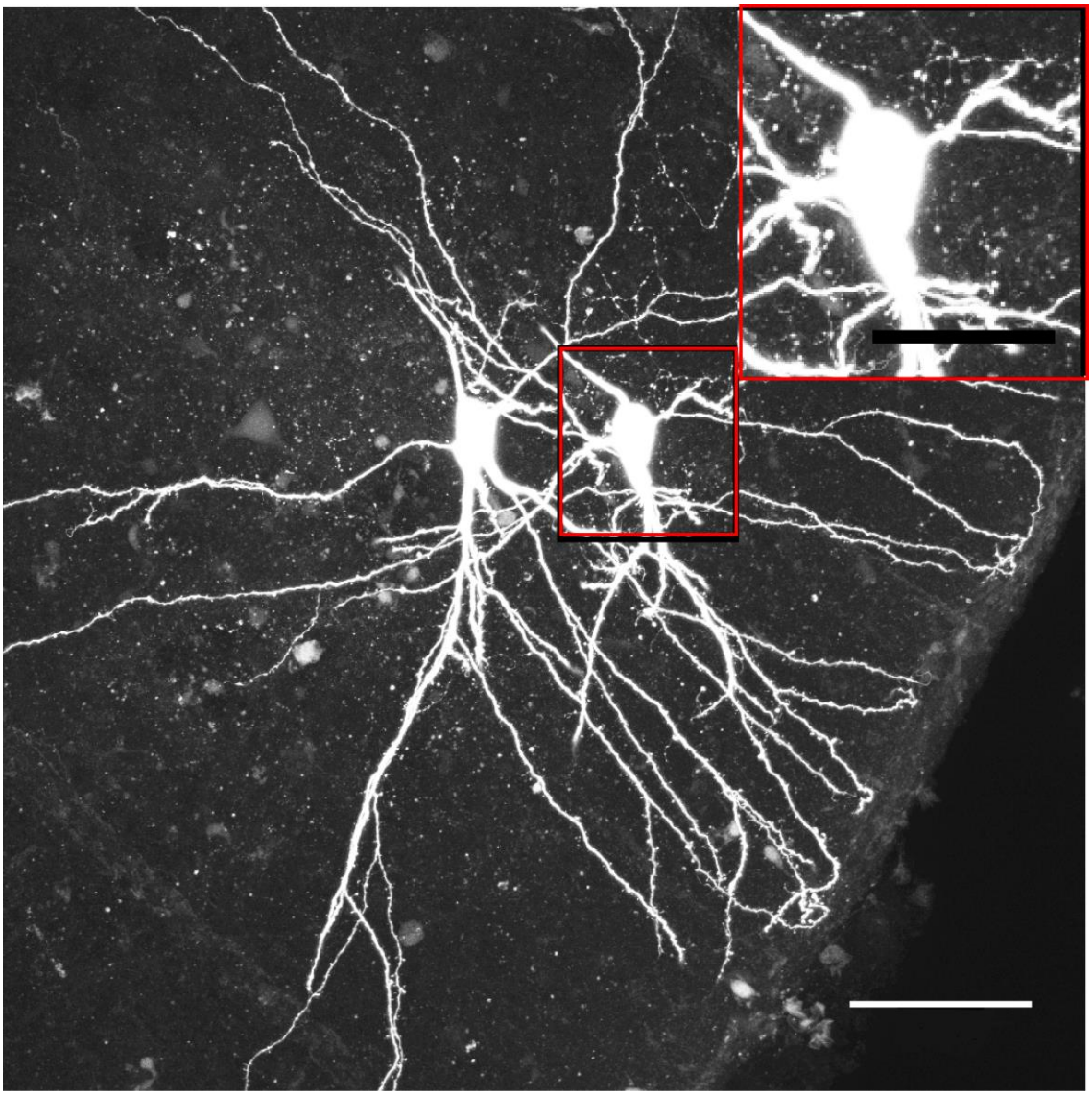

Figure 3.2.7. A 40xoil maximum z-stack projection confocal image, which shows an oblique pyramidal cells with a soma tilted at an approximately 45^{o} angle to the pial surface. Notice the one primary basal dendrite extending from the side of the cell body. Image in the red box is a magnified (2x) image of the soma of the oblique pyramidal cell. Scale bar = 50 µm for large image and 25 µm for box.

Pyramidal cells

The pyramidal cell comprised the least populated group found in this study of LEC LII (figure 3.1.1). This cell type was well-characterized by its triangular (or pyramid) shaped soma, and a thick apical dendrite ascending straight towards the pial surface. The pyramidal cell had its apical and basal dendritic domains well separated from the elongated side of the cell body, showing a polarization in the emergence of primary dendrites. For illustrations, see figure 3.2.8 below.

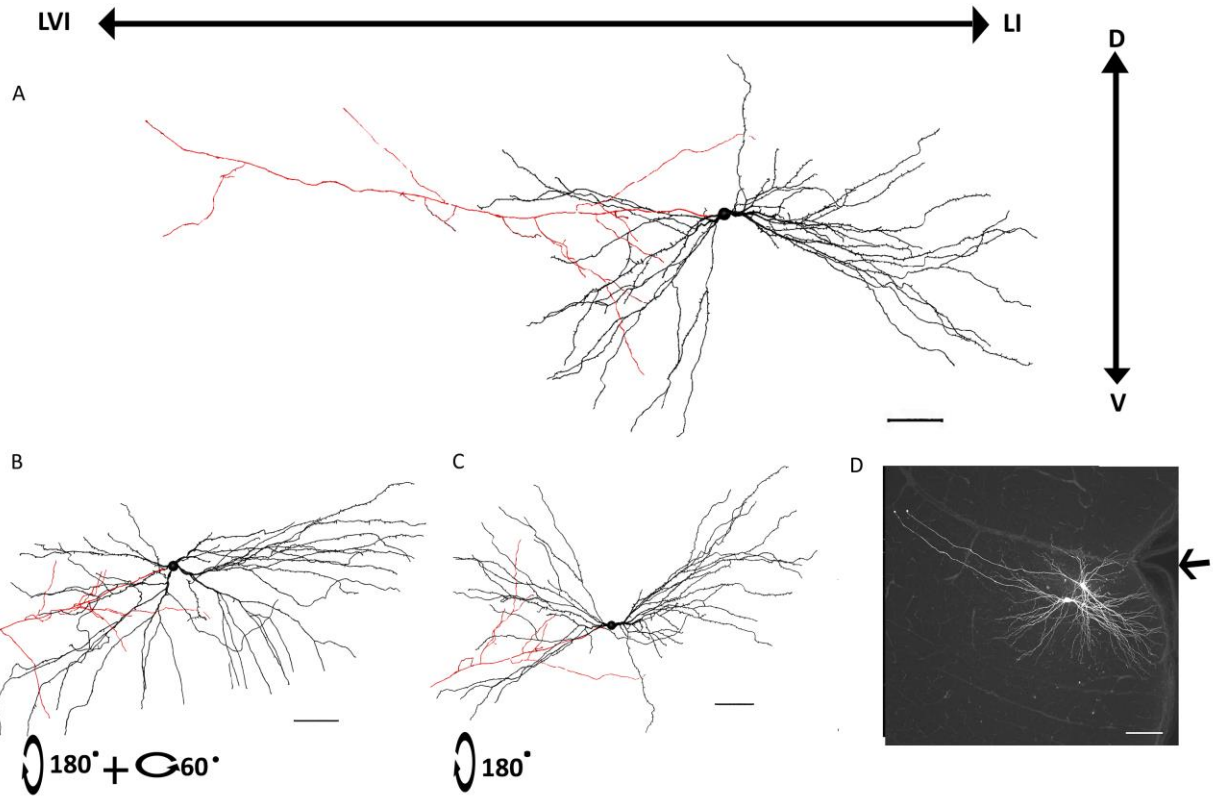

Figure 3.2.8. 3D reconstruction of a pyramidal cell, axon depicted in red. **A**: the full extent of the cell, in the xy plane, **B**: same cell as in A, from a lateral view with a vertical (180^{o}) and an outwards (60^{o}) flip, **C**: same cell flipped horizontally (180^{o}) from A. **D**: confocal image (10x) showing the z-maximal projection view. Arrow indicates the position of the rhinal fissure. Scale bars: A = 50 μm, B = 50 μm, C = 50 μm, D = 100 μm.

The somata were often found to be extra-elongated in some cases (see figure 3.2.9), and their dendritic domains remained separated such that the cell appeared polarized with no primary dendrites emerging from the side of the cell body. The apical dendritic tree was observed to reach the pial surface, whereas the basal dendritic trees remained in LII and LIII. The pyramidal cells were most often located deeper relative to the other cell types in LII (figure 3.1.2). The dendrites of the pyramidal cell were all spiny. The axon could be followed to the angular bundle whenever it was not cut, and was found to have collaterals in layers I, II and III. Three of the pyramidal cells were poorly filled with Biocytin, however, two of these still had acceptable electrophysiological recordings. One such poorly filled pyramidal cell is shown in figure 3.4.6.

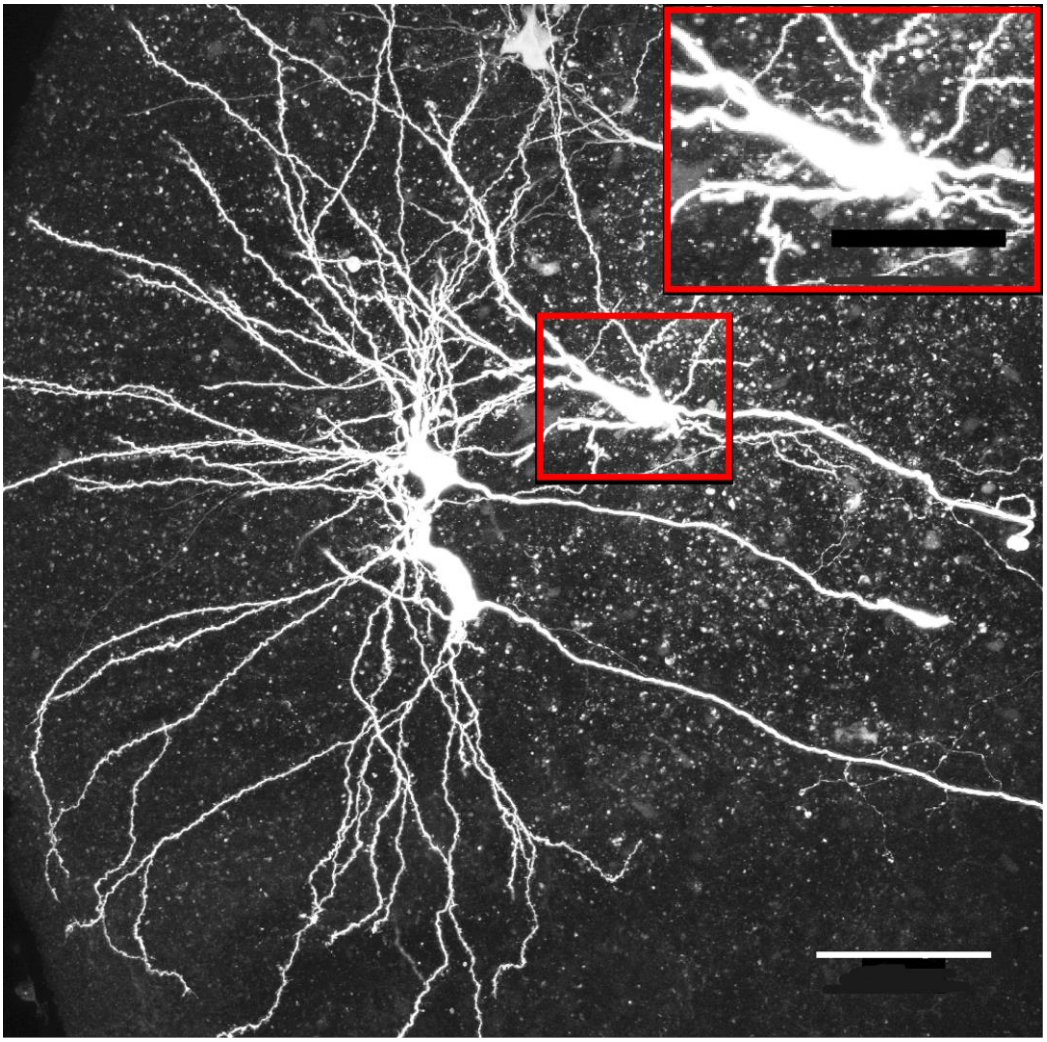

Figure 3.2.9. A 40xoil maximum z-stack projection confocal image, which shows an elongated pyramidal cell with a thick apical dendrite branching close to the soma. Image in the red box is a magnified (2x) image of the soma of the pyramidal cell. Scale bar = 50 µm for the large image and 25 µm for the box.

3.3. Electrophysiology

Electrophysiological parameters clustered based on cell types

The electrophysiological parameters varied within and across cell types, and no emergent property appeared to signal any particular cell type along the course of looking through the raw data. The raw data is given as a voltage reponse over time to the different current injections, with one full sweep going from -400 to +500 pA. From visual inspection it was apparent that cells belonging to a particular cell type did not show a correlation for a specific parametric profile (figure 3.3.1). This means that there is no recognizable electrophysiological "fingerprint" for the fan, multiform, oblique pyramidal or pyramidal cell. This observation was supported by no statistically significant differences between morphological cell types with respect to the individual electrophysiological parameters. The parameters that were calculated were the resting membrane potential (RMP), action potential (AP) threshold, input resistance (R_I), sag ratio, rebound, time constant (τ) and interspike interval (ISI) ratio. For the normally distributed parameters (RMP, R_I, Sag ratio, τ and ISI ratio) a MANOVA was performed with results taken to be significant when $p<0.05$. For the AP threshold and rebound values a nonparametric Kruskal Wallis test was run with results taken to be significant when $p<0.05$.

The results after the calculation of the RMP, AP threshold, R_I, sag ratio, rebound, τ and ISI ratio for the 90 cells are presented in figure 3.3.2. The RMP, AP threshold and sag ratio showed the least amount of variation within and across cell types (RMP: -69 mV to -71.2 mV; AP threshold: -46.4 mV to -47.3 mV; sag ratio: 0.93 to 0.94). The R_I, rebound, τ and ISI ratio were found to vary more within and across cell types (R_I: 102.1 MΩ to 132.8 MΩ; rebound 3.5 mV to 4.3 mV; τ: 24.5 ms to 28.5 ms; ISI ratio: 0.46 to 0.50). The sag ratio, ISI ratio and AP threshold for individual cells show as much difference between individual cells as between the cell groups (figure 3.3.1). Sometimes the hyperpolarizing current injection induced a spike on the rebound, as depicted in figure 3.3.1 A (bottom), C (bottom) and D (bottom). This behavior was seen for all cell types. However, it was only observed in a few cells, and was usually not consistent throughout the recordings.

None of the recorded cells were connected to each other, which was evident in that no injected cell triggered an excitatory post-synaptic potential (EPSP) in any other recorded cell.

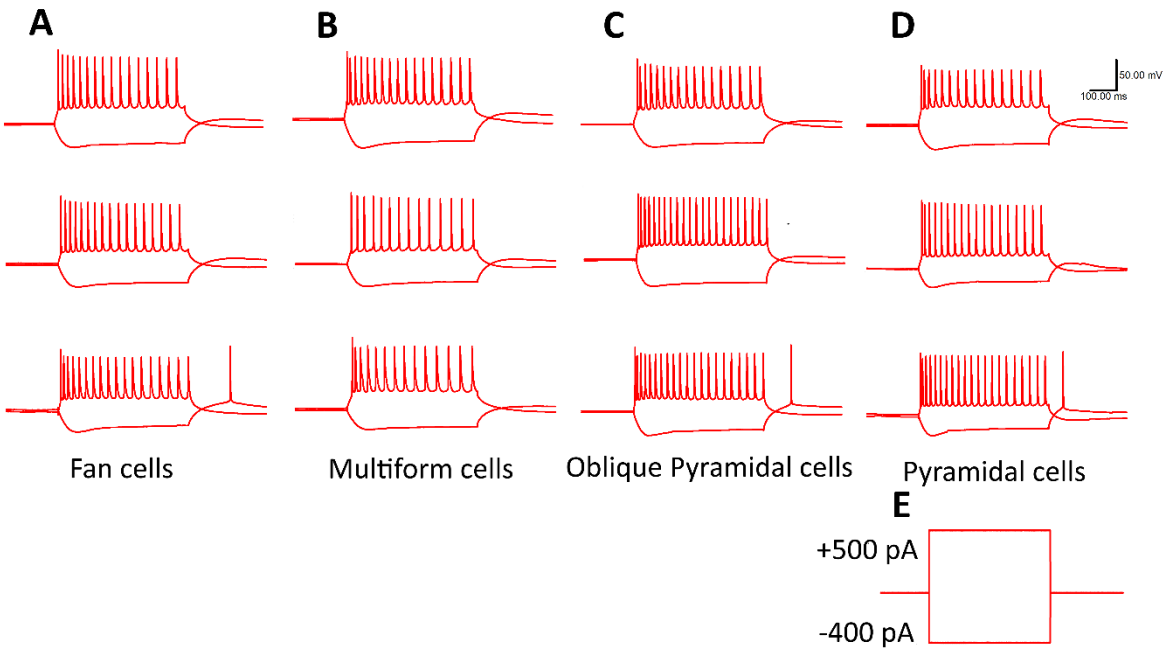

Figure 3.3.1. The voltage-current responses of the different cell types taken at the -400 pA and the +500 pA current injections. Scale bar for A, B, C, D = 100 ms, 20 pA. **A**: three fan cell responses, **B**: three multiform cell responses, **C**: three oblique pyramidal cell responses, **D**: three pyramidal cell responses. **E**: injection profile of the -400 pA and +500 pA current injections, total of 500 ms duration.

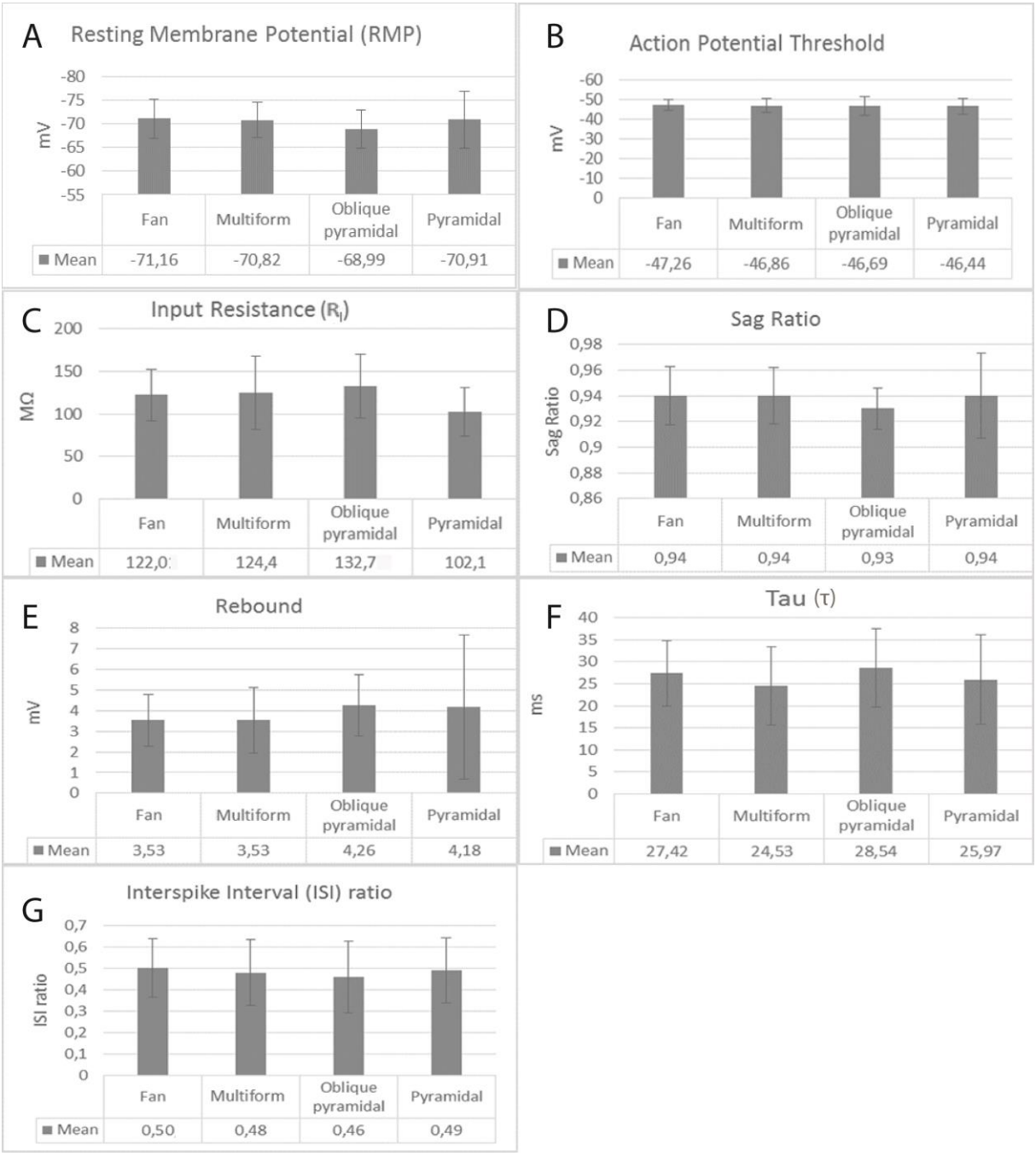

Figure 3.3.2. The electrophysiological parameters for each cell type, distributed by Fan (n=48), Multiform (n=18), Oblique pyramidal (n=14), Pyramidal (n=10). Results are given as means with error bars showing standard deviations. **A**: resting membrane potential, **B**: action potential threshold, **C**: input resistance, **D**: sag ratio, **E**: rebound, **F**: time constant (tau), **G**: interspike interval (ISI) ratio.

Electrophysiological recordings clustered based on position along the anterior-posterior axis

In order to look for possible differences in electrophysiological properties along the anterior-posterior axis of LEC LII, individual electrophysiological parameters were grouped based on the neurons relative position in the anterior-posterior axis, irrespective of their cell type. This grouping was performed by comparing the samples with Nissl stained sections (thickness of 50µm), using four Nissl sections for each bin. This procedure resulted in three bins that were 800 µm apart (see section 2.6 for details). Table 3.3.1 shows which slice number belonged to which anterior-posterior position bin.

Table 3.3.1. An overview of the anterior-posterior position of the recorded slices, grouped into the three bins: posterior, intermediate and anterior.

Posterior	Intermediate	Anterior
141001_2	141001_3	141002_4
141002_1	141002_2	141112_4
141112_2	141002_3	141113_4
141112_1	141112_3	141127_4
141113_1	141113_3	150220_3
141127_1	141113_2	
141127_2	141127_3	
141203_1	141203_3	
141203_2	141204_3	
141204_1	141203_4	
141211_2	141204_2	
141211_1	141211_3	
150108_1	141211_4	
150108_2	150108_3	
150212_1	150108_4	
150212_3	150211_1	
150220_1	150212_2	
141204_4	150220_2	

The information about the position of the slices in the anterior-posterior axis was then used to group the electrophysiological data, to see if there were any major differences along this axis. This grouping was done using the posterior group cells (n=43), the intermediate group cells (n=36) and the most anterior group cells (n=11). A test for normality showed two outliers for rebound. After these two had been removed from the set in total, a MANOVA was performed. This showed a significant difference ($p<0.05$) along the axis for the ISI ratios, between the most posterior, intermediate and anterior cells. The mean ISI ratio values were 0.45 for the posterior group, 0.50 for the intermediate group and 0.63 for the anterior group. The most significant difference was between the anterior sections and the posterior sections ($p < 0.001$), but also between the anterior sections and the intermediate sections ($p = 0.015$). No significant difference was found between the posterior sections and the intermediate sections ($p = 0.398$). No significant differences were found for the other parameters.

3.4. Immunohistochemistry

Test results and controls

Once the preliminary immunotests were performed using an initial protocol established in the laboratory, a series of tests were performed (see table 7.1. in appendix 7.4 for overview). The initial protocol was optimized for thin sections (40µm-100µm) and not the thick 400µm slices that are used for patch clamp recordings. Details on tests and controls that were performed before a finalized protocol was established are given in the appendix (section 7.4).

Distribution of Calbindin and Reelin immunoreactive neurons

CB-IR cells were mainly seen as a scattered, broad band located in deep LII/superficial LIII (figure 3.4.1). Some variability was seen in the number of stained cells, and this often affected how broad the band of CB-IR cells was. Generally, a lot of neurites were also stained. This latter type of staining surrounded cells that were not CB-IR (see G in figure 3.4.3 – 3.4.7). The staining of the soma was different for the CB-IR and Reelin-IR cells. Whereas the CB stain covered the entire soma of smaller cells, the Reelin stain seemed to be mainly periakyron in cells that were generally larger than the CB-IR cells.

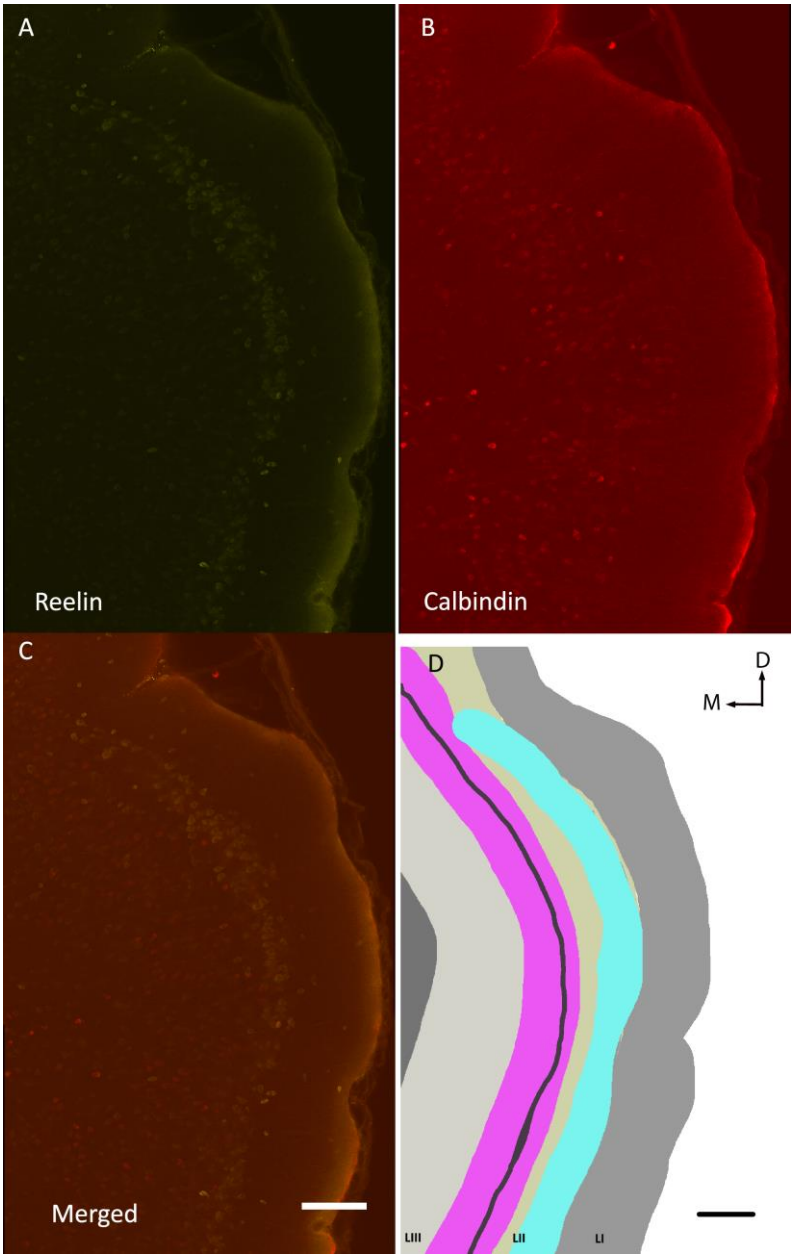

Figure 3.4.1. Distribution of the immunostained cells in the superficial layers of LEC. **A**: Reelin distribution, **B**: CB distribution, **C**: merged image of A and B. Scalebar = 100 µm. **D**: Cartoon figure of the distribution of Reelin (cyan) and CB (magenta). The black line is the border between LII and LIII. D = dorsal, M = medial. Scale bar = 100 µm.

Reelin-IR cells were seen in all layers of LEC, with the strongest and most prominent labeling in superficial LII (figure 3.4.1). There was little labeling, if any, directly adjacent to the strong band, and uniformly weaker labeling deeper to LIII. The Reelin stain seems to be absent in what is assumed to be the perirhinal cortex directly adjacent to the endpoint of the Reelin

stain in figure 3.4.1(A,D), whereas the CB stain continues a bit further across the rhinal fissure in figure 3.4.1(B,D). The distribution of CB and Reelin is not confined in perfectly restricted bands, as shown in figure 3.4.2. Notice that there are some CB-IR neurons in the more superficial part of LII as well, as the CB stain is more scattered than what figure 3.4.1.D gives the impression of. However, the general band still remains at the LII/LIII border. It is also apparent in the merged image (figure 3.4.2.A) that there is a gap between the most intense Reelin-IR band and the most intense CB-IR band, and that this gap is most evident towards the most dorsal border of LEC (close to the rhinal fissure).

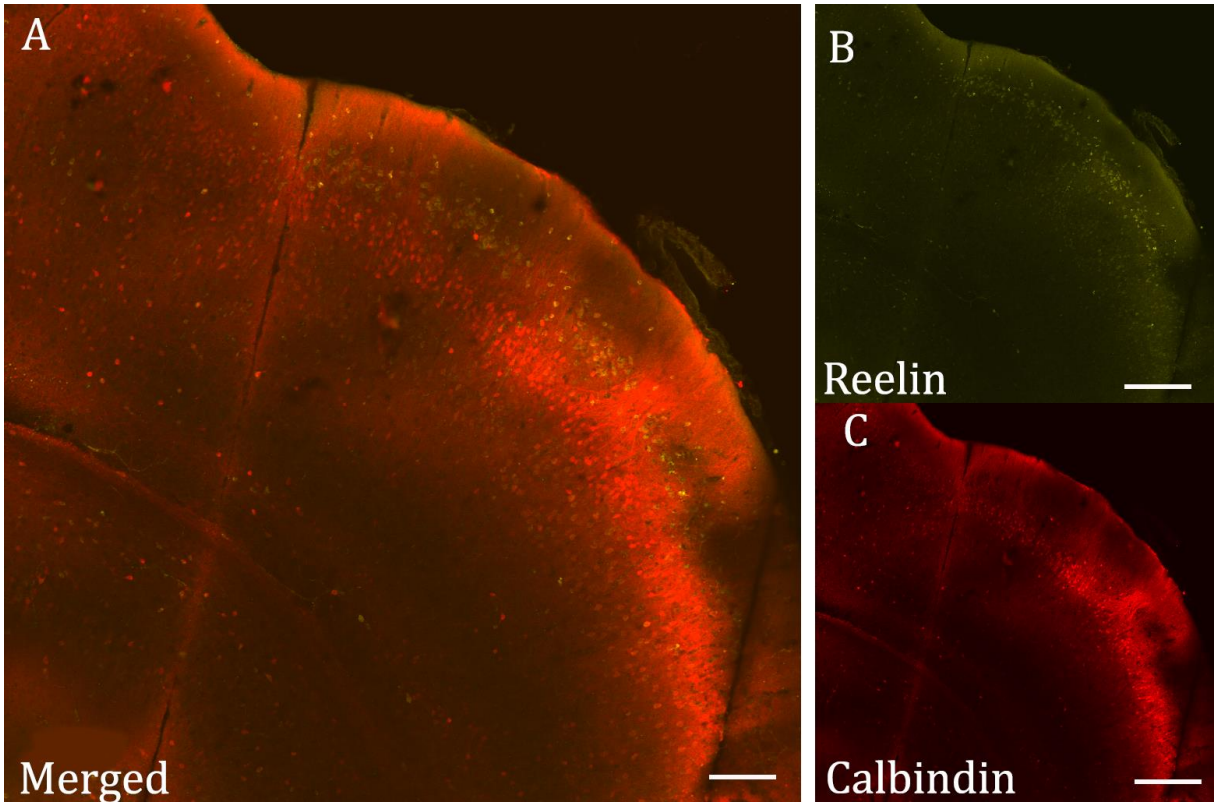

Figure 3.4.2. 10x confocal images of Reelin and CB immunoreactivity. **A**: a merged image of both Reelin and Calbindin, scale bar = 100 µm. **B**: the distribution of Reelin in superficial LII, scale bar = 200 µm, **C**: the distribution of CB in deep LII/superficial LIII, scale bar = 200 µm.

Colocalization of immunoreactivity

The determination of colocalization was done by looking at 63xoil confocal images, using all three channels to visualize Biocytin, CB and Reelin IR cells. 102 out of the total 104 cells that had been morphologically identified were Reelin-IR and not CB-IR. The analysis clearly showed that Reelin-IR cells are found among all principal cell types, including fan cells (figure 3.4.3), multiform cells (figure 3.4.4), oblique pyramidal cells (figure 3.4.5) and pyramidal cells (figure 3.4.5) in LEC LII. The remaining two cells that did not show IR to neither Reelin nor CB, were identified as a pyramidal cell (figure 3.4.6) and a fan cell (figure 3.4.7).

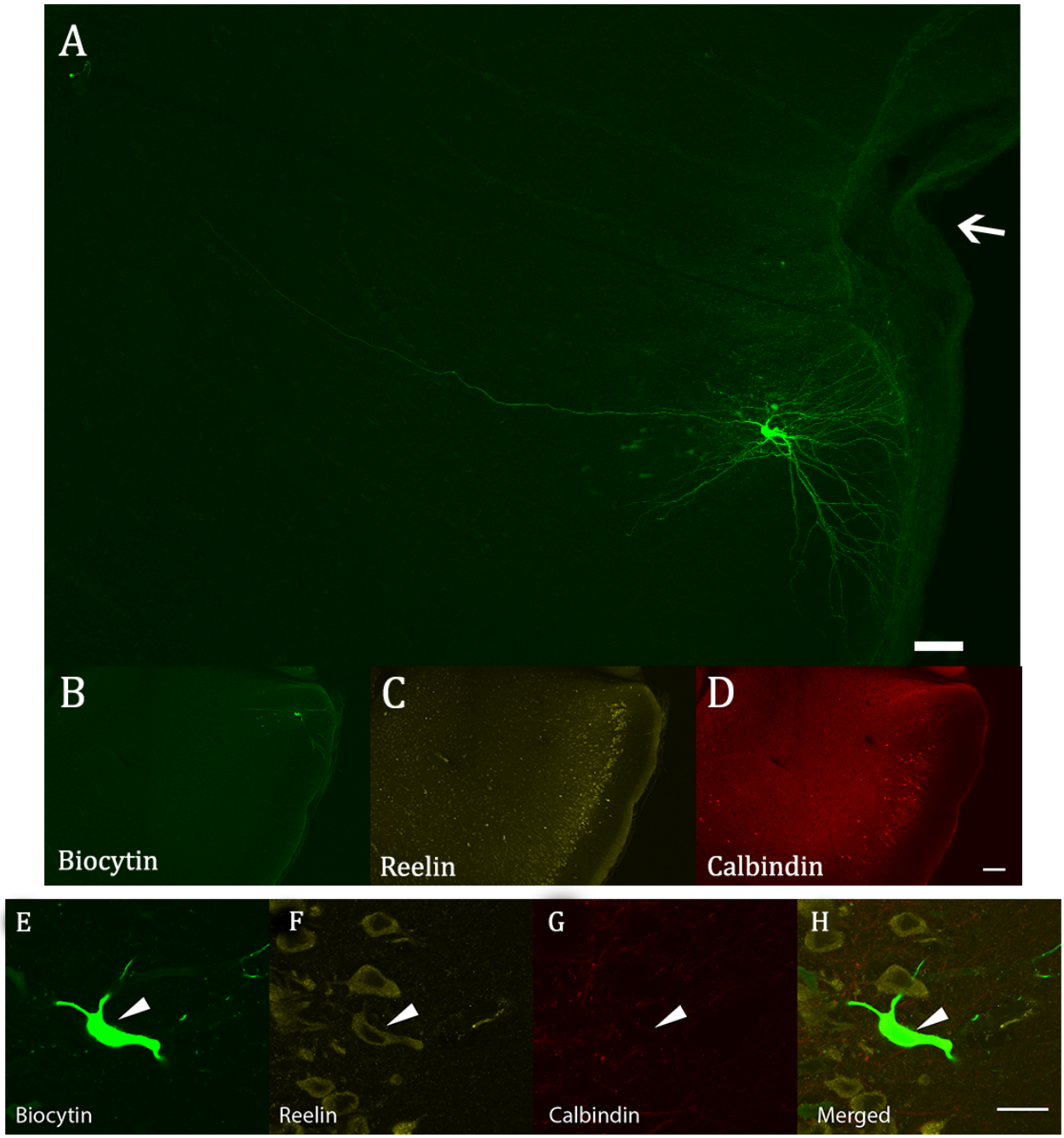

Figure 3.4.3. A-D: 10x confocal images showing **A:** the maximal projection view of a fan cell**.** Arrow indicates the position of the rhinal fissure**. B:** the same image as in A, just in one plane, showing the Biocytin labeling of the cell. **C**: same image-plane as in B, showing the Reelin distribution**. D**: same image-plane as in B and C showing the CB distribution. Scale bar A = 50µm, scale bar B, C, D = 100 µm. **E-H:** 63xoil confocal images of the colocalization of Biocytin and Reelin. **E**: Biocytin, **F**: Reelin, **G**: Calbindin, **H**: Merged. This fan cell is Reelin-IR but not CB-IR. Scale bar = 20 µm.

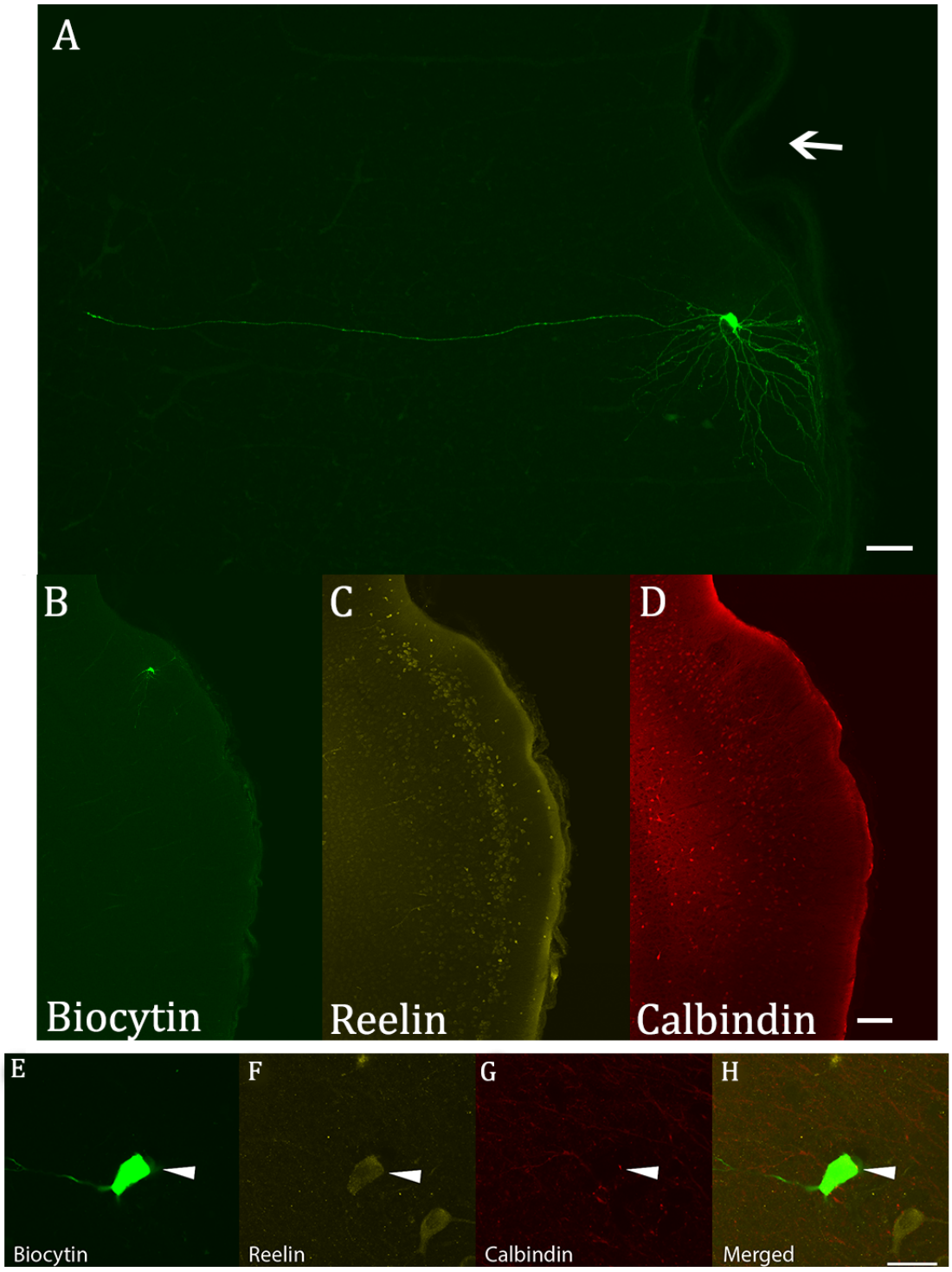

Figure 3.4.4. A-D: 10x confocal images showing **A:** the maximal projection view of a multiform cell**.** Arrow indicates the position of the rhinal fissure. **. B:** the same image as in A, just in one plane, showing the Biocytin labeling of the cell. **C**: same image-plane as in B, showing the Reelin distribution**. D**: same image-plane as in B and C showing the CB distribution Scale bar A = 50µm, scale bar B, C, D = 100 µm. **E-H**: 63xoil confocal images of the colocalization of Biocytin and Reelin. **E**: Biocytin, **F**: Reelin, **G**: Calbindin, **H**: Merged. This multiform cell is Reelin-IR but not CB-IR. Scale bar = 20 µm.

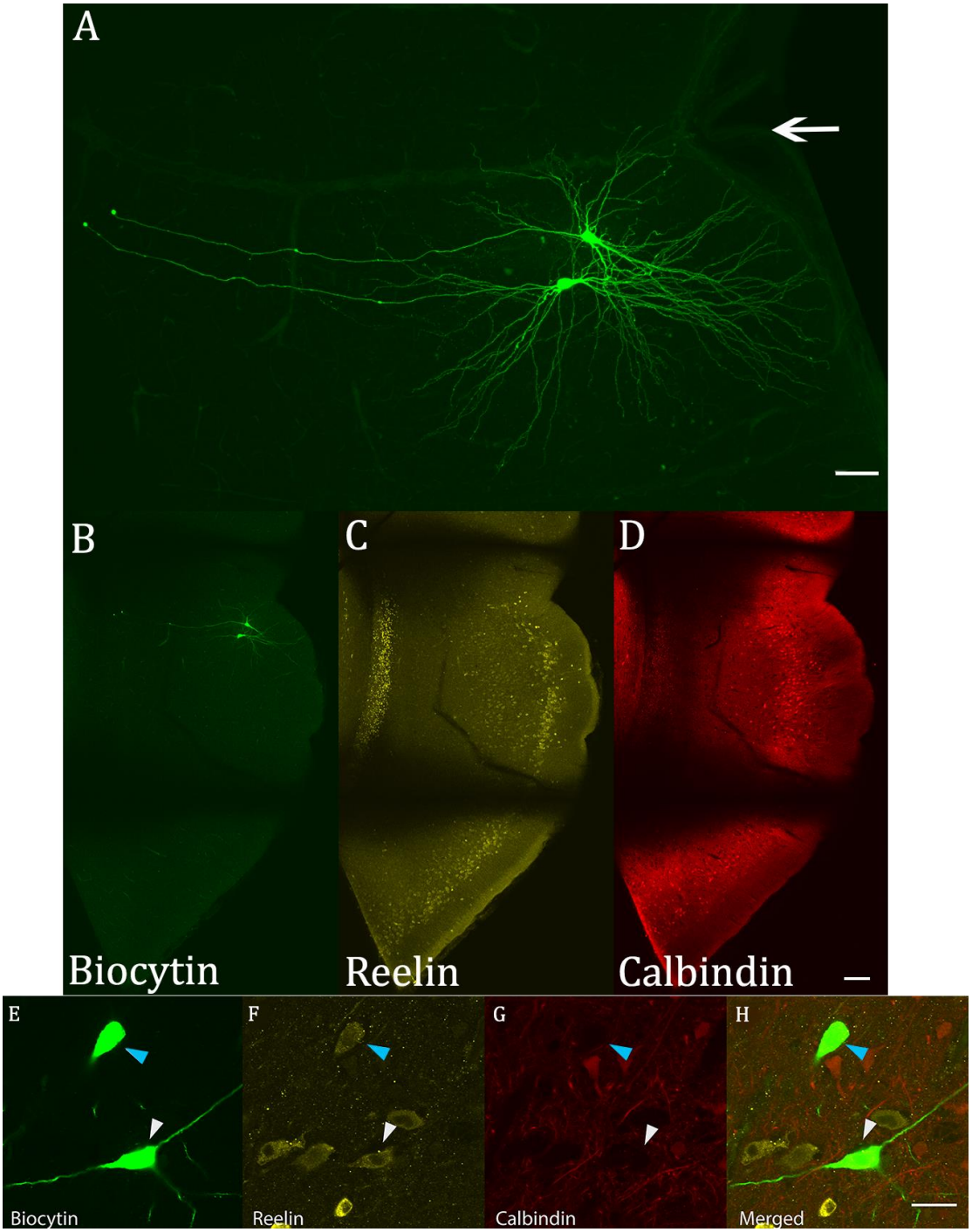

Figure 3.4.5. 10x confocal images showing **A:** the maximal projection view of an oblique pyramidal and a pyramidal cell**.** Arrow indicates the position of the rhinal fissure**. B:** the same image as in A, just in one plane, showing the Biocytin labeling of the cell. **C**: same image-plane as in B, showing the Reelin distribution**. D**: same image-plane as in B and C showing the CB distribution. Scale bar A = 50µm, scale bar B, C, D = 100 µm. **E-H:** 63xoil confocal images of the colocalization of Biocytin and Reelin for the pyramidal (cyan arrowhead) and the oblique pyramidal (white arrowhead) cell. **E**: Biocytin, **F**: Reelin, **G**: Calbindin, **H**: Merged. The oblique pyramidal and pyramidal cells are Reelin-IR but not CB-IR. Scale bar = 20 µm.

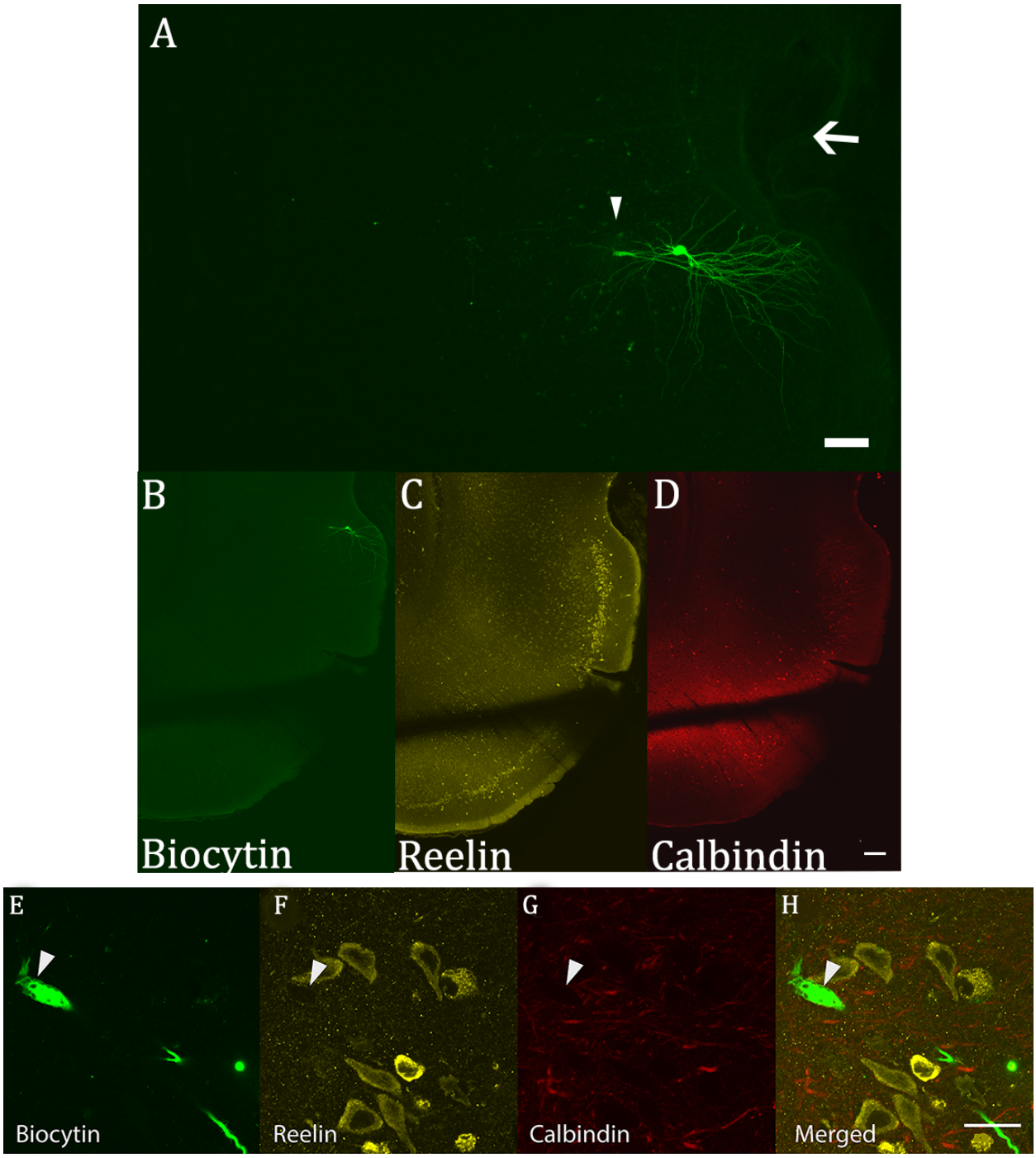

Figure 3.4.6. A-D: 10x confocal images showing **A:** the maximal projection view of a pyramidal (arrowhead) and fan cell**.** Arrow indicates the position of the rhinal fissure. **B:** the same image as in A, just in one plane, showing the Biocytin labeling of the cell. **C**: same image-plane as in B, showing the Reelin distribution**. D**: same image-plane as in B and C showing the CB distribution. Scale bar A = 50µm, scale bar B, C, D = 100 µm. **E-H:** 63xoil confocal images of a pyramidal cell that shows no immunoreactivity to either Reelin or CB. **E**: Biocytin, **F**: Reelin, **G**: Calbindin, **H**: Merged. Scale bar = 20 µm.

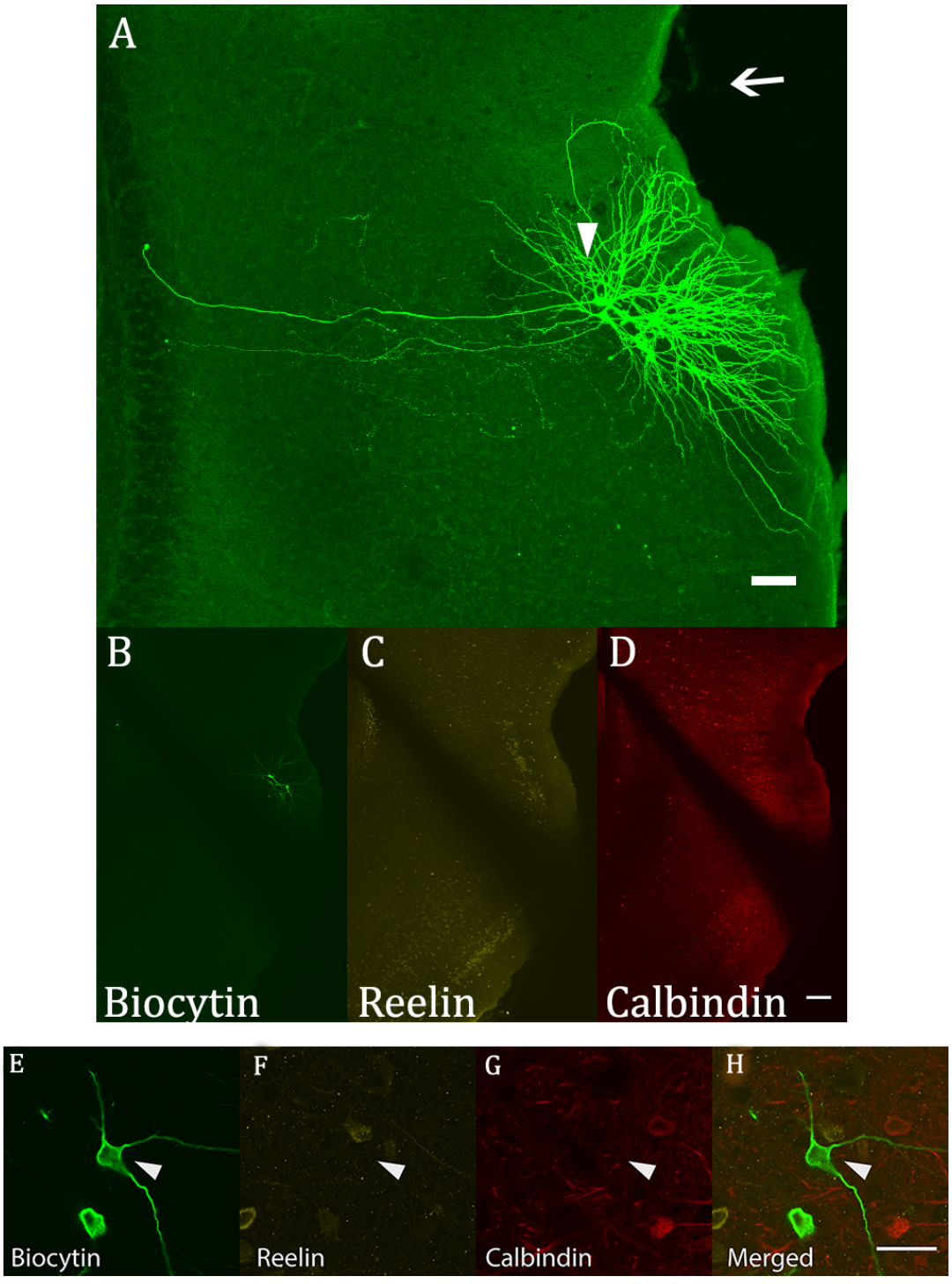

Figure 3.4.7. **A-D**: 10x confocal images showing **A:** the maximal projection view of two fan cells and two multiform cells**.** Arrow indicates the position of the rhinal fissure. **B:** the same image as in A, just in one plane, showing the Biocytin labeling of the cell. **C**: same image-plane as in B, showing the Reelin distribution**. D**: same image-plane as in B and C showing the CB distribution. Scale bar A = 50µm, scale bar B, C, D = 100 µm**. E-H**: 63xoil confocal images of a fan cell (arrowhead in A) that shows no immunoreactivity to either Reelin or CB. **E**: Biocytin, **F**: Reelin, **G**: Calbindin, **H**: Merged. Scale bar = 20 µm.

4. Discussion

The main findings in this study are three-fold. Firstly, it was shown that the morphologically defined classes of principal cells in LEC LII displayed variations within each group, be that of dendritic and somatic tilting, branching patterns or somatic shape. Also, two subclasses of fan cells were suggested. Secondly, it was shown that the four different principal cell types of LEC LII cannot be separated by their electrophysiological parameters. Lastly, 102 cells were found to be Reelin-IR and not CB-IR, irrespective of the class of neurons they belonged to. Two cells were reported as not showing immunoreactivity to either marker.

4.1. Morphological variations within principal cell types of LEC LII

Not surprisingly, none of the 104 characterized cells were morphologically identical. Where one draws the line between actually separating them into different cell types, is of course debatable, and with each cell group type showing variations, it is definitely difficult to discretize them. In this study, the fan cell, multiform cell, oblique pyramidal cell and pyramidal cell were identified. The fan, multiform and pyramidal cell, have already been described by several authors (Schwartz and Coleman, 1981, Germroth et al., 1989b, Lingenhohl and Finch, 1991, Tahvildari and Alonso, 2005, Canto and Witter, 2012b, a). The oblique pyramidal cell type was later included as one of the four principal cell types in LEC LII (Canto and Witter, 2012a), and it was clear that cells in this study fitted this description as well. The fan cells in this study were divided into two subclasses, namely the spherical fan cells and the parachute fan cells. The names are based on their somatic features, but they also differed in dendritic distributions. No other obvious subclass was identified. Nevertheless, an open description of cell types with differences in somatic shape, dendritic tilt, and branching patterns, can lead to new classifications further down the road, as it helps bring up the number of characterized cells.

Fan cells

The fan cells were the most numerous morphologically identified cell type, comprising 54% of the recorded cells, which is well in line with previous studies (Schwartz and Coleman, 1981, Tahvildari and Alonso, 2005, Canto and Witter, 2012a). The fan cells were generally easy to recognize, due to their fanning appearance and lack of basal dendrites. Also, the few fan cells that were situated directly adjacent to the rhinal fissure had a radially restricted extent and angle of their dendritic domain, in that their dendritic tree avoided the fissure completely (figure 3.2.2.). This could have a purpose in segregating input coming to EC LI and input coming to the adjacent perirhinal cortex LI, as perirhinal cortex itself has a strong projection to LEC LII (Burwell and Amaral, 1998a, b). It could also be due to neurotrophic factors, causing the dendrites to follow a chemical gradient (Ascoli and Samsonovich, 2002). It would be interesting to see if the perirhinal cortex cells' dendritic trees close to the rhinal fissure are also repelled by its presence.

The fan cells also showed differences with respect to their somatic shape, and displayed typically either a parachute-shaped or spherical cell body. This difference made it possible to separate the fan cells into the two subclasses of spherical-fan cells and parachute-fan cells. The fact that the parachute-fan cell appears to have more horizontal processes and that the spherical-fan cell appears to be more radially restricted (figure 3.2.3), could be similar as to why there are oblique (horizontal) pyramidal cells and (vertical) regular pyramidal cells in LEC LII. Similar differences in tilting and somatic shape have been reported previously, showing two similar examples of fan cells to those presented in this study (Schwartz and Coleman, 1981). A role of the fan cells being restricted to LI and LII could be to serve as the main recipients for olfactory input (Wouterlood and Nederlof, 1983), and to employ spatiotemporal coding by covering a great area of LI to increase combinatorial responses to this incoming olfactory information. This could be supported by the findings that olfactory bulb input terminates onto fan cells (called stellate cells of LEC in the article) of LEC LII, from where it was further projected to the hippocampus (Schwerdtfeger et al., 1990). Such direct sensory input to the EC is rare, as most of the input gets preprocessed and premodulated via presubiculum, perirhinal and postrhinal cortices (Vogt and Miller, 1983, Room and Groenewegen, 1986, Witter et al., 1986, Suzuki and Amaral, 1994, Burwell and Amaral,

1998b) If fan cells are the sole attributes of olfactory information to the hippocampus, and LEC LII cells are especially debilitated in the course of Alzheimer's disease (Braak and Braak, 1985), then the olfactory dysfunction seen in Alzheimer's disease might be due to pathological changes in fan cells (Kovacs et al., 2001, Wilson et al., 2007).

Multiform cells

The multiform cell type constituted the second most populated cell group in this study, with 18%. This is less than expected from previous studies (Schwartz and Coleman, 1981, Tahvildari and Alonso, 2005, Canto and Witter, 2012a), but might be due to the percentages skewed for the lower cell-count studies. The multiform cells exhibited differences in somatic shape, but they were all fusiform, in that no decisive shape could be distinguished, and the amount of primary dendrites extending at all 360^{o} made the soma distorted in all directions. The multiform cell is said to resemble the stellate cell in morphology (Tahvildari and Alonso, 2005), however, it is probably an even more diffuse cell type class than the stellate cells, as all cells with no preferred polarization were grouped into this class (Canto and Witter, 2012a). Having dendrites radially distributed over the extent of the soma could make the multiform cells better suited to function as cellular integrators, than cells showing a preferred direction of their dendrites (Canto, 2011). This is because they could effectively integrate information coming from all directions, and probably why interneurons that are similar to the multiform neurons, are abundant in both the central and peripheral nervous system (Markram et al., 2004, Kandel et al., 2013). However, cellular integrators such as the multipolar cells, are usually considered to be operating in a local network, and are not nearly as large as the multiform projection cells of LEC LII, so it remains to be seen what kind of importance the multiform neurons could serve.

Oblique Pyramidal cells

There were almost as many oblique pyramidal cells as there were multiform cells, coming in as the third most common cell type in LEC LII at 17%. The oblique pyramidal cell constitutes a surprisingly clear cell type group, and has also been described in other cortical areas such as the visual cortex (Peters and Kara, 1985). These cells have most likely also been described

in older studies of LEC LII, although in these studies they are referred to as “horizontal bipolar” cells (Schwartz and Coleman, 1981, Schwerdtfeger et al., 1990). The oblique pyramidal cells in this study were often situated right at the border between LI and LII (figure 3.1.5), as if making a horizontal barrier by this border. This was also described in a previous study of the horizontal bipolar cells being situated at the LI/LII border (Schwerdtfeger et al., 1990). The orientation of the cells varied, but was mainly found to be parallel to the pial surface, even when the cells curved up in the fissure. The fact that oblique pyramidal cells can have more primary dendrites, and even were observed to have dendrites extending from the side of the soma, makes them a bit more complex than being just a regular pyramidal cell tilted some angle.

Pyramidal cells

The pyramidal cells were the least numerous cell type in this study, amounting to only 11 % of the filled cells, which is a little less than previously reported (Schwartz and Coleman, 1981, Tahvildari and Alonso, 2005, Canto and Witter, 2012a). This is probably due to the fact that only quite superficial cells were recorded from in this study, whereas the others recorded from the entire depth of the layer, even including some ectopic LII cells that were found in LIII (Tahvildari and Alonso, 2005, Canto and Witter, 2012a). By looking at figure 3.1.5 it also becomes evident that the pyramidal cells recorded in this study were located more deep within layer II. The pyramidal cells were found to vary in elongation of the soma (figure 3.2.9). Since there were only 11 pyramidal cells in this study, of which three were incompletely filled with Biocytin, no other pattern was noted. Despite the incomplete filing of these three neurons, it was however still clear that they were pyramidal cells. This was because the proximal dendrites and soma holds cell-type specific features with their triangulated soma and primary dendrites following this triangulation by spanning outwards from the three vertices.

The pyramidal cell of LEC LII is a more typical-looking pyramidal cell than what has been found in MEC LII, as the MEC LII pyramidal cells have been described to have a horizontally tilted apical dendrite (Tahvildari and Alonso, 2005). The pyramidal cells of LEC and MEC LII also differ electrophysiologically (Klink and Alonso, 1997, Canto and Witter, 2012b, a). Generally, there exist a wide range of pyramidal cells in the cortex, with different dynamics and functions. One mechanism that is known to be in pyramidal cells elsewhere in cortex, is that of being a coincidence-detector. This is caused by several small dendritic potentials that sum up and evokes an action-potential firing when combined at the same space and time (Spruston, 2008). Such a property is widespread in the cortex and pyramidal cells, and it allows neurons to synchronize and integrate dispersed information into coherent representational arrangements (Konig et al., 1996).

4.2. Principal neurons in LEC LII cannot be distinguished based on electrophysiology

The cells in this study could not be separated based on their electrophysiology alone. This is in line with what was reported by Canto & Witter 2012a, but not in line with what was reported by Tahvildari & Alonso 2005. In the cerebrum in general, it is common for cells to show a correlation between morphology and electrophysiology, for instance among retinal ganglion cells (Barres et al., 1988), pyramidal cells of prefrontal cortex (Yang et al., 1996), or even within MEC LII (Canto and Witter, 2012b). Sometimes the electrophysiological responses even make up distinct subpopulations within the same morphological class as shown, for instance, in the medial mammillary body (Alonso and Llinas, 1992). However, it is not unique to LEC LII cells to not show a correlation between morphology and electrophysiology, as the rest of the layers of EC (excluding MEC LII) have also shown a lack of correlation between morphology and electrophysiology (Hamam et al., 2000, Hamam et al., 2002, Canto and Witter, 2012a, b). Thus, MEC LII pyramidal and stellate cells being separated based on electrophysiological parameters could be the exception, rather than the rule in the EC.

Values of the electrophysiological parameters that were studied are variant

The resting membrane potential (RMP) and action potential threshold (AP thresh) represent two basic, intrinsic neuronal properties. The RMP and AP thresh are often restricted to be within a certain physiological range, due to the equilibrium potentials of the ionic components controlling the RMP (Molleman, 2003), and the voltage-sensitivity of the S4 component of the voltage-gated sodium channels for the AP thresh (Bear et al., 2007). Responses that have been shown to vary between MEC LII and LEC LII are of a more complex and dynamic nature, and include the sag ratio, input resistance, and time constants, with the MEC LII cells displaying a more prominent sag ratio, a lower input resistance, and a shorter time constant than the LEC LII cells (Canto and Witter, 2012a, b). These variables do however exist in a gradient manner, between the MEC and LEC, such that cells close to the border appear to be intermediate (Canto and Witter, 2012b). This study only included the more dorsolateral part of the LEC (see figure 3.1.2. for overview of the position of the cells), so the cells responses in this study might represent the cellular responses of the most lateralized neurons, and not that of the more intermediate cells by the border. This is evident in that Canto & Witter (2012a) showed a prominent sag ratio (<0.80), whereas the sag ratio of this study was 0.94. However, there is also a difference as to how this was calculated, so it might not just be because of the position (Canto and Witter, 2012a). Other studies have claimed there is no sag in LEC LII principal cells (Jones, 1994, Empson et al., 1995, Wang and Lambert, 2003), which would make the LEC LII cells appear even more different from the MEC LII cells. The rebound values are related to the sag ratio values, as both are a result of I_h current due to the presence of HCN channels explained in section 1.5.1. The lower the sag ratio, the higher the rebound, which is evident in MEC LII neurons with prominent sag ratios having a rebound value greater than what is found in LEC LII neurons (Canto and Witter, 2012a, b). In this study, the rebound values were quite variable. The pyramidal cell group exhibited the greatest variance, with one cell having a rebound value of 12.38 mV and another with 0.72 mV. Sometimes the rebound was great enough to trigger an action potential (figure 3.3.2). However, as this did not occur on each sweep for the cells, it was still possible to calculate the rebound value for all but one cell.

The input resistance and time constant are both measures of how fast the neuron is able to respond to membrane alterations. For the input resistance, there actually seems to be a small difference in this study between the pyramidal and oblique pyramidal cells, with values of 102.1 MΩ and 132.8 MΩ respectively. However, no statistical difference was found, which could be due to the high standard deviation among the pyramidal cells. The values in this study were higher than for Tahvildari & Alonso, which showed an input resistance of around 50 MΩ. This is probably due to Tahvildari & Alonso using sharp pipettes, rather than patch pipettes as used here (Li et al., 2004, Brette and Destexhe, 2012). Canto & Witter who performed the experiments using the same set-up as this study, had a much higher input resistance (410 MΩ) which was probably due to how this was calculated. The time constant was also very variable, and could sometimes vary from run to run for the same cell. When looking at table 1.5.1 and figure 3.3.1 only one study differ notably from the rest with respect to the time constant, and that is the Wang & Lambert 2003 study, with a time constant of 43 ms. This difference is most likely due to calculational differences, as there are different methods to calculate the time constant. However, Wang & Lambert did not state how they calculated this variable, nor if they excluded any cells electrophysiologically.

A common way to separate cell types based on electrophysiological responses, is by looking at the firing patterns. I observed that the interspike-interval (ISI) interval seemed to differ from cell to cell, with the last ISI always being shorter than the first (see figure 2.2.1B). Such a firing pattern is referred to as spike frequency adaptation (SFA), which is caused by sustained excitatory stimulus causing the neuron to reduce its electrical activity (Hille, 2001). This reduction can be due to the actions of potassium channels that are activated by calcium influx (K_{Ca} channels) and these also underlie the afterhyperpolarization (AHP) that follows an action potential (Benda et al., 2005). For the values given in this study, in the range of 0.16 to 0.84, this was a hopeful parameter candidate to show cell type significance. This could then be attributed to differential expression of these K_{Ca} channels, and the functional differences that this implies. However, no such difference between cell types was found, but the SFA did vary in the anterior-posterior axis implying possible differences in channel expression along this axis.

4.3. Principal cells of LEC LII are Reelin-IR

In this study, 98.1% of the cells showed immunoreactivity to the protein Reelin, and none of the cells did show immunoreactivity to the calcium-binding protein CB. This included all four cell types, and the staining seemed to be identical across the cell types, with no marked differences in intensity of the stain across cell types. The distribution of the two immunomarkers displayed two general bands in superficial LEC, with Reelin residing in superficial LII and CB in the deep LII and superficial LIII (see figure 3.4.1). These distributions are in line with what has been previously reported in LEC LII/LIII (Wouterlood, 2002, Ramos-Moreno et al., 2006), and is different from the distribution seen in MEC LII. The Reelin and CB distribution in MEC LII is more dispersed within the layer, and Reelin-IR and CB-IR cells are more frequently adjacent to each other (Varga et al., 2010, Gianatti, 2015). The results presented in this study showed that the space inbetween the Reelin-IR band and the CB-IR band in LEC LII was only sparsely populated by cells (see figure 7.1 in appendix), suggesting that LEC LII should be separated into two sublayers: LIIa and LIIb. This division of LEC LII has previously been suggested (Wyss, 1981, Caballero-Bleda and Witter, 1993). Moreover, the division of the sublayer is not only based on immunoreactivity, but also that LIIa has distinctive clusters of cells whereas LIIb appears as a continuation of MEC LII (Kohler, 1986, 1988). This could in turn have something to do with the fact that MEC and LEC do not develop during the same time. LEC develops (embryonically) a few days before MEC (Bayer, 1980, Wyss et al., 1983). Since Reelin has a role in development, it is plausible that differences in LII (separation into LIIa and LIIb in LEC for instance) has something to do with this. There is also a heavier Reelin-IR in LEC LII than MEC LII (Ramos-Moreno et al., 2006), making the immunomarkers vary in both distribution as well as in quantity between the two twin regions.

One claim made from a study of MEC LII, was that only the Reelin-IR stellate cells project to the hippocampus, whereas the CB-IR pyramidal cells project extrahippocampally (Varga et al., 2010). This is not clear in LEC, as no tracing studies have been linked to the immunostaining against Reelin and CB in this area. Since there are only two major principal cell types in MEC LII, these cells can in theory be separated by only two immunomarkers. Due to the presence of four cell types in LEC LII, a simple separation by using two

immunomarkers is not feasible. Furthermore, implicating that only Reelin-IR cells contribute to the perforant path, whilst also suggesting that the immunoreactivity to CB or Reelin can separate cell types, is contradicting to what has been found in this and previous studies. There it was reported that all cell types of both LEC and MEC LII project to the hippocampus (Schwartz and Coleman, 1981, Germroth et al., 1989b). It could however still be true that only stellate cells project to the hippocampus, as shown by Varga et al (2010) and that they are the only Reelin-IR cells in MEC LII. However, it remains unclear if the Reelin-IR cells in LEC LII are the *only* cells of LEC LII that project to the hippocampus. Additionally, neither is it known whether *all* the Reelin-IR cells of LEC LII do indeed project to the hippocampus. It is still not clear where the CB-IR cells of MEC LII project to, though they have been suggested to project extrahippocampally (Varga et al., 2010). Since the CB-IR cell types have not been identified in LEC LII, it remains an open question whether or not these cells are different from the superficial Reelin cells. It is likely that CB-IR cells are pyramidal cells, since the pyramidal cells seem to be located deeper in the layer, as well as in LIII, coinciding with the CB-IR band. Also, since LIII projects to CA1 and subiculum, regions where pyramidal cells also have been shown to be the primary cell type, it could mean that perhaps CB-IR indicates that these cells synapse onto pyramidal cells. It remains unclear whether or not single LII cells have separate projections to either CA3 or DG, or if the DG-projecting cells also give off collaterals onto CA3 cells (Cappaert et al., 2014). It could be that the vast majority of LEC LIIa cells are Reelin-IR and that all of these cells project to the DG and synapse onto granule cells, whereas the LEC LII CB-IR cells synapse onto pyramidal cells of CA3.

If it holds true that stellate cells and pyramidal cells in MEC LII can be separated by immunoreactivity to Reelin and CB, then this makes the cellular population in MEC LII much more heterogeneous than the cellular population in LEC LII, both in terms of immunohistochemistry and electrophysiology. However, the story is not that simple in MEC either. Canto & Witter's 2012b study in MEC stated that there were indeed two major (stellate cells and pyramidal cells) and three intermediate cell type classes. The intermediate cell types were named oblique pyramidal neuron, between pyramidal and stellate cell, and between oblique pyramidal and stellate cell. The three classes made up 21% of the cells found in LII MEC. These cells were electrophysiologically confined to be either like stellate

cells or pyramidal cells (Canto and Witter, 2012b). Also, the immunoreactivy in MEC was not 100% separated by cell type, since not all CB-IR cells in MEC were pyramidal cells (Tang et al., 2014). This means that even in MEC, the immunoreactivity to either CB or Reelin does not automatically infer the cell type present.

Lack of IR to both Reelin and CB suggests a third subpopulation of LEC LII cells

The two cells that were not immunoreactive to Reelin, were neither immunoreactive to CB. This implies that a subpopulation of LEC LII principal cells are not Reelin-IR nor are they CB-IR. The two cells in question were situated in the Reelin-IR band, and they were one fan cell and one pyramidal cell. Figure 7.1 in the appendix suggests that there are indeed a small number of cells that do not show immunoreactivity to neither Reelin nor CB, but the majority of these cells seem to reside in between the two immunoreactive bands. The fan cell was in a cluster of four cells, and had before the colocalization of immunomarkers been scanned for reconstruction. This is hard on the tissue, and the tissue had suffered some from the handling. The Biocytin filling had bleached since the morphological scan. The three other cells were labeled for Reelin, and it might very well be that the fan cell should have been Reelin-IR as well, but that it was too weak to see. For the pyramidal cell, the original filling was poor to start with, whereas the other cell in the slice was well-preserved. Thus, it could be that there was either poor access to the pyramidal cell during filling or that a part of the cell membrane was removed along with the exiting of the pipette. However, the electrophysiological recording of this cell was included in the dataset of acceptable recordings, so the poor filling does probably not stem from the recording, but rather the cell itself.

4.4. Functional implications

This study showed that no electrophysiologically investigated parameter differed significantly between the fan cells, multiform cells, oblique pyramidal cells and pyramidal cells, suggesting that possible functional differences stem from differences in morphology and/or connectivity. The fact that morphologically, MEC LII shows vertically oriented cells

(pyramidal, stellate) whereas superficial LEC LII shows horizontally oriented cells (fan, oblique pyramidal) is interesting. It could be, that because LEC occupies approximately 68% of the total surface area of the EC (Dolorfo and Amaral, 1998), it has more processes going horizontally. This is because it has to cover twice as much area as MEC LII, with roughly the same number of cells (Witter, 2010). By covering a wider mediolateral extent of EC, LEC LII cells could also receive more topographically specialized input. By combining input in space and time, LEC LII could possibly decipher between more complex combinations of input as well. Also, with the vast majority of LEC LIIa cells being Reelin-IR, this suggests that the cells are highly adaptable, and can easily undergo synaptogenesis (Rogers et al., 2011), which allows for dynamical adjustments to changes in input. The spatiotemporal coding scheme opportunity by single cells covering a larger mediolateral extent and the adaptational level suggested by the Reelin-IR implies that the principal cells of LEC LII could form dynamical circuits that can change easily to large amount of input, making clear distinctions between inputs that are similar.

A dynamic, high resolution circuitry could be highly beneficial when separating objects in space, which LEC LII cells have been shown to do (Deshmukh and Knierim, 2011). LEC LII cells have also been shown to fire when encountering objects that were missing from where they were originally observed. These cells have been referred to as trace-cells (Tsao et al., 2013). This suggests that the circuit in which these cells lie, have stored information about previously encountered objects, and yields extra attention for when the objects are missing from where they were initially "learned" to be. This could in turn have something to do with an attractor network mechanism in LEC. In general, an attractor network is a neural network that can come into one or more stable states. For this to occur, recurrent connections must be present. It has been suggested that the way in which MEC codes spatial information is by using a continuous attractor system, as a way of coding the vectorial distance and direction the animal is moving (McNaughton et al., 2006). Since space is a continuous variable this can be supported. However, objects are discrete variables. As such, the spatial object recognition in LEC could employ a discrete attractor system. This is supported by the evidence of trace-cells. It is also supported in that CA3 has the possibility to store both discrete and continuous attractors in the same network and that "the place can be used as a retrieval cue to recall

the object at that place; and that the object can be used as a retrieval cue to recall the place of the object", thus complimenting each other in both spatial and episodic memory incidences (Rolls et al., 2002). Since no connections were found between the Reelin-IR cells, based on the protocol used for the separate connectivity study, it implies that the recurrent connectivity does not include (many) direct connections between Reelin-IR cells, but could perhaps mean that the cells of LEC LIIa are connected to cells of LEC LIIb which are CB-IR and that this would make a circuit across the sublayers. However, it still remains to be seen if the connectivity within LEC LII will allow for such a model.

4.5. Methodological issues

4.5.1. Comparing electrophysiological parameters within and across studies

It generally holds true that the physiological parameters measured in one study are not directly comparable for those measured in another study, due to subtle differences in either animals, recordings or calculations. When it comes to the recording protocol, finer intervals of current injections, longer pauses, and total recording time have an influence on what recorded data there is to do calculations on. Finally, the calculations being done have been shown to be quite different between studies, with the safer ones being that of resting membrane potential and steady-state measures, as these can be read off directly. Some programs allow for more automated calculations (like Fitmaster) whereas others give the users more freedom (such as IGOR Pro). Since each cell will vary (i.e. not fire an action potential at the same current injection, or have an action potential firing on the rebound) recordings need to be treated differently. The exact same calculations, on the exact same interval, for the exact same current injection does not seem feasible. This adds to the issue of normalizing these measures, and therefore makes it difficult to compare two measures done in two different labs, or even sometimes within one lab, as has been the case with this study and Canto & Witter 2012.

4.5.2. Statistical analyses

For the statistical analysis, the cells could have also been clustered based on their day of retrieval. This would ensure that the day-to-day variance would be taken care of, together

with potential differences between animals (there are differences in age). However, the different cell types were fairly well distributed over the separate patch-clamp recording days, so this was not opted for. Also, for the anterior-posterior position, the slices from the same day were separated over the whole extend of the axis, and this should limit the need of clustering.

For the morphological analysis, a reconstruction of all cells could have potentially been performed. However, this would have been too time consuming. It would perhaps have been best if all the cells were screened for their cell type, and the cells that were properly filled, with intact axons, could have been reconstructed. Instead, the first few cells were all reconstructed, and it was only later on that cells were elected for reconstruction based on their filling.

4.5.3. Optimizing the immunoprotocol

The fact that immunohistochemistry is so empirically based, with few underlying general ideas of how the actual binding process works, makes it difficult to reproduce. Also, working with biological tissue is predisposed to yield variations. The immunoprotocol could have been optimized further. Starting in October 2014 and going into February 2015, the protocol was tested for the different variables. Although it was not ideal in February, a sufficient amount of tests and the fact that the CB and Reelin stains did not co-localize in the superficial LII, made it possible to use the protocol and analyze the stain. Also, for some slices, there was a lot more background for the Reelin stain, which was apparent as a weak labeling in all layers and of more cells than would be expected to be just Reelin-IR. This could be directly related to the thickness of the slices used (400 µm). An option would have been to resection the slices after the confocal-scanning for morphological-purposes had been performed. This has been opted for in studies coupling electrophysiological recordings and immunohistochemistry before, and it was considered. The slices would then have been resectioned into either 50 or 60 µm thick sections, of which only the first or second slices (from the top) would have had cell bodies, as this is how deep the cells were patched. However, there is a much larger risk of losing cells this way, and it did not seem to be necessary.

The CB stain seemed to vary a lot across sections. This was both in intensity and quantity. Since the CB primary antibody used was polyclonal, some variation across subjects is expected, as the polyclonal antibody can bind to a variety of epitopes on the target antigen (Renshaw, 2007, Kumar and Rudbeck, 2009). However, it was tested up against a mouse-monoclonal primary antibody for CB as well, and the two antibodies seemed to stain the same cells in this case, but deviations from this might exist (see appendix figure 7.4). It can sometimes be beneficial to use a polyclonal antibody, and this seems to be the case for CB, as several studies staining against CB, have used the CB anti-rabbit primary antibody (Peterson et al., 1996, Varga et al., 2010). In general, the advantages of using a polyclonal rather than a monoclonal antibody is that the polyclonal antibodies have a higher affinity and are less sensitive to handling. Two drawbacks are more variation and less specificity (Kumar and Rudbeck, 2009). The CB stain did not result in much background, and the staining never seemed excessive to what had been reported in previous studies in LEC (Wouterlood, 2002).

4.5.4. Position of the cells

The cells could have been controlled for that they actually were in LEC LII and not in adjacent layers or cortices. The landmarks being used were the rhinal fissure and the islands of dense clusters of large cells appearing after a relatively cell-free LI. Since no deep cells were patched, it was rather safe to assume that it would still be LII, and not LIII. In addition, most of the cells were located dorsally, close to the fissure, and laterally, away from MEC, to assure that the cells were actually in LEC and not in MEC. It would have been possible to perform a Nissl stain on each section, so that the cytoarchitectural differences could confirm the location of the patched cells. However, the Reelin stain in LEC LII follows LEC beautifully with a distinct cut-off at the dorsal border near the fissure to either perirhinal or postrhinal cortex. For the more anterior sections, this is especially clear, as the Reelin stain stops more ventral to the rhinal fissure, as does LEC. This confinement to LEC at the dorsal border near the fissure has also been reported elsewhere (Stranahan et al., 2011a), confirming that the position of the cells in this study should indeed be restricted to LEC LII.

4.6. Future

A natural follow-up to this study would be to patch cells located deeper in LII towards the border to LIII to investigate the immunoreactivity of these cells, which cell types they are, and whether or not they differ from the more superficial cells in terms of electrophysiology. It is likely that these cells are CB-IR pyramidal cells, but they could also be GABAergic CB-IR cells, as approximately 10% of LEC CB-IR cells are supposed to be GABAergic (Wouterlood and Jasperse, 2001). Furthermore, it would be interesting to patch GABAergic cells in the superficial LII LEC, as this superficial Reelin-IR band in LII might also include some Reelin-IR GABAergic cells (Germroth et al., 1989a, Witter, 2010). By filling these cells with Biocytin, one can check to see whether their axon collaterals spread locally or if they have axons that can be followed into the angular bundle. If the latter is the case, then there is a fair chance that these GABAergic cells project to the hippocampus (Germroth et al., 1989a, Witter, 2010), and it would be interesting to further characterize them.

It is also possible to check other molecular markers such as Calretinin (CR). CR is also a calcium-binding protein that has been found to be in specific cellular populations in the EC. However, there is not that much CR in LEC LII and it is controversial whether it is just in interneurons, or also in principal neurons. Wouterlood et al (2000) showed that roughly 30% of the CR-IR neurons co-localized with GABA, and that the remaining 70% most likely were extrahippocampally projecting principal cells (Wouterlood et al., 2000). Another study done by Miettinen et al (1997) showed that nearly 100% of the CR-IR cells in LII and LIII of the EC co-expressed GAD or GABA (Miettinen et al., 1997). It would be interesting to resolve this ambiguity, and do a double-immuno for CR with CB, as they have been shown to co-localize (Leuba and Saini, 1997). Another interesting thing about CR is that it has been suggested that CR-IR cells only synapse onto interneurons. This could add knowledge to the connectivity circuitry in superficial LEC LII, and it would be very interesting to see which cell types out of the principal cells, that are CR-IR (if any).

Another possible project would be to check which cells in LEC LII are positive for the neuropeptide opioid enkephalin. It has been shown that the lateral perforant path (and not the medial) uses proenkephalin derived peptides, which may act together with glutamate in inducing LTP (Bramham et al., 1991). Generally, enkephalic immunoreactive cells are relatively few compared to the total number of cells which gives rise to the lateral perforant path (Steward and Scoville, 1976, Fredens et al., 1984). The fact that not all the cells contributing to the perforant path are encephalic gives rise to the possibility that there might be a peptidergic component of the lateral perforant path which differs from the nonpeptidergic component. It would be interesting to see which cell types this would include.

It would also be very useful to do a study where one does immunohistochemistry against CB, Reelin and Nissl, and then do a proper cell count using stereology. The sections would have to be thin (40-60µm), and careful delineations between MEC and LEC and the different layers within, should be made. This would give useful numbers on what to expect on the cellular distribution and quantity of Reelin and CB IR cells in the EC, and would hopefully clarify the differences in distributions and quantity between MEC and LEC.

Since the different morphological cell types do not differ much in their electrophysiological parameters, it is possible to conduct experiments on their dendrites or membrane channels. Morphological differences (especially size) should yield differences in how the cells integrate and respond to alterations of voltage or current perturbations. Cellular diversity should represent functional differences in how they interact, if this difference is not in electrophysiology or immunoreactivity, then it could be in connectivity. As none of the cells that were patched in this study were connected to one another, no further information about this is added.

5. Conclusions

The results of this study demonstrate that the cell types characterized morphologically display diversity within groups, in terms of dendritic extension and somatic shape. Two subclasses of the fan cells were suggested on the basis of somatic shape and dendritic distribution, namely the spherical and parachute – shaped fan cells. Furthermore, it was not possible to separate the morphologically different cells based on their electrophysiological parameters measured here, as there was no significant difference in the electrophysiological responses of the different cell groups. Lastly, the fan cells, multiform cells, oblique pyramidal cells and pyramidal cells all show a positive immunoreactivity to Reelin. Thus, the immunoreactivity to Reelin of cells in LEC LII is not cell-type specific. It is still unknown which cell types of LEC LII expresses Calbindin. Only two cells out of the 104 cells studied showed no immunoreactivity to either immunomarker. This study suggests that principal cells of LEC LII might be more homogeneous with respect to electrophysiological responses and immunoreactivity than MEC LII.

6. References

Alonso A, Llinas RR (1992). Electrophysiology of the mammillary complex in vitro. II. Medial mammillary neurons. J Neurophysiol 68:1321-1331.

Ascoli GA, Alonso-Nanclares L, Anderson SA, Barrionuevo G, Benavides-Piccione R, Burkhalter A, Buzsaki G, Cauli B, DeFelipe J, Fairen A, Feldmeyer D, Fishell G, Fregnac Y, Freund TF, Gardner D, Gardner EP, Goldberg JH, Helmstaedter M, Hestrin S, Karube F, Kisvarday ZF, Lambolez B, Lewis DA, Marin O, Markram H, Munoz A, Packer A, Petersen CCH, Rockland KS, Rossier J, Rudy B, Somogyi P, Staiger JF, Tamas G, Thomson AM, Toledo-Rodriguez M, Wang Y, West DC, Yuste R, PING (2008). Petilla terminology: nomenclature of features of GABAergic interneurons of the cerebral cortex. Nat Rev Neurosci 9:557-568.

Ascoli GA, Samsonovich A (2002). Bayesian morphometry of hippocampal cells suggests same-cell somatodendritic repulsion. Adv Neur In 14:133-139.

Aston-Jones GS, Siggins GR (2000). Electrophysiology. vol. 2014.

Barres BA, Silverstein BE, Corey DP, Chun LL (1988). Immunological, morphological, and electrophysiological variation among retinal ganglion cells purified by panning. Neuron 1:791-803.

Bayer SA (1980). Development of the Hippocampal Region in the Rat .2. Morphogenesis during Embryonic and Early Postnatal Life. J Comp Neurol 190:115-134.

Bear MF, Connors BW, Paradiso MA (2007). The Action Potential. In: Neuroscience - Exploring the Brain, pp 75-100.

Benda J, Longtin A, Maler L (2005). Spike-frequency adaptation separates transient communication signals from background oscillations. J Neurosci 25:2312-2321.

Berndtsson C (2013). The Specificity of Output from Medial Entorhinal Cortex. In: Neuroscience Master's Trondheim, Norway: NTNU.

Blair HT (2014). Neuroscience. Charting the islands of memory. Science 343:846-847.

Braak H, Braak E (1985). On Areas of Transition between Entorhinal Allocortex and Temporal Isocortex in the Human-Brain - Normal Morphology and Lamina-Specific Pathology in Alzheimers-Disease. Acta Neuropathol 68:325-332.

Bramham CR, Milgram NW, Srebro B (1991). Activation of AP5-sensitive NMDA Receptors is Not Required to Induce LTP of Synaptic Transmission in the Lateral Perforant Path. Eur J Neurosci 3:1300-1308.

Brette R, Destexhe A (2012). Intracellular Recording. In: Handbook of Neural Activity Measurement, pp 44-91: Cambridge University Press.

Burwell RD (2000). The parahippocampal region: corticocortical connectivity. Ann NY Acad Sci 911:25-42.

Burwell RD, Amaral DG (1998a). Cortical afferents of the perirhinal, postrhinal, and entorhinal cortices of the rat. J Comp Neurol 398:179-205.

Burwell RD, Amaral DG (1998b). Perirhinal and postrhinal cortices of the rat: interconnectivity and connections with the entorhinal cortex. J Comp Neurol 391:293-321.

Caballero-Bleda M, Witter MP (1993). Regional and laminar organization of projections from the presubiculum and parasubiculum to the entorhinal cortex: an anterograde tracing study in the rat. J Comp Neurol 328:115-129.

Canto CB (2011). Layer Specific Integrative Properties of Entorhinal Principal Neurons vol. Ph.D. Trondheim, Norway: NTNU.

Canto CB, Witter MP (2012a). Cellular properties of principal neurons in the rat entorhinal cortex. I. The lateral entorhinal cortex. Hippocampus 22:1256-1276.

Canto CB, Witter MP (2012b). Cellular properties of principal neurons in the rat entorhinal cortex. II. The medial entorhinal cortex. Hippocampus 22:1277-1299.

Canto CB, Wouterlood FG, Witter MP (2008). What does the anatomical organization of the entorhinal cortex tell us? Neural Plast 2008:381243.
Cappaert NLM, Van Strien NM, Witter MP (2014). Hippocampal Formation. In: The Rat Nervous System, pp 511-573: Elsevier Inc. .
Chin J, Massaro CM, Palop JJ, Thwin MT, Yu GQ, Bien-Ly N, Bender A, Mucke L (2007). Reelin depletion in the entorhinal cortex of human amyloid precursor protein transgenic mice and humans with Alzheimer's disease. J Neurosci 27:2727-2733.
de Rouvroit CL, de Bergeyck V, Cortvrindt C, Bar I, Eeckhout Y, Goffinet AM (1999). Reelin, the extracellular matrix protein deficient in reeler mutant mice, is processed by a metalloproteinase. Exp Neurol 156:214-217.
De Villers-Sidani E, Tahvildari B, Alonso A (2004). Synaptic activation patterns of the perirhinal-entorhinal inter-connections. Neuroscience 129:255-265.
Deshmukh SS (2014). Spatial and Nonspatial Representations in the Lateral Entorhinal Cortex. In: Space, Time and Memory in the Hippocampal Formation (Derdikman, D. and Knierim, J. J., eds), pp 127-152 Baltimore, USA: Springer.
Deshmukh SS, Knierim JJ (2011). Representation of non-spatial and spatial information in the lateral entorhinal cortex. Front Behav Neurosci 5.
Didic M, Barbeau EJ, Felician O, Tramoni E, Guedj E, Poncet M, Ceccaldi M (2011). Which memory system is impaired first in Alzheimer's disease? J Alzheimers Dis 27:11-22.
Dolorfo CL, Amaral DG (1998). Entorhinal cortex of the rat: topographic organization of the cells of origin of the perforant path projection to the dentate gyrus. J Comp Neurol 398:25-48.
Eichenbaum H, Fortin NJ (2005). Bridging the gap between brain and behavior: Cognitive and neural mechanisms of episodic memory. J Exp Anal Behav 84:619-629.
Empson RM, Gloveli T, Schmitz D, Heinemann U (1995). Electrophysiology and Morphology of a New-Type of Cell within Layer-Ii of the Rat Lateral Entorhinal Cortex in-Vitro (Vol 193, Pg 149, 1995). Neurosci Lett 199:81-81.
Evers JF, Schmitt S, Sibila M, Duch C (2005). Progress in functional neuroanatomy: Precise automatic geometric reconstruction of neuronal morphology from confocal image stacks. J Neurophysiol 93:2331-2342.
Fredens K, Stengaard-Pedersen K, Larsson LI (1984). Localization of enkephalin and cholecystokinin immunoreactivities in the perforant path terminal fields of the rat hippocampal formation. Brain Res 304:255-263.
Fujimaru Y, Kosaka T (1996). The distribution of two calcium binding proteins, calbindin D-28K and parvalbumin, in the entorhinal cortex of the adult mouse. Neurosci Res 24:329-343.
Germroth P, Schwerdtfeger WK, Buhl EH (1989a). GABAergic neurons in the entorhinal cortex project to the hippocampus. Brain Res 494:187-192.
Germroth P, Schwerdtfeger WK, Buhl EH (1989b). Morphology of Identified Entorhinal Neurons Projecting to the Hippocampus - a Light Microscopical Study Combining Retrograde Tracing and Intracellular Injection. Neuroscience 30:683-691.
Gianatti M (2015). Projections of calbindin expressing neurons in layer II of the entorhinal cortex. In: Neuroscience Master's Trondheim, Norway: NTNU.
Giocomo LM, Hasselmo ME (2008). Time constants of h current in layer ii stellate cells differ along the dorsal to ventral axis of medial entorhinal cortex. J Neurosci 28:9414-9425.
Hafting T, Fyhn M, Molden S, Moser MB, Moser EI (2005). Microstructure of a spatial map in the entorhinal cortex. Nature 436:801-806.
Halavi M, Hamilton KA, Parekh R, Ascoli GA (2012). Digital reconstructions of neuronal morphology: three decades of research trends. Fronti Neurosci 6:49.
Hamam BN, Amaral DG, Alonso AA (2002). Morphological and electrophysiological characteristics of layer V neurons of the rat lateral entorhinal cortex. J Comp Neurol 451:45-61.
Hamam BN, Kennedy TE, Alonso A, Amaral DG (2000). Morphological and electrophysiological characteristics of layer V neurons of the rat medial entorhinal cortex. J Comp Neurol 418:457-472.

Hargreaves EL, Rao G, Lee I, Knierim JJ (2005). Major dissociation between medial and lateral entorhinal input to dorsal hippocampus. Science 308:1792-1794.
Hille B (2001). Introduction. In: Ion Channels of Excitable Membranes, pp 1-21: Sinauer Associates, Inc.
Iacopino AM, Christakos S (1990). Specific reduction of calcium-binding protein (28-kilodalton calbindin-D) gene expression in aging and neurodegenerative diseases. Proc Natl Acad Sci U S A 87:4078-4082.
Inoue S (2006). Foundations of Confocal Scanned Imaging in Light Microscopy. In: Handbook of Biological Confocal Microscopy (Pawley, J. B., ed), pp 1-16 New York, USA: Springer.
Insausti R, Herrero MT, Witter MP (1997). Entorhinal cortex of the rat: Cytoarchitectonic subdivisions and the origin and distribution of cortical efferents. Hippocampus 7:146-183.
Iritani S, Niizato K, Emson PC (2001). Relationship of calbindin D28K-immunoreactive cells and neuropathological changes in the hippocampal formation of Alzheimer's disease. Neuropathology 21:162-167.
Jones RSG (1994). Synaptic and Intrinsic-Properties of Neurons of Origin of the Perforant Path in Layer-Ii of the Rat Entorhinal Cortex in-Vitro. Hippocampus 4:335-353.
Kandel ER, Barres BA, Hudspeth AJ (2013). Nerve Cells, Neural Circuitry, and Behavior. In: Principals of Neural Science (Kandel, E. R. et al., eds), pp 21-38 USA: McGraw-Hill Companies.
Kitamura T, Pignatelli M, Suh J, Kohara K, Yoshiki A, Abe K, Tonegawa S (2014). Island cells control temporal association memory. Science 343:896-901.
Klink R, Alonso A (1997). Morphological characteristics of layer II projection neurons in the rat medial entorhinal cortex. Hippocampus 7:571-583.
Kohler C (1986). Intrinsic connections of the retrohippocampal region in the rat brain. II. The medial entorhinal area. J Comp Neurol 246:149-169.
Kohler C (1988). Intrinsic connections of the retrohippocampal region in the rat brain: III. The lateral entorhinal area. J Comp Neurol 271:208-228.
Konig P, Engel AK, Singer W (1996). Integrator or coincidence detector? The role of the cortical neuron revisited. Trends Neurosci 19:130-137.
Kovacs T, Cairns NJ, Lantos PL (2001). Olfactory centres in Alzheimer's disease: olfactory bulb is involved in early Braak's stages. Neuroreport 12:285-288.
Kruskal WH, Wallis WA (1952). Use of Ranks in One-Criterion Variance Analysis. J Am Stat Assoc 47:583-621.
Kumar GL, Rudbeck L (2009). Immunohistochemical (IHC) Staining Methods: Dako.
Leuba G, Saini K (1997). Colocalization of parvalbumin, calretinin and calbindin D-28k in human cortical and subcortical visual structures. J Chem Neuroanat 13:41-52.
Li WC, Soffe SR, Roberts A (2004). A direct comparison of whole cell patch and sharp electrodes by simultaneous recording from single spinal neurons in frog tadpoles. J Neurophysiol 92:380-386.
Lingenhohl K, Finch DM (1991). Morphological Characterization of Rat Entorhinal Neurons Invivo - Soma-Dendritic Structure and Axonal Domains. Exp Brain Res 84:57-74.
Markram H, Toledo-Rodriguez M, Wang Y, Gupta A, Silberberg G, Wu C (2004). Interneurons of the neocortical inhibitory system. Nat Rev Neurosci 5:793-807.
McNaughton BL, Battaglia FP, Jensen O, Moser EI, Moser MB (2006). Path integration and the neural basis of the 'cognitive map'. Nat Rev Neurosci 7:663-678.
Miettinen M, Pitkanen A, Miettinen R (1997). Distribution of calretinin-immunoreactivity in the rat entorhinal cortex: coexistence with GABA. J Comp Neurol 378:363-378.
Molleman A (2003). Basic Theoretical Principles. In: Patch Clamping: An Introductory Guide to Patch Clamp Electrophysiology England: John Wiley & Sons.
O'Keefe J, Dostrovsky J (1971). The hippocampus as a spatial map. Preliminary evidence from unit activity in the freely-moving rat. Brain Res 34:171-175.
Pape HC (1996). Queer current and pacemaker: the hyperpolarization-activated cation current in neurons. Annu Rev Physiol 58:299-327.

Peters A, Kara DA (1985). The Neuronal Composition of Area-17 of Rat Visual-Cortex .1. The Pyramidal Cells. J Comp Neurol 234:218-241.
Peterson DA, LucidiPhillipi CA, Murphy DP, Ray J, Gage FH (1996). Fibroblast growth factor-2 protects entorhinal layer II glutamatergic neurons from axotomy-induced death. J Neurosci 16:886-898.
Purves D, Augustine G, Fitzpatrick D (2001). The Asscoation Cortices: An overview of cortical structure. In: Neuroscience Sunderland (MA): Sinauer Associates.
Ramos-Moreno T, Galazo MJ, Porrero C, Martinez-Cerdeno V, Clasca F (2006). Extracellular matrix molecules and synaptic plasticity: immunomapping of intracellular and secreted Reelin in the adult rat brain. Eur J Neurosci 23:401-422.
Ray S, Naumann R, Burgalossi A, Tang QS, Schmidt H, Brecht M (2014). Grid-Layout and Theta-Modulation of Layer 2 Pyramidal Neurons in Medial Entorhinal Cortex. Science 343:891-896.
Renshaw S (2007). Immunohistochemistry. Cambridge, UK: Scion Publishing Ltd.
Rogers JT, Rusiana I, Trotter J, Zhao L, Donaldson E, Pak DT, Babus LW, Peters M, Banko JL, Chavis P, Rebeck GW, Hoe HS, Weeber EJ (2011). Reelin supplementation enhances cognitive ability, synaptic plasticity, and dendritic spine density. Learn Mem 18:558-564.
Rolls ET, Stringer SM, Trappenberg TP (2002). A unified model of spatial and episodic memory. Proc R Soc A 269:1087-1093.
Room P, Groenewegen HJ (1986). Connections of the Parahippocampal Cortex in the Cat .2. Subcortical Afferents. J Comp Neurol 251:451-473.
Schmitt S, Evers JF, Duch C, Scholz M, Obermayer K (2004). New methods for the computer-assisted 3-D reconstruction of neurons from confocal image stacks. NeuroImage 23:1283-1298.
Schwartz SP, Coleman PD (1981). Neurons of Origin of the Perforant Path. Exp Neurol 74:305-312.
Schwerdtfeger WK, Buhl EH, Germroth P (1990). Disynaptic olfactory input to the hippocampus mediated by stellate cells in the entorhinal cortex. J Comp Neurol 292:163-177.
Scoville WB, Milner B (1957). Loss of recent memory after bilateral hippocampal lesions. J Neurol Neurosurg Psychiatry 20:11-21.
Shelbourne P, Coote E, Dadak S, Cobb SR (2007). Normal electrical properties of hippocampal neurons modelling early Huntington disease pathogenesis. Brain Res 1139:226-234.
Solstad T, Boccara CN, Kropff E, Moser MB, Moser EI (2008). Representation of Geometric Borders in the Entorhinal Cortex. Science 322:1865-1868.
Solstad T, Moser EI, Einevoll GT (2006). From grid cells to place cells: a mathematical model. Hippocampus 16:1026-1031.
Spargo E, Everall IP, Lantos PL (1993). Neuronal Loss in the Hippocampus in Huntingtons-Disease - a Comparison with Hiv-Infection. J Neurol Neurosur Ps 56:487-491.
Spruston N (2008). Pyramidal neurons: dendritic structure and synaptic integration. Nat Rev Neurosci 9:206-221.
Squire LR, Stark CE, Clark RE (2004). The medial temporal lobe. Annu Rev Neurosci 27:279-306.
Steward O, Scoville SA (1976). Cells of Origin of Entorhinal Cortical Afferents to Hippocampus and Fascia Dentata of Rat. J Comp Neurol 169:347-370.
Stranahan AM, Haberman RP, Gallagher M (2011a). Cognitive decline is associated with reduced reelin expression in the entorhinal cortex of aged rats. Cereb Cortex 21:392-400.
Stranahan AM, Salas-Vega S, Jiam NT, Gallagher M (2011b). Interference with reelin signaling in the lateral entorhinal cortex impairs spatial memory. Neurobiol Learn Mem 96:150-155.
Suzuki WA, Amaral DG (1994). Perirhinal and parahippocampal cortices of the macaque monkey: cortical afferents. J Comp Neurol 350:497-533.
Suzuki WA, Eichenbaum H (2000). The neurophysiology of memory. Ann NY Acda Sci 911:175-191.
SWANT (2011). Review on Swant #CB38 Polyclonal Rabbit anti-CALB1 antibody. vol. 2015.
Available at http://1degreebio.org/reagents/product/504930/reviews/?qid=0 [Accessed March 21, 2015].

Tahvildari B, Alonso A (2005). Morphological and electrophysiological properties of lateral entorhinal cortex layers II and III principal neurons. J Comp Neurol 491:123-140.
Tang Q, Burgalossi A, Ebbesen CL, Ray S, Naumann R, Schmidt H, Spicher D, Brecht M (2014). Pyramidal and stellate cell specificity of grid and border representations in layer 2 of medial entorhinal cortex. Neuron 84:1191-1197.
Thorns V, Licastro F, Masliah E (2001). Locally reduced levels of acidic FGF lead to decreased expression of 28-kda calbindin and contribute to the selective vulnerability of the neurons in the entorhinal cortex in Alzheimer's disease. Neuropathology 21:203-211.
Tsao A, Moser MB, Moser EI (2013). Traces of Experience in the Lateral Entorhinal Cortex. Curr Biol 23:399-405.
van Strien NM, Cappaert NLM, Witter MP (2009). The anatomy of memory: an interactive overview of the parahippocampal-hippocampal network. Nat Rev Neurosci 10:272-282.
Varga C, Lee SY, Soltesz I (2010). Target-selective GABAergic control of entorhinal cortex output. Nature Neurosci 13:822-824.
Vogt BA, Miller MW (1983). Cortical Connections between Rat Cingulate Cortex and Visual, Motor, and Postsubicular Cortices. J Comp Neurol 216:192-210.
Wang X, Lambert NA (2003). Membrane properties of identified lateral and medial perforant pathway projection neurons. Neuroscience 117:485-492.
Wilson RS, Arnold SE, Schneider JA, Tang Y, Bennett DA (2007). The relationship between cerebral Alzheimer's disease pathology and odour identification in old age. J Neurol Neurosurg Psychiatry 78:30-35.
Witter MP (2010). Connectivity of the Hippocampus. In: Hippocampal Microcircuits (Cutsuridis, V. et al., eds), pp 5-26: Springer.
Witter MP, Room P, Groenewegen HJ, Lohman AHM (1986). Connections of the Parahippocampal Cortex in the Cat .5. Intrinsic Connections - Comments on Input Output Connections with the Hippocampus. J Comp Neurol 252:78-94.
Wouterlood FG (2002). Spotlight on the neurones (I): cell types, local connectivity, microcircuits, and distribution of markers. In: The Parahippocampal Region - organization and role in cognitive function, pp 61-88.
Wouterlood FG, Jasperse B (2001). Co-expression of calbindin D28k and GABA in the entorhinal cortex of the rat. Abstr Soc Neurosci 27:1827.
Wouterlood FG, Nederlof J (1983). Terminations of Olfactory Afferents on Layer-Ii and Layer-Iii Neurons in the Entorhinal Area - Degeneration Golgi Electron-Microscopic Study in the Rat. Neurosci Lett 36:105-110.
Wouterlood FG, van Denderen JC, van Haeften T, Witter MP (2000). Calretinin in the entorhinal cortex of the rat: distribution, morphology, ultrastructure of neurons, and co-localization with gamma-aminobutyric acid and parvalbumin. J Comp Neurol 425:177-192.
Wyss JM (1981). An autoradiographic study of the efferent connections of the entorhinal cortex in the rat. J Comp Neurol 199:495-512.
Wyss JM, Sripanidkulchai B, Hickey TL (1983). An Analysis of the Time of Origin of Neurons in the Entorhinal and Subicular Cortices of the Cat. J Comp Neurol 221:341-357.
Yang CR, Seamans JK, Gorelova N (1996). Electrophysiological and morphological properties of layers V-VI principal pyramidal cells in rat prefrontal cortex in vitro. J Neurosci 16:1904-1921.
Zhang SJ, Ye J, Miao C, Tsao A, Cerniauskas I, Ledergerber D, Moser MB, Moser EI (2013). Optogenetic dissection of entorhinal-hippocampal functional connectivity. Science 340:1232627.

7. Appendices

7.1. Immunohistochemistry protocol

Biocytin, Reelin and Calbindin

Original protocol given in red.

Day 1

- Heat the sections in PB at 60°C for 2 hours
- Rinse sections 2x15min in PB on shaker
- Rinse sections 5x15min in TBS-Tx on shaker
- Incubate for 3 hours with 10% goat serum in TBS-Tx on shaker
- Incubate with primary antibodies,
    - Rabbit anti-calbindin 1:3000 (1:5000)
    - Mouse anti-reelin 1:1000

  in TBS-Tx
- Leave this for 3 (4) days in refrigerator (4°C) on shaker

Day 2

- Rinse 5x15min in TBS-Tx on shaker
- Incubate with secondary antibodies,
    - Streptavidin 488, 1:600
    - Goat anti-mouse 546, 1:400
    - Goat anti-rabbit 635, 1:400
- Leave on shaker overnight in room temperature

Day 3

- Rinse section 3x15min in TBS-Tx on shaker

For confocal preparations:

- Dehydrate sections in 30%, 50%, 70%, 90% and 100%x2 alcohol, and lastly 100% alcohol and methyl salicylate (1: 1). 10 min for each step

- Clearing with methyl salicylate: leave until the section becomes transparent and sinks to the bottom of the glass tube
- Embed with methyl salicylate and metal slides

7.2. Solutions and concentrations

Phosphate buffer (PB), 0.125M (100mL):

- 31.25mL 0.4M phosphate buffer
- 68.75mL distilled H_2O

Can be stored for up to one week in refrigerator.

0.5% TBS-Tx buffer (500mL):

- 500mL distilled H_2O
- 3.03g Tris
- 4.48g NaCl
- 2.5mL Triton-X-100

Use HCl to adjust pH to 8.0.

Can be stored for up to one week in refrigerator.

Dimethyl sulfoxide (DMSO) cryoprotectant solution (100mL):

- 31.25mL 0.4M phosphate buffer
- 46.75mL H_2O
- 20mL glycerine
- 2mL DMSO

Can be stored for up to one year in a refrigerator.

Paraformalaldehyde (PFA) fixative solution (500mL):

- Heat 200 mL distilled H_2O to 60^oC in the microwave.
- Add 20g paraformalaldehyde
- Add a few drops of NaOH and heat (≤60°C) until the solution becomes clear
- Add 156 mL 0.4M phosphate buffer solution and 144 mL distilled H_2O
- Adjust pH till 7.4 using HCl
- Filter the solution

Cannot be stored unless frozen.

Ringer solution (500mL):

- 4.25g NaCl
- 0.125g KCl
- 0.1g $NaHCO_3$

Filtrate and heat up to 40^oC directly before use. pH is adjusted to 6.9 with O_2. Cannot be stored.

Articificial Cerebrospinal Fluid (ACSF) solution for cutting (1L)

- 15.359g Choline Cl
- 0.186g KCl
- 1.423g $MgCL_2*6H_20$
- 0.074g $CaCl_2$
- 4.502g Glucose
- 0.1948g NaH_2PO_4
- 2.1g $NaHCO_3$
- 2.278265g Na-ascorbate
- 0.33012g Na-pyruvate
- 18.22g D-Mannitol

Articificial Cerebrospinal Fluid (ACSF) solution for recording and holding (1L)

- 7.363g NaCl
- 0.224g KCl
- 0.187g NaH_2PO_4
- 1.801g Glucose
- 2.184g $NaHCO_3$

For recording ACSF:

250 mL of solution above, with 0.750 mL MgCl and 0.125 mL $CaCl_2$.

For holding ACSF:

750 mL of solution above, with 1.125 mL MgCL and 1.2 mL $CaCl_2$.

Intacellular (electrode) solution (100mL)

- 2.8116g K-gluconate
- 0.07456g KCl
- 0.2551g Na_2Phosphocreatin
- 0.2383g Hepes
- 0.20288g MgATP
- 0.015696g NaGTP

Adjust pH to 7.3 using KOH 285mOsm. Biocytin can be added before or after at 2-4mg/mL. Osmolality between 275-280.

7.3. Nissl

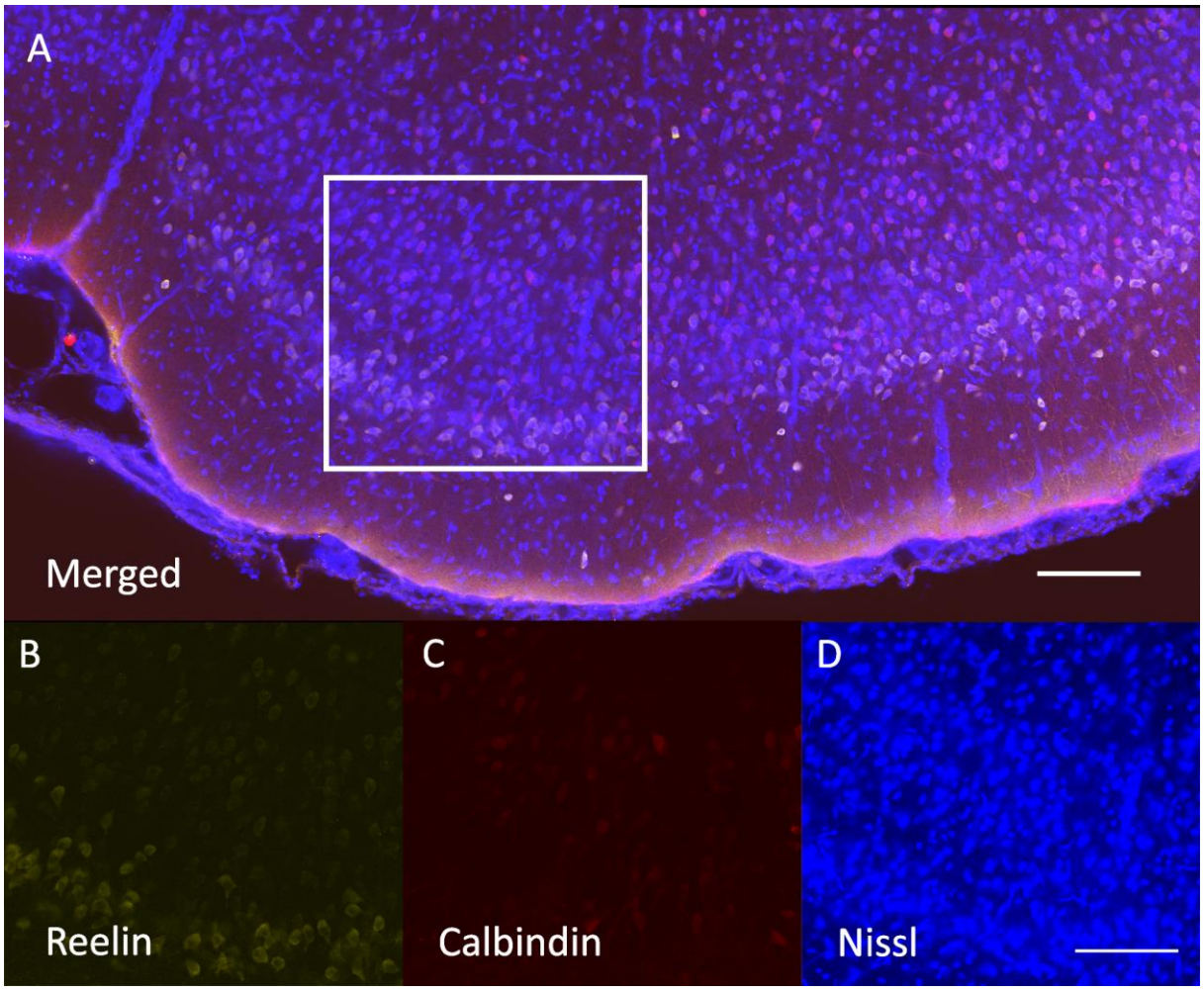

Figure 7.1. A: shows the merged image of the Nissl, Reelin and CB stain. **B, C**, and **D** show the individual scans of each stain separately from the marked square in **A**. There are more stained cells in the Nissl than the Reelin and CB stain combined. Scale bars = 100 µm.

7.4. Immunotests and controls

A total of nine tests were performed to optimalize the immunoprotocl as best possible. Initially, the CB stain was not working optimally, in that very few cells were stained, probably due to a combination concentration and incubation time of the primary antibody. A summary of the tests are given in table 7.1. Generally, there is an inverse relationship between the two, meaning that if you lower the incubation period, the concentration is opted, and it is generally wiser to start with the incubation period (Kumar and Rudbeck, 2009). After having tested both 1,2,3,4,5 days incubation time for the primary antibody, and testing for 1:5000 and 1:3000 in concentration for the primary antibody, it was decided that it was sufficient with 3 days incubation time for the primary antibody at a concentration of 1:3000 (figure 7.2.). Reelin seemed also to benefit from the 3 days incubation period with the primary antibody, but here the concentration of 1:1000 was kept. Whether the antibodies required heat-induced epitope retrieval was also tested, showing that the heating did not result in a better staining for CB nor Reelin.

A control for the secondary antibodies was carried out. The results showed no secondary antibody binding in the absence of the primary antibody (figure 7.3.). The secondaries are the goat anti-rabbit Alexa 635 for the CB stain and the goat anti-mouse Alexa 546 for the Reelin stain. A test for specificity of the CB stain was done using both the rabbit anti-CB and the mouse anti-CB. This test was carried out to see if the two antibodies raised against different epitopes of the antigen gave the same staining pattern. Since the mouse anti-CB is a monoclonal antibody, it was assumed that this would stain the same cells, or fewer cells than the rabbit anti-CB, which is a polyclonal antibody. However, they stained the same cells, as shown in figure 7.4.

Table 7.1. Table of tested variables and their conclusions for what was used in the final protocol.

Variable	**Tested**	**Used in final protocol**
Heat-induced epitope-retrieval	2hrs in 60^{o}C PB, no heat	No heat
Primary antibody incubation time (d)	1,2,3,4,5 both CB and Reelin	3
Primary antibody concentration	1:2000, 1:3000, 1:5000 CB	1:3000
Primary antibody type (host/clonality)	Rabbit-Polyclonal (CB), Mouse-Monoclonal (CB)	Rabbit-Polyclonal (CB)

The control tests (just secondary antibody or Nissl stain) are not included in the table above, and the tests were run in using different combinations in a total of 9 sessions. Test results and control images are given in the appendix 7.4.

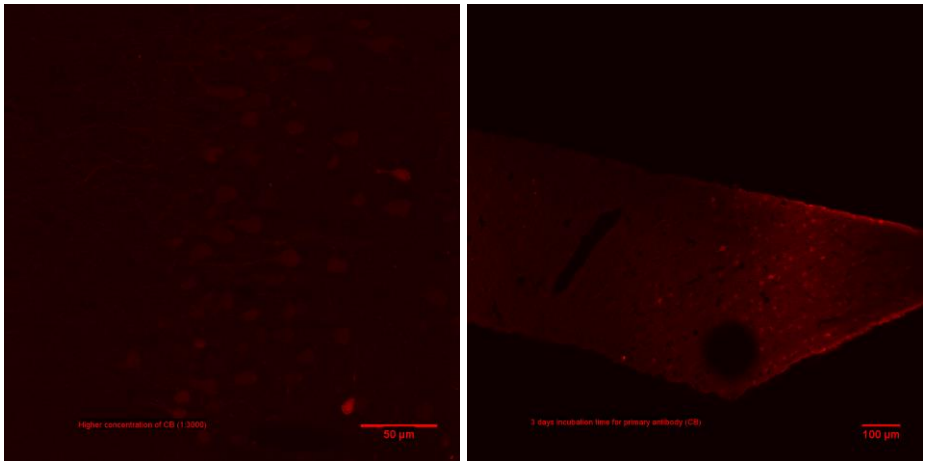

Figure 7.2. Two test runs for the 1:3000 concentration of primary antibody for CB (left) and one for the three days incubation period of the primary antibody for CB (right). Scale bars = 50 µm (left) and 100 µm (right).

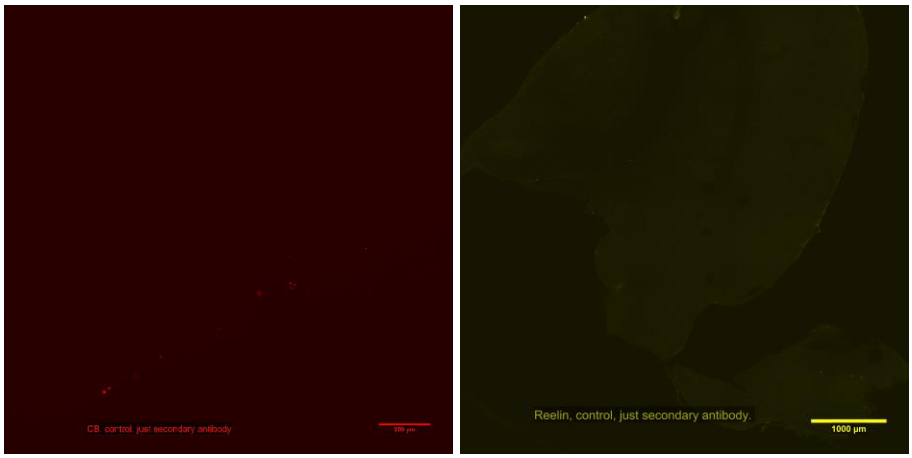

Figure 7.3. Secondary antibody control images of CB and Reelin. Scale bars = 200 µm for CB image, 1000 µm for Reelin image. No cells showed staining against just the secondary antibodies.

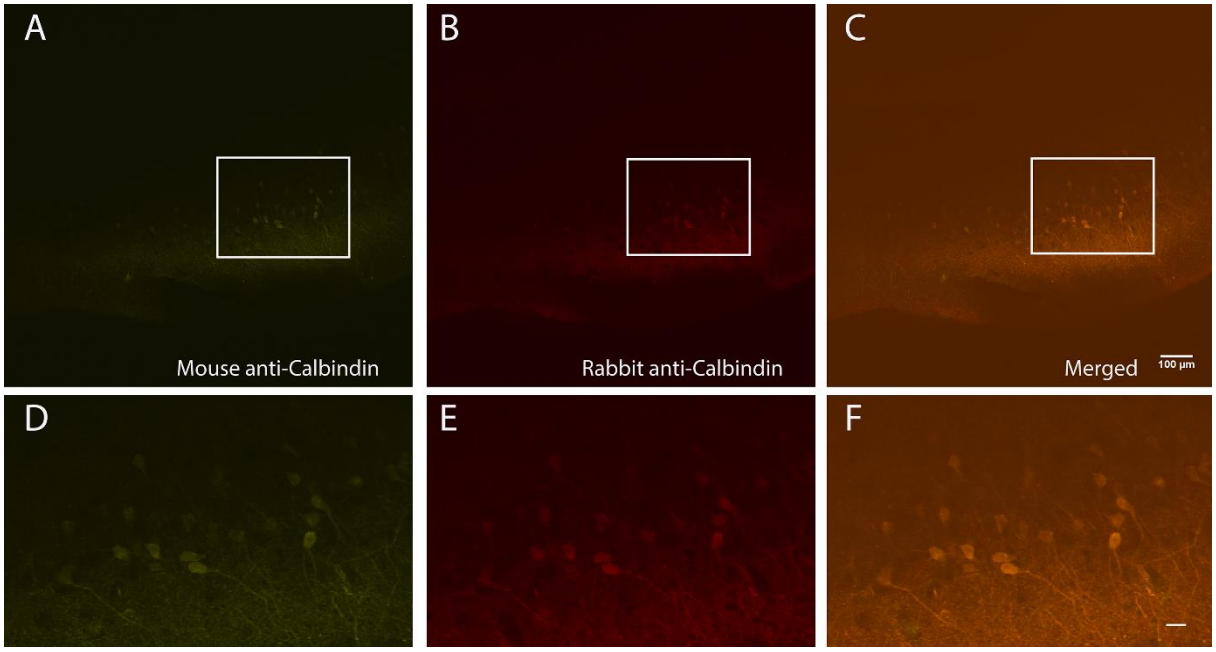

Figure 7.4. A: mouse anti-Calbindin with close-up **D**. **B**: rabbit anti-Calbindin with close-up **E**. **C:** merged image of the two showing full overlap of cells in **F**. Scale bars: **A, B, C** = 100 µm, **D, E, F** = 50 µm.

7.5. Chemicals

Antibodies	*Manufacturer*
Primary	
Mouse anti-Reelin	Merck Millipore
Rabbit anti-Calbindin	SWANT, Inc
Secondary	
Goat anti-mouse 546	Invitrogen
Goat anti-rabbit 635	Thermo Fisher (life)
Streptavidin A488	Life technologies
Serums	
Goat serum	Abcam
Other	
NeuroTrace 640/660 Nissl	Thermo Fisher (life)
Neurotrace 435/455 Nissl	Thermo Fisher (life)

Chemicals	Manufacturer
Biocytin	Sigma Aldrich
$CaCl_2$	VWR
Choline-Cl	Sigma Aldrich
D-mannitol	Sigma Aldrich
Dimethyl sulfoxide (DMSO)	VWR
Ethanol	Kemetyl Norge A/S
Glucose	VWR
Glycerine	VWR
HCl	Merck
HEPES	Sigma Aldrich
Isofluorane	Isoba vet (Intervet International)
K-glutanate	VWR
KCl	Merck
Methyl salicylate	VWR
MgATP	Sigma Aldrich
$MgCl_2$	Merck
Na-ascorbate	Sigma Aldrich
Na-GTP	Sigma Aldrich
Na-pyruvate	Sigma Aldrich
NaCl	VWR
$NaHCO_3$	Merck
NaH_2PO_4	Merck
Na_2Phosphocreatin	Sigma Aldrich
Paraformaldelhyde (PFA)	Merck
Phosphate buffer (PB)	Merck
Tris (hydroxmethyl) aminomethane	Merck
Triton-X-100	Merck

7.6. Animals

Table 7.1. Rat ID, date of patching age and sex of the 12 animals used.

Rat ID	Date of patching (YYMMDD)	Age	Sex
20279	141001	P51	Female
20282	141002	P52	Female
20440	141112	P27	Female
20437	141113	P28	Male
20501	141127	P22	Male
20503	141203	P28	Male
20504	141204	P29	Male
20505	141211	P36	Male
20603	150108	P39	Female
20744	150211	P31	Male
20745	150212	P32	Male
20672	150220	P48	Male

7.7. Electrophysiological parameters, cells sorted by cell type

7.7.1. Fan cells

Cell #	Tau	Sag	RMP	AP thresh	Input R	ISI ratio	Rebound
141112_1(2)	16,63	0,875	-67,03	-49,90	60,99	0,589	5,02
141112_1(3)	17,85	0,908	-70,46	-53,30	74,41	0,395	6,87
141112_2(1)	23,20	0,913	-70,87	-45,45	99,84	0,657	4,22
141112_2(4)	36,18	0,939	-73,43	-45,89	127,45	0,494	4,00
141112_3(1)	27,68	0,922	-69,69	-48,16	164,31	0,623	3,42
141112_3(2)	32,30	0,901	-61,66	-44,57	135,03	0,603	2,52
141112_4(2)	20,80	0,957	-71,92	-46,99	81,01	0,711	1,93
141113_2(1)	15,33	0,891	-66,39	-46,75	82,39	0,463	6,50
141113_4(1)	41,53	0,925	-71,14	-44,18	146,79	0,716	5,17
141113_4(2)	43,75	0,915	-65,85	-44,56	156,18	0,671	3,92
141127_1(2)	32,40	0,927	-70,32	-50,88	131,91	0,595	3,55
141127_1(3)	24,15	0,905	-66,57	-48,93	99,19	0,446	3,33
141127_1(4)	34,48	0,939	-70,62	-47,22	141,24	0,524	5,36
141127_2(3)	23,55	0,926	-67,92	-47,98	153,56	0,381	4,91
141127_3(1)	29,83	0,938	-73,59	-45,47	148,23	0,591	3,33
141203_1(3)	15,63	0,885	-63,57	-47,85	85,00	0,338	---
141203_3(2)	29,80	0,911	-69,74	-45,40	156,42	0,537	3,94
141203_4(1)	37,80	0,921	-67,79	-47,20	106,08	0,386	3,64
141203_4(3)	42,10	0,924	-72,21	-51,19	132,88	0,331	3,80
141204_4(2)	27,18	0,954	-70,40	-45,77	111,72	0,633	1,95
141204_4(3)	39,88	0,942	-70,27	-46,61	146,48	0,563	2,75
141211_1(2)	23,33	0,969	-74,83	-51,10	118,91	0,452	2,17
141211_2(3)	17,73	0,933	-73,56	-49,71	207,95	0,265	3,87
141211_2(4)	35,53	0,929	-77,59	-54,84	155,42	0,311	2,50
141211_3(1)	28,83	0,947	-72,42	-44,39	100,83	0,500	2,85
141127_4(1)	35,08	0,922	-73,17	-47,81	167,74	0,486	5,36
150108_1(2)	23,78	0,967	-75,78	-47,74	113,27	0,394	2,44
150108_1(3)	25,73	0,946	-74,05	-50,11	139,88	0,377	2,54
150108_2(2)	19,35	0,961	-75,62	-45,23	95,78	0,436	3,21
150108_2(3)	24,15	0,961	-78,06	-45,52	109,94	0,512	2,00
150108_3(1)	27,48	0,945	-75,80	-43,99	123,60	0,532	2,56
150108_3(3)	26,65	0,953	-82,64	-49,02	118,33	0,553	2,30
150108_3(4)	25,88	0,938	-69,92	-43,08	134,36	0,519	3,28
150108_4(1)	24,60	0,966	-76,91	-49,74	106,43	0,241	2,25
150108_4(3)	24,13	0,947	-74,21	-44,40	129,33	0,347	2,60
150212_1	27,83	0,952	-72,49	-50,20	141,75	0,219	2,64
150212_2(2)	25,48	0,962	-77,42	-50,27	115,95	0,249	1,77
150212_3	26,70	0,950	-70,10	-50,60	152,07	0,235	2,28
150220_2(2)	17,03	0,975	-67,33	-49,76	69,16	0,588	2,40
150220_2(3)	13,43	0,961	-69,03	-48,19	61,80	0,690	2,92

150220_3(1)	30,83	0,940	-70,52	-48,17	117,92	0,670	2,94
141001_3	28,66	0,948	-72,06	-45,33	111,41	0,586	3,53
141002_1	20,87	0,955	-74,45	-46,17	104,33	0,530	4,91
141002_3(2)	27,97	0,925	-66,17	-43,21	141,99	0,503	4,95
141002_3(4)	29,60	0,955	-71,32	-45,20	102,91	0,604	2,73
141002_4(1)	23,15	0,923	-66,10	-44,76	147,27	0,573	4,23
141002_4(2)	38,99	0,925	-65,67	-41,52	111,47	0,630	4,27
141002_4(4)	31,38	0,923	-66,84	-44,32	115,33	0,613	6,13
Mean	***27,42***	***0,935***	***-71,16***	***-47,26***	***122,01***	***0,497***	***3,53***
SD	***7,44***	***0,023***	***4,16***	***2,82***	***30,00***	***0,136***	***1,27***

7.7.2. Multiform

Cell #	Tau	Sag	RMP	AP thresh	Input R	ISI ratio	Rebound
141113_1	33,80	0,930	-70,84	-43,95	121,05	0,718	3,37
141113_2(2)	45,03	0,937	-73,68	-48,07	199,95	0,461	3,91
141127_2(4)	28,25	0,915	-70,52	-45,63	136,95	0,484	4,37
141203_1(1)	26,95	0,964	-64,97	-37,97	176,27	0,359	3,28
141203_1(4)	5,40	0,897	-63,12	-42,48	54,18	0,160	8,58
141203_2(3)	27,95	0,914	-73,89	-50,27	184,30	0,525	5,17
141203_4(2)	36,18	0,921	-70,43	-46,34	119,41	0,485	3,53
141204_2(2)	18,20	0,939	-75,78	-48,25	116,52	0,352	2,72
141204_3(2)	13,20	0,925	-67,36	-44,32	198,88	0,592	3,95
141211_2(1)	19,10	0,929	-74,58	-49,72	110,47	0,381	3,55
141211_2(2)	16,73	0,976	-76,15	-50,54	116,28	0,284	1,22
141211_3(2)	19,13	0,962	-71,19	-49,82	134,25	0,307	2,85
141211_4(1)	27,08	0,946	-69,64	-49,03	108,98	0,614	2,50
150220_1(1)	25,25	0,968	-72,11	-50,49	81,16	0,640	1,25
150220_1(2)	25,55	0,961	-71,93	-49,57	81,28	0,655	2,33
150220_1(3)	23,03	0,959	-68,85	-49,46	71,02	0,459	3,61
141002_2(1)	24,60	0,956	-74,42	-44,68	90,19	0,592	3,19
141002_3(3)	26,14	0,927	-65,26	-42,89	137,99	0,626	4,10
Mean	***24,53***	***0,940***	***-70,82***	***-46,86***	***124,40***	***0,483***	***3,53***
SD	***8,88***	***0,022***	***3,78***	***3,54***	***42,88***	***0,152***	***1,61***

7.7.3. Oblique Pyramidal

Cell #	Tau	Sag	RMP	AP thresh	Input R	ISI ratio	Rebound
141112_1(1)	9,58	0,907	-65,64	-51,12	60,18	0,190	6,60
141112_1(4)	31,05	0,931	-64,38	-51,33	97,43	0,233	3,14
141112_2(2)	30,65	0,939	-69,85	-48,30	158,00	0,501	3,72
141112_2(3)	35,73	0,931	-66,79	-36,12	163,02	0,450	3,60
141112_4(1)	22,18	0,959	-77,92	-49,41	116,65	0,838	1,69
141113_3(1)	19,25	0,932	-63,72	-40,36	72,33	0,545	5,50
141127_1(1)	25,68	0,912	-66,76	-48,82	124,13	0,290	6,40
141127_2(2)	40,43	0,917	-68,16	-45,78	137,15	0,420	4,27
141127_3(2)	35,50	0,936	-68,20	-47,17	196,89	0,528	5,20
141203_2(4)	23,18	0,949	-73,13	-45,21	154,59	0,480	2,39
141211_1(1)	23,00	0,957	-74,89	-51,13	155,69	0,386	3,46
141204_1(1)	43,15	0,912	-70,38	-42,56	159,33	0,620	5,74
150220_3(2)	28,23	0,939	-66,23	-52,86	120,22	0,401	3,06
141002_3(1)	31,98	0,940	-69,81	-43,57	143,21	0,581	4,91
Mean	***28,54***	***0,933***	***-68,99***	***-46,69***	***132,77***	***0,462***	***4,26***
SD	***8,91***	***0,016***	***4,06***	***4,77***	***37,38***	***0,167***	***1,50***

7.7.4. Pyramidal

Cell #	Tau	Sag	RMP	AP thresh	Input R	ISI ratio	Rebound
141113_3(2)	23,38	0,936	-66,21	-46,15	104,77	0,549	4,75
141203_1(2)	15,83	0,899	-63,22	-48,89	66,54	0,368	12,38
141203_2(2)	14,13	0,897	-69,89	-49,28	70,40	0,464	7,48
141203_3(1)	40,98	0,893	-60,63	-42,00	155,96	0,591	2,87
141204_2(1)	40,88	0,935	-74,78	-48,64	134,58	0,435	4,73
141204_3(1)	12,03	0,993	-76,42	-37,43	76,77	0,721	0,72
150108_2(1)	26,48	0,951	-76,44	-46,56	109,06	0,466	2,17
150108_3(2)	31,18	0,934	-73,37	-48,64	112,04	0,352	3,13
150108_4(2)	26,40	0,969	-78,31	-49,14	101,35	0,230	2,06
150220_2(1)	28,40	0,960	-69,82	-47,64	89,55	0,681	1,46
Mean	***25,97***	***0,937***	***-70,91***	***-46,44***	***102,10***	***0,486***	***4,18***
SD	***10,14***	***0,033***	***6,02***	***3,85***	***28,24***	***0,152***	***3,49***